Departement Fysica
Faculteit Wetenschappen
Universiteit Antwerpen

Proefschrift ter verkrijging van de graad van
Master in de Fysica

Hybrid statistics-simulations based method for atom-counting using scanning transmission electron microscopy

Annelies De wael

prof. dr. Sandra Van Aert
dr. Annick De Backer

Academiejaar 2015-2016

Dankwoord

Terugkijkend op de vijf jaren van mijn opleiding Fysica, die voorbij gevlogen zijn, wil ik heel erg graag mijn leerkracht wiskunde uit de laatste jaren van mijn middelbare opleiding aan het Koninklijk Atheneum van Lier, mevrouw Danielle Geukens, bedanken. Mevrouw, u hebt een belangrijke rol gespeeld in mijn keuze voor de richting Fysica door me zo goed voor te bereiden en de wiskunde zo leuk te maken. Bedankt ook zeker voor uw blijvende interesse in mijn studies.

Na het schrijven van een bachelorthesis onder de geweldige begeleiding van prof. dr. Sandra Van Aert en dr. Annick De Backer heb ik met veel overtuiging en enthousiasme gekozen om ook mijn masterthesis bij hen te schrijven. Daar heb ik tot op de dag van vandaag nog geen seconde spijt van gehad. Daarom verdienen zij hier zonder twijfel de grootste dankbetuigingen.
Sandra, ik wil je ontzettend bedanken voor je enthousiasme, dat heel erg motiverend en aanstekelijk werkt! Bedankt ook voor al de interessante en bemoedigende gesprekken over problemen en resultaten gerelateerd aan de masterthesis en meer. En ik wil je zeker ook bedanken voor de keuze voor dit uitdagende, leuke onderwerp en de vele kansen die je me hiermee gegeven hebt.
Annick, tijdens de voorbereidingen van mijn masterthesis heb ik je je doctoraat met glans zien afronden en heb je een prachtige tweede dochter op de wereld gezet. Ik wil je bedanken voor de vele moeite die je in de begeleiding van mijn onderzoek gestoken hebt, wat ik des te meer weet te appreciëren, gezien je je handen zelf ook meer dan vol gehad hebt de voorbije jaren. Jouw motivatie voor je onderzoek werkt ontzettend inspirerend.

Vervolgens wil ik mijn familie en Livio bedanken voor hun onvoorwaardelijke steun, motivatie en interesse. Livio, jou wil ik niet enkel bedanken voor je motiverende aanmoedigingen wanneer de moed me af en toe dan toch in de schoenen zonk, maar ook voor je kritische kijk op mijn onderzoek en de hulp bij het redeneren over de opbouw van mijn code. Bedankt om er altijd voor me te zijn. Dankjewel ook zeker aan mijn papa die heel veel moeite heeft gedaan om mijn onderzoek te begrijpen en me zo dwong na te denken over de beste manier om alles uit te leggen. En dankjewel mama voor je zoektocht naar grammaticale en spellingsfoutjes.

I also want to thank prof. dr. Peter Nellist and dr. Lewys Jones from the STEM group of the department of Materials at the University of Oxford for the interesting discussions about what they hope to achieve using this interesting new method and how the method might be improved and extended in the future. Finally, I want to thank prof. dr. Sandra Van Aert and prof. dr. Peter Nellist for giving me the opportunity to do an internship at the University of Oxford.

Samenvatting

In deze thesis wordt een nieuwe hybride methode ontwikkeld voor het tellen van het aantal atomen uit ringvormige donkerveld rooster transmissie elektronenmicroscopie (ADF STEM) beelden van monoatomaire kristallijne nanostructuren. ADF STEM beelden zijn zeer bruikbaar voor een kwantitatieve analyse, omdat de beeldintensiteit rechtstreeks bepaald wordt door het aantal atomen in het onderzochte materiaal en hun atoomtype. Er bestaan tegenwoordig twee methoden die toelaten het aantal atomen te tellen.
De eerste methode maakt gebruik van beeldsimulaties die het experimentele proefopzet zo goed mogelijk nabootsen en de intensiteiten uit deze gesimuleerde beelden rechtstreeks vergelijken met de experimentele intensiteiten. Deze methode laat echter niet toe de precisie van de telresultaten te bepalen. Bovendien hangt de betrouwbaarheid van de telresultaten af van eventuele meetfouten bij het bepalen van het experimentele proefopzet die onopgemerkt blijven.
De tweede methode voor het tellen van het aantal atomen maakt gebruik van zogenaamde statistische parameterschattingstheorie. Deze methode modelleert de waarschijnlijkheidsverdeling van de experimentele intensiteiten en schat de parameters die deze verdeling bepalen. Voor beelden met weinig ruis zijn de telresultaten die op deze manier bekomen worden zeer betrouwbaar. Bovendien voorziet deze methode in een maat voor het bepalen van hun precisie.
De hybride methode maakt gebruik van de intensiteiten uit gesimuleerde beelden voor het bepalen van de waarschijnlijkheidsverdeling van de experimentele intensiteiten. De gesimuleerde intensiteiten leveren namelijk een voorkennis over de verwachte waarden voor de experimentele intensiteiten overeenkomstig met een verschillend aantal atomen onder elkaar in een atoomkolom. Om rekening te houden met mogelijke kalibratiefouten in het gesimuleerde proefopzet worden niet de gesimuleerde intensiteiten zelf gebruikt om de verwachte waarden te bepalen, maar een functie ervan. Deze functie wordt bepaald door het effect van enkele veelvoorkomende meetfouten op de intensiteiten te bekijken. Hieruit volgt de keuze voor een lineair verband, dat opgenomen wordt in het model dat de waarschijnlijkheidsverdeling van de experimentele intensiteiten beschrijft, en de basis vormt van de hybride methode ontwikkeld in deze thesis. De implementatie en interpretatie van de hybride methode worden in detail bestudeerd, om vervolgens de prestaties van de methode te onderzoeken. Met de hybride methode worden hogere percentages correct getelde atoomkolommen bereikt dan met de bestaande methode die enkel gebruik maakt van statistische parameterschattingstheorie zonder de voorkennis uit beeldsimulaties. Vergelijkbaar met een onderbelichte foto waaruit details moeilijker te herkennen zijn, is het ook moeilijker om atomen te tellen uit "onderbelichte" ADF STEM beelden, aangezien die meer ruis bevatten. Op basis van de berekende percentages voorspellen we dat de grootste verbetering merkbaar zal zijn voor de analyse van kleine nanodeeltjes waarvan beelden met een zeer lage elektronendosis werden opgenomen. Tenslotte wordt de methode toegepast op experimentele beelden. Als eerste worden atomen geteld uit een goed geconditioneerd beeld van een goud nanorod, waarvoor atomen reeds met de bestaande statistische methode geteld konden worden. De telresultaten die hieruit bekomen worden met de hybride methode komen goed overeen met de eerder bekomen resultaten. We besluiten met de analyse van een uitdagend experimenteel beeld van een klein platinum-iridium nanodeeltje, opgenomen met een zeer lage elektronendosis, waaruit voor het eerst betrouwbare telresultaten bekomen worden.

Abstract

In this thesis, a novel hybrid statistics-simulations based method for atom-counting from annular dark field scanning transmission electron microscopy (ADF STEM) images of monatomic crystalline nanostructures is developed. ADF STEM images are very useful for a quantitative analysis, because the image intensities are directly determined by the number of atoms in the material under study and their atom type. Nowadays, two methods exist that allow us to count the number of atoms.
The first method uses image simulations that mimic the experimental set-up as accurate as possible and compares the intensities from the simulated images directly to the experimental intensities. However, this method does not provide a measure for the precision of the atom-counting results. Furthermore, any measurement errors in determining the experimental set-up, on which the accuracy of the counting results depends, remain undetected.
The second method for atom-counting uses so-called statistical parameter estimation theory. This method models the probability distribution of the experimental intensities and estimates the parameters that determine this distribution. For images with a high signal-to-noise ratio, the obtained counting results are very reliable. Furthermore, this method provides a measure for their precision.
The hybrid method uses the intensities of the simulated images to determine the probability distribution of the experimental intensities, since the simulated intensities provide a prior knowledge about the expectation values of the experimental intensities corresponding to different numbers of atoms stacked below one another in an atomic column. To account for possible calibration errors in the simulated experimental set-up, a function of the simulated intensities is used to determine the expectation value, rather than the simulated intensities themselves. This function is determined by studying the effect of common measurement errors on the intensities. This study results in the choice for a linear relationship, which is included in the model for the probability distribution of the experimental intensities, and forms the basis of the hybrid method developed in this thesis. The implementation and interpretation of the hybrid method are studied in detail, and used to study the performance of the hybrid method. Higher percentages of correctly counted atomic columns are reached using the hybrid method as compared to using the existing method based on statistical parameter estimation theory without the prior knowledge from image simulations. Comparable to a dimly lit photograph, from which features are harder to recognise, it is also very difficult to count atoms from "dimly lit" ADF STEM images, which have a low signal-to-noise ratio. The largest improvement is predicted for the analysis of small nanoparticles, imaged using a very low electron dose.
Finally, the method is applied to some experimental images. First, atoms are counted from a well-conditioned image of a gold nanorod, for which atom-counting was already possible using the existing statistics-only based method. The atom-counts obtained from this image using the hybrid method are in good agreement with the previously obtained results. We conclude with the analysis of a challenging experimental image of a very small platinum-iridium nanoparticle, imaged with a very low electron dose. For the first time, reliable atom-counts are obtained for this image.

Contents

Chapter 1

Introduction

Modern society depends strongly on materials science, a research area that comprises the interdisciplinary study of materials properties and ultimately aims to design new, advanced materials with pre-specified optical, dynamical, thermodynamic, electronic and/or chemical properties. Such advanced materials are used in technologically innovating applications, such as the use of lightweight composites for faster vehicles, optical fibres for telecommunications and silicon microchips in smartphones and computers that are becoming increasingly smaller and faster, keeping up with Moore's law [Moore, 1998]. Over the last decades, materials science has evolved from the macro- to the microscale and even further down to the nanoscale, thanks to the development of advanced imaging techniques for nanomaterials. Nanomaterials are materials with at least one dimension in the nanometer range. Interestingly, materials often exhibit strongly different properties at the nanoscale, as compared to their macroscopic properties. For example, gold in its macroscopic form is chemically inert, while gold nanoparticles can be used as a catalyst to enhance the efficiency of a chemical reaction [Mikami et al., 2013]. In the field of nanomedicine, gold nanoparticles can also be used to control the protein orientation [Lin et al., 2015]. Changing the length of gold nanorods, nanoparticles with an elongated shape, can be used to tune the wavelength of the absorbed light, enabling the use of such nanorods in medical applications, such as drug delivery [Stone et al., 2011]. Another group of nanoparticles with particularly interesting properties are the bimetallic nanoparticles, such as for example platinum-iridium nanoparticles. Such platinum-based bimetallic nanoparticles are very efficient catalysts, and can be used for carbon monoxide oxidation in fuel cells [Ralph and Hogarth, 2002].

Materials science ultimately aims to understand how the synthesis of a material influences its structure, and thus the material's properties and performance. This understanding is called the "materials paradigm" [Olson, 2000; Yang and Tarascon, 2012]. Knowledge of the interrelationships among a material's properties, performance, processing and structure allows us to evolve from experimental observation, theoretical understanding and description of existing materials towards theoretical predictions and the actual production of new materials.

The physical properties of nanostructures are mainly controlled by their composition, their chemical bonding and the positions of their atoms. At the nanoscale, the electronic structure of materials becomes size-dependent [Koli et al., 2014]. An example of the size-dependence of properties of nanoparticles is shown in figure 1.1. The optical properties of silver nanoparticles can be tuned by changing the size of the nanoparticles. Figure 1.1 shows how the colour of the colloids changes with increasing nanoparticle size [Huang and Nancy Xu, 2010]. The size dependence of nanomaterials opens up many possibilities for production of materials with unique properties. Due to the crucial dependence of a nanomaterial's properties on its size, we need to be able to determine the size with high precision and accuracy in order to allow for production of materials with predicted properties. This can be achieved through accurately counting the number of atoms on an atomic scale. In order to count atoms with atomic resolution, electron microscopy images of the particles are recorded. By counting

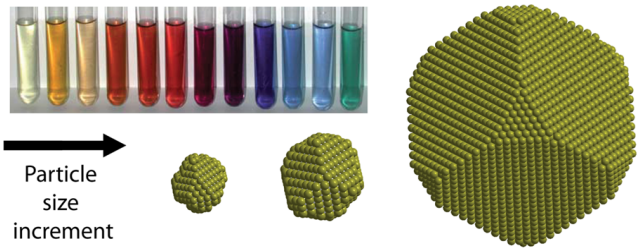

Figure 1.1: Size dependence of the optical properties of colloidal silver nanoparticles. The colour of the colloids changes with the nanoparticle size [Huang and Nancy Xu, 2010].

the number of atoms from two-dimensional (2D) images, recorded under different viewing directions, a three-dimensional (3D) reconstruction of the structure can be obtained, as shown in figure 1.2, where counting results of two different projections have been used as an input for discrete tomography to obtain a 3D reconstruction of a silver (Ag) nanoparticle embedded in an aluminium (Al) matrix [Van Aert et al., 2011]. From such 3D reconstructions of a particle, the exact shape and size can be determined. Using the exact atomic positions, the properties of the nanomaterial can be predicted and studied using ab-initio calculations[1]. Atom-counting results have already been combined with ab-initio calculations to study the dynamical behaviour of ultrasmall germanium clusters [Bals et al., 2012].

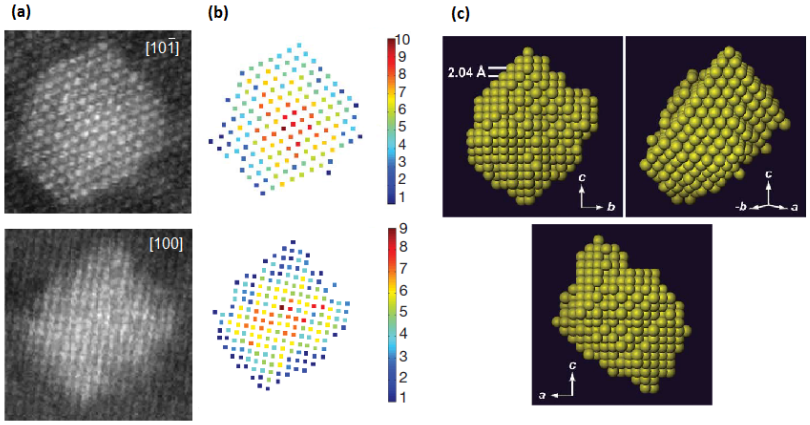

Figure 1.2: 3D atomic imaging of crystalline nanoparticles. (a) Experimental HAADF STEM images of nanosized Ag clusters embedded in an Al matrix in [10$\bar{1}$] zone-axis orientation and [100] zone-axis orientation. (b) Number of Ag atoms per column. (c) The computed 3D reconstruction of the Ag nanocluster viewed along three different directions. Figure adjusted from [Van Aert et al., 2011].

In order to be able to count atoms, images of the structure at the atomic scale need to be recorded that contain information about the thickness of the nanoparticle. Different experimental methods exist to image nanomaterials. Scanning tunnelling and atomic force microscopy provide information about the local surface structure [Wiesendanger, 1994]. X-ray and neutron diffraction techniques, on the other hand, do not only provide information about the surface but about the inside of the material as well, albeit averaged structure information [Zanchet et al., 2000]. Diffraction techniques are therefore very useful for the analysis of periodic materials, such as crystals, whereas they do not

[1]Theoretical calculations using the exact structure information as an input, in order to calculate electronic properties "from the beginning".

suffice for the analysis of nanomaterials which are usually aperiodic. An excellent technique to study nanostructures that provides non-averaged information about the entire material is atomic resolution (scanning) transmission electron microscopy (STEM) because of the strong interaction of electrons with small volumes of matter [Fujita and Sumida, 1994; Henderson, 1995; Spence, 1999]. In a scanning transmission electron microscope, schematically shown in figure 1.3, an electron beam is focused into a fine probe and scans across the sample in a 2D raster. For each probe position, the electrons scattered towards the detector are integrated to determine the image intensity. An image of the sample is formed, displaying the scattered intensities at the different probe positions. Intensities in annular dark field scanning transmission electron microscopy (ADF STEM) images increase with increasing number of atoms in an atomic column as well as with increasing atomic number of the atoms [Anderson et al., 1997]. Thanks to this property, counting atoms through quantitative analysis of the ADF STEM image intensities is possible.

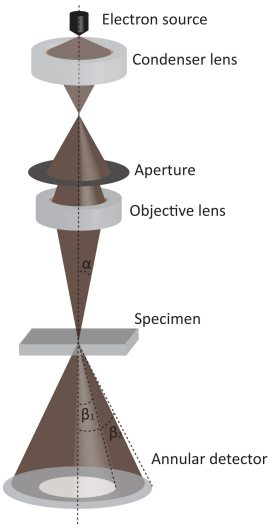

Figure 1.3: Ray diagram of a scanning transmission electron microscope, indicating how the most important lenses and apertures effect the electron beam before it is focussed onto the sample. Scattered electrons are detected on the annular detector, and integrated to calculate the ADF STEM image intensity.

At present, two methods for counting the number of atoms from scanning transmission electron microscopy images exist. The first method makes use of image simulations. ADF STEM images under the experimental conditions can be accurately simulated in order to count atoms through direct comparison between the simulated image intensities and the experimental image intensities [LeBeau et al., 2010]. Advanced image simulations software exists that can simulate the images formed in different imaging modes for samples under study [Loane et al., 1991; Bollig et al., 1996; Kirkland, 1998; Muller et al., 2001; Ishizuka, 2002; Koch, 2002; Croitoru et al., 2006; Rosenauer and Schowalter, 2007; Rosenauer et al., 2008]. Quantitative comparison of experimental images with simulations requires intensity measurements on an absolute scale [LeBeau et al., 2008]. This is achieved by normalising the experimental intensities with respect to the incident electron beam. Furthermore, a full characterisation of the ADF detector should be carried out in order to achieve true agreement between simulations and experiment [Grillo, 2011; Findlay and LeBeau, 2013; MacArthur et al., 2014]. This simulations-only based method is very intuitive, but an important drawback of this method is that there is no way to determine the accuracy and precision of the atom-counts. Any systematic errors in the image simulations stay undetected, since a match between experimental intensities and simulated intensities can always be found, even with inaccurate simulations.
The alternative atom-counting method developed recently does provide a measure for the precision of

the atom-counts. This method is based on statistical parameter estimation theory, which has become a trusted framework for quantitative analysis of ADF STEM images over the last few years. Unknown structure parameters are estimated by fitting a physical imaging model to the experimental images using a criterion of goodness of fit [den Dekker et al., 2005; Van Aert et al., 2005]. This approach allows one to measure two-dimensional (2D) atomic column positions with subpicometer precision [Van Aert et al., 2012], to measure compositional changes at interfaces [Van Aert et al., 2009; Boschker et al., 2011; Huijben et al., 2013], to count atoms with single atom sensitivity [Van Aert et al., 2013; De Backer et al., 2013, 2015a], and to reconstruct three-dimensional (3D) atomic structures [Van Aert et al., 2011; Bals et al., 2012]. This statistics-only based method is very reliable and results in atom-counts with single atom sensitivity [Van Aert et al., 2013], provided the images are well-conditioned and its conditions do not exceed the limitations of the method [De Backer et al., 2013, 2015a].
Despite the advantages of the STEM imaging mode, the high beam currents used in STEM imaging make the technique less suitable for the study of beam-sensitive nanostructures. In order to minimise radiation damage, the electron dose, i.e. the number of incident electrons used to record an electron microscopy image per unit of area in the material, should be reduced. Comparable to the use of a dimmed light source in light microscopy, imaging using a low electron dose in electron microscopy will result in more noisy images. The performance of the statistics-only based atom-counting method is very sensitive to a low signal-to-noise ratio. Therefore, in order to be able to count the number of atoms from low dose images of beam-sensitive particles, a new method that suffers less critically from a low signal-to-noise ratio is required.

The goal of this master's thesis is to develop a hybrid statistics-simulations based atom-counting method, in order to count the number of atoms in challenging ADF STEM images of small nanostructures with low signal-to-noise ratios from which atoms cannot be counted to date. This hybrid method will be realised by incorporating prior knowledge about the material, obtained through image simulations, into the well-established statistical parameter estimation theory framework. The outline of this thesis is as follows. In chapter 2, quantitative electron microscopy and the existing approaches for atom-counting in experimental annular dark field scanning transmission electron microscopy (ADF STEM) images are discussed in more detail. Following this discussion, we introduce a hybrid statistics-simulations based method which directly combines elements from both existing methods in chapter 3. The way of including this prior knowledge from image simulations in the statistical parameter estimation theory framework will be discussed, as well as the interpretation and implementation of the new algorithm. The performance of this novel hybrid atom-counting method is examined in chapter 4, where it is also compared to the previous statistics-only based atom-counting method. Furthermore, in this chapter, we examine the accuracy and precision of the atom-counting results. Finally, the hybrid method is applied to experimental images of a large gold (Au) nanorod and very small platinum-iridium (Pt/Ir) nanoparticles. The Au nanorod, analysed in chapter 5, is very well-conditioned for atom-counting and has previously been analysed using the statistics-only based atom-counting method by Van Aert et al. [2013]. The counting results obtained using this method are reliable, and therefore this case study serves as a verification of the methodology. An analysis of the Pt/Ir nanoparticles, discussed in chapter 6, was also previously attempted using the statistics-only based method by De Backer et al. [2015a]. However, high electron dose images were needed to obtain a reliable analysis. In this chapter, the analysis of a low electron dose image using the hybrid statistics-simulations based atom-counting method will be shown. Up until now, atoms could not be counted from this image. This case study will therefore be used to show the great improvement of the hybrid method for quantitative analysis of challenging nanomaterials.

Chapter 2

Atom-counting using ADF STEM images

Nowadays, two different approaches for counting the number of atoms using annular dark field scanning transmission electron microscopy (ADF STEM) images exist. The first approach is a simulations-only based approach which is very intuitive and uses image simulations, whereas the second approach is a statistics-only based approach which regards the images as data planes from which unknown structure parameters need to be estimated. Both approaches use images obtained with a scanning transmission electron microscope (STEM). We will therefore start this chapter with a discussion of quantitative STEM. Next, both existing atom-counting approaches will be discussed in more detail.

2.1 Quantitative scanning transmission electron microscopy

Quantitative electron microscopy refers to the image processing of electron microscopy images in order to extract quantitative information about the sample's structure and composition, whereas in qualitative electron microscopy the images are interpreted visually, without extracting any numerical data. In order to predict properties of materials using ab initio calculations, positions of the atoms need to be known with a high precision [Koli et al., 2014]. Therefore, an essential step towards materials design is the quantitative, instead of qualitative, interpretation of high resolution electron microscopy images of nanomaterials.

An excellent technique for the imaging of nanostructures is atomic resolution (scanning) transmission electron microscopy (STEM) because of the strong interaction of electrons with small volumes of matter [Fujita and Sumida, 1994; Henderson, 1995; Spence, 1999]. This imaging technique has become a popular technique, because it has some advantages over conventional parallel beam TEM. Examples are the high chemical sensitivity and relative ease of the image interpretability [Nellist and Pennycook, 2000]. Remarkable high-technology developments in the lens design have greatly improved the image resolution [Haider et al., 1998]. Nowadays, state-of-the-art instruments are available with a resolution of the order of 50 pm [Erni et al., 2009; Takayanagi et al., 2011]. For most atom types, this exceeds the point where the electrostatic potential of the atoms is the limiting factor [Van Dyck et al., 2003]. In addition, detectors behave more and more like ideal quantum detectors [Ruskin et al., 2013], making the microscope itself less restricting. Therefore, the quality of experimental images is mainly set by the unavoidable presence of electron counting noise and environmental disturbances [Jones and Nellist, 2013; Jones et al., 2015].

High-angle annular dark field (HAADF) STEM is especially suited for quantitative analysis, owing to the excellent dependence of the image intensities on the atomic number Z of the atoms in the sample and the number of atoms in the sample [Anderson et al., 1997; Nellist and Pennycook, 2000]. In HAADF STEM, only electrons that have scattered incoherently over angles much larger than the

probe convergence angle (α in figure 1.3) are detected [Nellist and Pennycook, 2000; Hawkes et al., 2007]. Depending on the collection range of the detector, the dependence of the image contrast on the atomic number Z will be different, as well as the pixel signal-to-noise ratio. Different STEM detector geometries are nowadays available [Cowley et al., 1995; Shibata et al., 2010; Yang et al., 2015]. In annular dark field (ADF) STEM, the detector inner angle (β_1 in figure 1.3) exceeds the probe convergence angle (α in figure 1.3). Depending on the detector inner angle, imaging modes are called low angle (LA), medium angle (MA) or high angle (HA) ADF STEM. Traditionally, high angle annular dark field (HAADF) STEM is used to extract quantitative information, but it has been shown that the HAADF STEM regime is not necessarily optimal for atom-counting [De Backer et al., 2015b]. The optimal detector inner angle increases for increasing thickness when deriving the optimal STEM detector design for atom-counting. For thin samples, the LAADF STEM regime exhibits optimal atom-counting properties, even though visual interpretation in this imaging mode is less straightforward. Optimal imaging modes can be derived, in order to extract more quantitative information using the same electron dose [De Backer et al., 2015b].
ADF STEM images contain useful information for quantitative analysis, and are therefore used as starting point for both existing atom-counting approaches discussed in the remainder of this chapter. In the next section we will discuss how simulations of ADF STEM images can be used to count the number of atoms based on an experimental ADF STEM image of a nanomaterial.

2.2 Simulations-only based atom-counting method

By simulating the image formation of a scanning transmission electron microscope, the resulting images for a certain nanomaterial under specific experimental conditions can be simulated. The intensities from such simulated images can then be used to count atoms by direct comparison to the experimental image intensities.
Advanced image simulations packages exist that can accurately simulate the images formed in different imaging modes for samples under study, based on multislice or Bloch wave algorithms [Cowley and Moodie, 1959; Bollig et al., 1996; Kirkland, 1998; Ishizuka, 2002; Allen et al., 2003; Findlay et al., 2003; Croitoru et al., 2006], or on frozen phonon or frozen lattice calculations [Loane et al., 1991; Muller et al., 2001; Koch, 2002; Rosenauer and Schowalter, 2007; Rosenauer et al., 2008]. Image simulations can accurately describe experimental image contrast up to at least 100 nm thickness [LeBeau et al., 2008, 2010]. Image simulations are performed using experimental parameters such as the accelerating-voltage, convergence angle, spherical aberration constant, defocus value and detector angles as an input. The experimental set-up is matched accurately in order for the simulations to agree with the experiment [Findlay and LeBeau, 2013; Martinez et al., 2015; Jones, 2016].
Quantitative agreement between experiment and simulations is achieved by placing intensity variations in the experimental image on an absolute scale by normalising the measured image intensities with respect to the incident beam [Rosenauer and Schowalter, 2007; LeBeau et al., 2008]. Furthermore, to achieve true quantitative agreement between simulated intensities and experimental intensities, a full characterisation of the ADF detector should be performed [Grillo, 2011]. The detector response is mapped by scanning the STEM probe over the ADF detector [Findlay and LeBeau, 2013; MacArthur et al., 2014]. This detector map has an important influence on the agreement between simulation and experiment, since ADF detectors of different manufacturers were found to respond both inhomogeneously and asymmetrically. In order to correct for the detector map, a detector sensitivity profile can be included in the image simulations [Grieb et al., 2012; Mehrtens et al., 2013; Martinez et al., 2015].
Image intensities corresponding to the atomic columns determined from the experimental image can now be compared to those determined from the simulated image in order to count the number of atoms per column. However, due to channelling of the electrons when propagating through the material, the intensity of a column with two atoms does not simply equal two times the intensity of a column

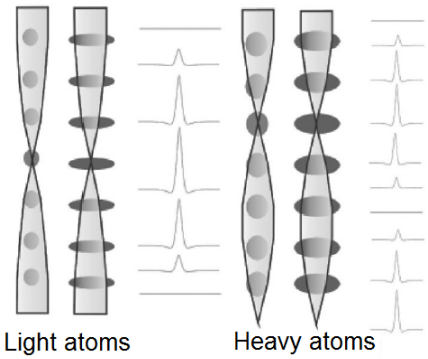

Figure 2.1: Schematic representation of the effect of channelling [Geuens and Van Dyck, 2005]. Each atom can be considered as a lens. The incoming electron wave is focussed at periodic distances, resulting in a non-linear increase of the intensities in an ADF STEM image with the number of atoms in a column.

with only one atom. Channelling causes a non-linear increase of the intensities with increasing thickness. Image simulations are therefore performed for a range of thicknesses to construct the so-called "library". For a monatomic nanostructure, the different thicknesses are directly related to different numbers of atoms in an atomic column. Channelling theory describes the quantum mechanical interaction of the incident electrons with the object. Intuitively, this effect can be understood as a lensing effect of the electron beam incident on an atomic column orientated along a crystallographic zone axis, as shown in figure 2.1. It causes the intensity of the scattered electrons from this atomic column to differ from the simple sum of scattered intensities caused by each individual atom. A detailed description is given by Geuens and Van Dyck [2005].

Different measures exist for the quantification of the total intensity of the scattered electrons for the individual atomic columns, such as average intensities within squares [LeBeau et al., 2010], peak intensities [LeBeau et al., 2010; E et al., 2013] and scattering cross sections calculated using circles [E et al., 2013] or Voronoi cells [Rosenauer et al., 2011; Jones et al., 2014; Nguyen et al., 2014]. Using statistical parameter estimation based on an empirical model of an ADF STEM image, an alternative definition to calculate the cross section exists [Van Aert et al., 2011], which will be discussed later on in section 2.3. Cross sections have been shown to have the best performance for atom-counting, because they are robust to changes in the probe such as a change in defocus, convergence angle or source size, and even to very small amounts of sample tilt [E et al., 2013; Jones and Nellist, 2013; Martinez et al., 2013; De Backer et al., 2015b; MacArthur et al., 2015].
A direct comparison between the experimental and the simulated image intensities corresponding to the atomic columns can be performed by determining the intensities with the same quantitative measure. Next, these experimental intensities are compared directly to the so-called "library values", i.e. the simulated intensities corresponding to atomic columns with different thicknesses. Using linear interpolation, the number of atoms in each column is determined. Since the number of atoms in a column is discrete, these numbers are then rounded to the nearest integer value [LeBeau et al., 2010]. An example of a counting result obtained using this method is shown in figure 2.2. In this example, atom-counts were obtained for a wedge-shaped gold film, imaged along the [110]-direction. Atom-counts are indicated in the experimental image, and columns are represented into a histogram according to the atom-counts. In this example, a nice agreement is found between experimental columns assigned to a certain number of atoms and the corresponding simulated columns. Visual discrimination between one atom differences is difficult, whereas columns with two atoms difference are already clearly distinct. However, using this simulations-only based method, a match with the experiment can always be forced, without knowing the accuracy and precision of the counting result.

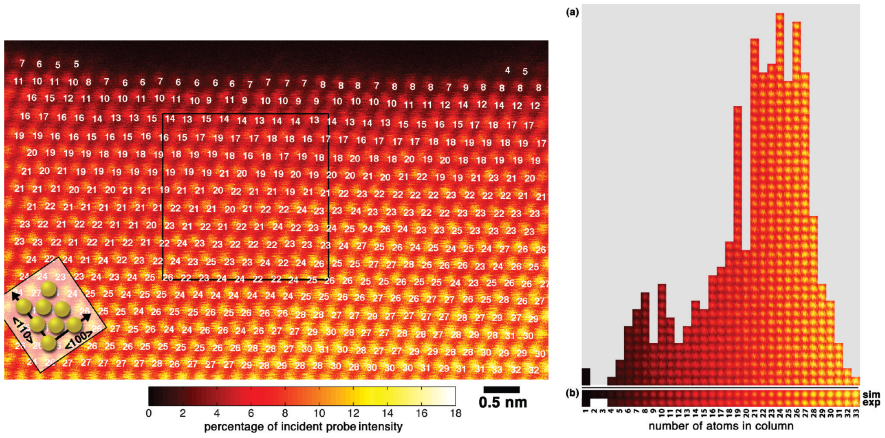

Figure 2.2: Example of atom-counting in ADF STEM images using the **simulations-only based method** [LeBeau et al., 2010]. Left: HAADF-STEM image of a wedge-shaped gold film viewed along [110]. The intensity maxima correspond to gold atom columns and the white labels near the lower right of each atom column indicate the number of atoms contained in that column. The image intensities are shown on an absolute scale relative to the incident beam intensity (see scale bar). Right: (a) Histogram of all the columns in the figure on the left, binned by the number of atoms they contain. (b) Atomic column images extracted from simulations (top row underneath the histogram) and experiments (bottom row underneath the histogram) after averaging all the experimental columns in each bin shown in (a).

This first approach for atom-counting is very intuitive. However, small mismatches between the actual and the simulated experimental set-up, such as a different detector inner angle or sample tilt, can influence the simulated image intensities significantly. These systematic errors remain undetected and the reliability of the quantitative analysis therefore depends solely on the accuracy of the simulations to match the experiment [Van Aert et al., 2013; Jones, 2016]. Alternatively, atoms can be counted using a statistical parameter estimation theory framework. In this statistics-only based method, simulations are no longer needed, and such undetected systematic errors can be avoided, as will be discussed in the next section.

2.3 Statistics-only based atom-counting method

Statistical parameter estimation theory has become a recognised framework for the quantitative analysis of electron microscopy images [den Dekker et al., 2005; Van Aert et al., 2005], and since several years, statistical parameter estimation theory is used for atom-counting in ADF STEM images [Van Aert et al., 2011; De Backer et al., 2013; Van Aert et al., 2013]. Unknown structure parameters are determined from the observations, by formulating a physical model for the expectation value of the observations and estimating the unknown parameters of the model using statistical parameter estimation theory. Contrary to the previous simulations-only based approach for atom-counting, this approach does allow for a quantification of the precision of the atom-counts. In this section, the methodology of this method will be explained, and a practical example will be shown. First of all, a model which describes the image contrast of ADF STEM images is formulated.

Model-based parameter estimation

A parametric incoherent imaging model to describe the expectation values of the image intensities is formulated by a function that is sharply peaked at the positions of the atomic columns, modelled as a superposition of Gaussian peaks. The expectation value of the image intensity at pixel (k, l) in the

image is given by the following object function:

$$O(\mathbf{r}_{k,l};\theta) = \zeta + \sum_{n=1}^{N} \eta_n \exp\left(-\frac{(x_k - \beta_{x_n})^2 + (y_l - \beta_{y_n})^2}{2\rho^2}\right). \tag{2.1}$$

In this expression, ζ is a constant background present in the image, ρ is the width of the two-dimensional Gaussian peaks, η_n is the height of the n^{th} Gaussian peak, β_{x_n} and β_{y_n} are the x- and y-coordinate of the n^{th} atomic column, and N is the total number of atomic columns in the image. The unknown parameters are summarised in the parameter vector:

$$\theta = (\beta_{x_1}, ..., \beta_{x_N}, \beta_{y_1}, ..., \beta_{y_N}, \rho, \eta_1, ..., \eta_N, \zeta)^T. \tag{2.2}$$

Figure 2.3b shows such a model calculated based on the experimental HAADF STEM image of a lead (Pb) nanoparticle, embedded in crystalline silicon (Si), shown in figure 2.3a. The intensities belonging to the different atomic columns can be quantified in two ways. Either the maximum value of the Gaussian peak is used, or the volume under the peak, which equals the total intensity of the scattered electrons. The volume under an estimated Gaussian peak expresses the so-called scattering cross section:

$$\hat{V}_n = 2\pi\hat{\eta}_n\hat{\rho}^2, \tag{2.3}$$

with $\hat{\eta}_n$ and $\hat{\rho}$ the least squares estimates of the parameters η_n and ρ from equation (2.1). The scattering cross sections have been shown to outperform the peak intensities for atom-counting [De Backer et al., 2015a]. Therefore, in the remainder of the description of this statistics-only based method the scattering cross sections will be used as the measure to quantify the column intensities.

Probability distribution of the scattering cross sections

Due to the unavoidable presence of noise in the experimental image, the scattering cross sections are inherently random in nature. Therefore, when represented in a histogram, we do not see isolated peaks corresponding to the different thicknesses, but overlapping broadened components, as can be seen in the example in figure 2.3c. A distribution on the values of the cross sections corresponding to a number of atoms in a column around the expectation value will be present, causing the components to have a finite width σ around its location μ. This distribution will be modelled as a Gaussian distribution. The probability distribution of the scattering cross sections is therefore described by a so-called "Gaussian mixture model", a superposition of Gaussian components[1]:

$$f_{\text{mix}}\left(\hat{V}_n; \mathbf{\Psi}_G\right) = \sum_{g=1}^{G} \pi_g \phi_g\left(\hat{V}_n; \mu_g, \sigma\right), \tag{2.4}$$

with

$$\phi_g\left(\hat{V}_n; \mu_g, \sigma\right) = \frac{1}{\sqrt{2\pi\sigma^2}} \exp\left(-\frac{(\hat{V}_n - \mu_g)^2}{2\sigma^2}\right), \tag{2.5}$$

the Gaussian components. The mixing proportion π_g of the g^{th} component indicates which fraction of the columns in the image have a specific number of atoms corresponding to the g^{th} component, i.e. the weight of the g^{th} component in the Gaussian mixture model. Furthermore, in this expression μ_g represents the location of the g^{th} component in the mixture model and σ the width of the components, while $\hat{V}_n$ represents the least squares estimate for the n^{th} scattering cross section, expressed by equation

[1] Note that these 1D Gaussian components are different from the 2D Gaussian peaks previously used in the description of the model for the image intensities.

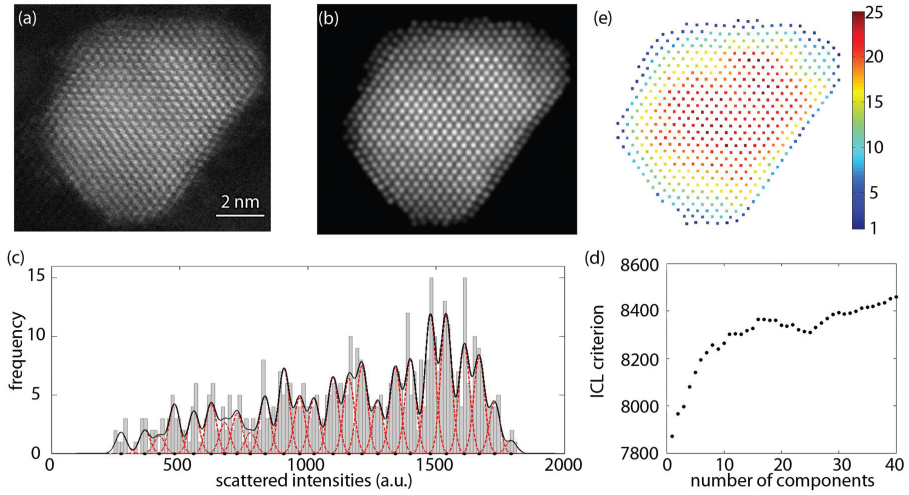

Figure 2.3: Example of atom-counting in ADF STEM images using the **statistics-only based method** [Van Aert et al., 2013]. (a) Experimental HAADF STEM image of a Pb nanoparticle embedded in crystalline Si. (b) Refined model. (c) Histogram of scattering cross sections of the Pb columns. The black solid curve shows the estimated mixture model; the individual components are shown as red dashed curves. (d) The Integrated Classification Likelihood criterion evaluated as a function of the number of Gaussian components in a mixture model. (e) Number of Pb atoms per column.

(2.3). The vector $\mathbf{\Psi}_G$ is the parameter vector containing all unknown parameters to be estimated in a Gaussian mixture model with G components:

$$\mathbf{\Psi}_G = (\pi_1, ..., \pi_{G-1}, \mu_1, ..., \mu_G, \sigma)^T. \tag{2.6}$$

Notice that π_G is not estimated, since the sum of all G mixing proportions must equal one, and therefore $\pi_G = 1 - \sum_{g=1}^{G-1} \pi_g$. This means that $2G$ parameters need to be estimated to determine the mixture model completely, and therefore be able to count atoms. It is common practice to assume homoscedastic components, i.e. a constant width σ for all components.

The goodness of fit of a Gaussian mixture model to the collection of scattering cross sections obtained from the experimental ADF STEM image, is expressed by the likelihood function $L(\mathbf{\Psi}_G)$:

$$L(\mathbf{\Psi}_G) = \prod_{n=1}^{N} f_{\text{mix}}\left(\hat{V}_n; \mathbf{\Psi}_G\right), \tag{2.7}$$

where experimental scattering cross sections were regarded as independent statistical draws from the Gaussian mixture model. The assumption of independent statistical draws from the underlying Gaussian mixture model implies that the so-called cross talk between neighbouring columns is assumed insignificant [Fertig and Rose, 1981; Nellist and Pennycook, 1999; Allen et al., 2003; De Backer et al., 2013].
Estimates of the parameters $\mathbf{\Psi}_G$ are computed by maximising the likelihood function. The parameter updates are iteratively calculated using the expectation maximisation (EM) algorithm, in two steps, the E-step and the M-step [Dempster et al., 1977]. In the E-step, the posterior probability that the estimated scattering cross section of the n^{th} column $\hat{V}_n$ belongs to the g^{th} component is calculated:

$$\tau_g\left(\hat{V}_n; \mathbf{\Psi}_G^{(k)}\right) = \frac{\pi_g^{(k)} \phi_g(\hat{V}_n; \mu_g^{(k)}, \sigma^{(k)})}{\sum_{h=1}^{G} \pi_h^{(k)} \phi_h(\hat{V}_n; \mu_h^{(k)}, \sigma^{(k)})}, \tag{2.8}$$

where G represents the total number of components in the Gaussian mixture model, ϕ_g the Gaussian components expressed by equation (2.5), and k the iteration step. The updates of the parameters that maximise the log likelihood are calculated in the M-step using the following expressions:

$$\pi_g^{(k+1)} = \frac{1}{N}\sum_{n=1}^{N}\tau_g\left(\hat{V}_n;\boldsymbol{\Psi}_G^{(k)}\right), \tag{2.9}$$

$$\mu_g^{(k+1)} = \frac{\sum_{n=1}^{N}\tau_g\left(\hat{V}_n;\boldsymbol{\Psi}_G^{(k)}\right)\hat{V}_n}{\sum_{n=1}^{N}\tau_g\left(\hat{V}_n;\boldsymbol{\Psi}_G^{(k)}\right)}, \tag{2.10}$$

and

$$\sigma^{(k+1)} = \sqrt{\frac{1}{N}\sum_{g=1}^{G}\sum_{n=1}^{N}\tau_g\left(\hat{V}_n;\boldsymbol{\Psi}_G^{(k)}\right)\left(\hat{V}_n-\mu_g\right)^2}. \tag{2.11}$$

The iterative EM-algorithm stops when convergence of the likelihood is reached. A more detailed description of this algorithm can be found in appendix A.
By means of simulations, the following input values for the algorithm were found to result in unbiased estimates for the parameters of the mixture model:

$$\pi_g^{(0)} = \frac{1}{G}, \tag{2.12}$$

for the mixing proportions, and

$$\sigma^{(0)} = \frac{\max(\hat{\mathbf{V}})-\min(\hat{\mathbf{V}})}{2G}, \tag{2.13}$$

for the width of the components. Different sets of starting values are used for the locations, ranging between the minimum and maximum value of the dataset [De Backer et al., 2013]. For each different set of starting values, the algorithm is iterated until convergence is reached. The estimates $\boldsymbol{\Psi}_G$ of the parameters in the mixture model are then given by the set of estimated parameters corresponding to the maximal likelihood value.
So far, we have only considered the estimation of the probability distribution of the scattered intensities presuming a specific number of components G. The next part deals with determining the number of components in a mixture model using order selection criteria.

Assessing the number of components in the mixture model using an order selection criterion

In order to estimate the unknown parameters of the Gaussian mixture model, the number of components has to be known. Unfortunately, determining the number of components is not very straightforward, which is a disadvantage of this statistics-only based atom-counting method. The number of components in the Gaussian mixture model, i.e. the model order, is determined through the use of an order selection criterion which takes into account the likelihood of the model on the one hand, and penalises the complexity of the model on the other hand. In this manner, a model with the right balance between complexity and likelihood can be chosen corresponding to a minimum in the order selection criterion evaluated as a function of the number of components. Many different information criteria exist [McLachlan and Peel, 2000], but the Integrated Classification Likelihood (ICL) criterion [Biernacki et al., 2000] has been proven to have the best performance for atom-counting [De Backer et al., 2013]. The ICL criterion is expressed as follows:

$$ICL(G) = -2\log L(\hat{\boldsymbol{\Psi}}_G) + 2EN(\hat{\tau}) + d\log N, \tag{2.14}$$

with $-2\log L(\hat{\mathbf{\Psi}}_G)$ the likelihood term depending on the estimated parameters $\hat{\mathbf{\Psi}}_G$ and $2EN(\hat{\tau}) + d\log N$ the penalty term depending on the number of parameters d, the sample size N and an entropy term:

$$EN(\hat{\tau}) = -\sum_{g=1}^{G}\sum_{n=1}^{N}\tau_g\left(\hat{V}_n;\hat{\mathbf{\Psi}}_G\right)\log\tau_g\left(\hat{V}_n;\hat{\mathbf{\Psi}}_G\right), \tag{2.15}$$

which favours mixture models with well-separated components, in order to estimate physically meaningful mixture models.

An example of this procedure to count the number of atoms using statistical parameter estimation theory is shown in figure 2.3. Atoms were counted in a Pb nanoparticle, embedded in crystalline Si. The experimental HAADF STEM image is summarised in the example shown in figure 2.3a. Figure 2.3b shows the estimated model, expressed by equation (2.1). From this estimated model, the scattering cross sections are calculated as the volumes under the estimated Gaussian peaks (equation (2.3)) and shown in the histogram in figure 2.3c. Next, the ICL criterion is calculated for the most likely Gaussian mixture model out of the different sets of starting values at each different number of components, and evaluated as a function of the number of components. The estimated mixture model corresponding to the minimum of interest in the ICL criterion is shown overlapping the histogram of scattering cross sections in figure 2.3c. For each column, the probability that its scattering cross section belongs to each component is determined. Next the columns are assigned atom-counts corresponding to the component with the highest probability. The atom-counts for this example are shown in figure 2.3e.

Using the statistical parameter estimation theory framework, atoms can be counted with single atom sensitivity [Van Aert et al., 2013; De Backer et al., 2013]. However, when the overlap between the components of the Gaussian mixture model is large or the average number of atomic columns per component is small, the atom-counting performance is strongly reduced [De Backer et al., 2013]. In practice, these challenging conditions correspond to noisy images of small nanoparticles.

2.4 Discussion

In this chapter, we have discussed the two existing atom-counting approaches. Ideally, both approaches should result in the same atom-counts. The direct comparison with image simulations is very intuitive and straightforward. However, a match with the experimental results can always be forced. Systematic errors in the measurement of the experimental set-up used as an input for the image simulations cannot be recognised, and determine the (unknown) accuracy of the atom-counts.
The atom-counting procedure based on statistical parameter estimation theory is simulations-free, and therefore does not suffer from undetectable systematic errors in the simulations' input. Furthermore, through the use of statistical parameter estimation theory, the precision on the atom-counting results can be quantified, using the estimated relative width of the components of the Gaussian mixture model. This was not possible using simulations only, and makes this atom-counting method more reliable. Atom-counts with single atom sensitivity can be obtained in this manner, provided the image of the nanoparticle is well-conditioned, which in this context means a high signal-to-noise ratio and/or a large number of atomic columns in the ADF STEM image.
The statistics-only based atom-counting approach fails under conditions which correspond to low dose images of small nanoparticles. Since beam-sensitive materials need to be imaged using a low electron dose, a method that enables atom-counting from images with a lower signal-to-noise ratio is required. By incorporating prior knowledge from image simulations into a statistical parameter estimation theory framework, we aim to overcome these limitations. This will be realised in a novel hybrid method, introduced in the next chapter.

Chapter 3

Hybrid method: methodology

Two different approaches for atom-counting have been introduced in the previous chapter, based respectively on image simulations [LeBeau et al., 2010; Jones et al., 2014] or on statistical parameter estimation theory [Van Aert et al., 2011, 2013; De Backer et al., 2013]. Counting the number of atoms through direct comparison with image simulations is a very straightforward approach. An important disadvantage of this approach however is that systematic errors, caused by small mismatches between the actual and simulated experimental set-up, are very difficult to detect, but can nonetheless influence the simulated image intensities significantly. Therefore, the reliability of this image simulations-only based atom-counting approach depends solely on the unknown accuracy of the simulations [Van Aert et al., 2013; Jones, 2016]. At present, the most reliable atom-counts from ADF STEM images of nanoparticles are obtained through analysis using statistical parameter estimation theory, independent from image simulations. However, caution is needed when analysing small nanoparticles. Such particles are very beam-sensitive and therefore need to be imaged using a low electron dose, which leads to a poor signal-to-noise ratio in the images and may result in inaccurate atom-counts. By independently performing image simulations, the counting results obtained using the statistics-only based method can be verified. If no agreement is found between results from the independent statistical analysis and the image simulation, we conclude that atom-counts are inaccurate. This was for example the case for a platinum-iridium nanoparticle imaged using a very low electron dose, in order to avoid radiation damage, discussed in [De Backer et al., 2015a]. Atoms could not be counted from the low dose images of such a nanoparticle. In chapter 6, we will experimentally show that atom-counting does become possible in the low dose image using the hybrid method, introduced in this chapter.

In an ideal situation, the results obtained by the statistics-only based method and the simulations-only based method agree perfectly. In other words, ideally the locations of the Gaussian mixture model are estimated equal to the scattering cross sections, i.e. the image intensities corresponding to the atomic columns, determined from very accurate image simulations. The hybrid method is introduced to enforce this necessity of finding the same results using either statistical parameter estimation theory or image simulations, and therefore combines elements of both existing methods. Since some inaccuracies may be present in the experimental input parameters needed for the image simulations, we cannot simply force the locations of the estimated Gaussian mixture models to exactly equal the scattering cross sections calculated from image simulations. However, we can propose a function that relates the experimental scattering cross sections to those determined from image simulations, with a parameter that can be estimated to take into account possible inaccuracies.

We therefore start the description of the hybrid method by proposing a relation between the experimental scattering cross sections and the simulated scattering cross sections, based on some examples of common calibration errors during experimental acquisition. This proposed function is then used to incorporate prior knowledge from image simulation into the estimates of the locations of the com-

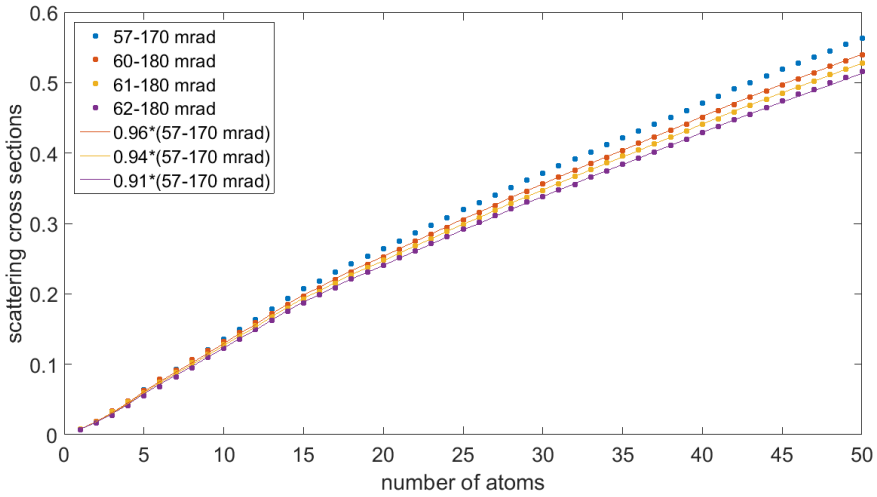

Figure 3.1: Simulated scattering cross sections for different detector settings for Au in [100] zone axis. In full lines, the scaled library for 57-170 mrad is shown, in nice agreement with libraries with different detector settings. Increasing detector inner angle causes a linear scaling of $a < 1$. Figure adjusted from [Martinez, 2014].

ponents of the Gaussian mixture model. This implies that locations are no longer freely estimated. Instead, the parameter describing the relationship between experimental and simulated intensities is estimated to determine the locations. Analytical updates for the new parameters are calculated by maximising the likelihood. Next, the likelihood of the estimated models is evaluated to examine the interpretation of the results obtained by the hybrid method. Finally, we introduce an order selection criterion and define its new interpretation in the context of the hybrid method.

3.1 Relationship between experimental and simulated scattering cross sections

When performing image simulations with the purpose of quantitative comparison to experimental results, it is of the utmost importance that all experimental parameters are measured correctly. The use of inaccurate parameters can cause the simulated scattering cross sections to deviate from the actual experimental scattering cross sections. However, since some inaccuracies can always be present, the goal of this section is to propose a relationship that describes this deviation due to common calibration errors of the experimental set-up. This relation can then be included in the hybrid method, in order to enable atom-counting even when some parameters may have been measured inaccurately.

In order to determine the relationship, we will look at two examples of parameters that are often measured slightly inaccurate during the experiment. The annular dark field detector inner angle (β_1 in figure 1.3) is a first example of the parameters used as input for the image simulations. Figure 3.1 shows the effect of detector angles that differ very little from each other (order of magnitude milliradians) on the atomic column intensities, quantified by the scattering cross sections. An increasing detector inner angle results in a global decrease of the scattering cross sections, which can be quite accurately approximated using a linear scaling relationship, as is shown by the full lines in figure 3.1. Assume for instance that the actual detector inner angle equals 57 mrad (blue in figure 3.1), while simulations were performed using a detector inner angle of 60 mrad (red in figure 3.1). In this case, a scaling parameter of 0.96 results in a nice agreement between the actual intensities and the simulated scattering cross sections and would allow us to compensate for the deviation of the scattering cross sections in the

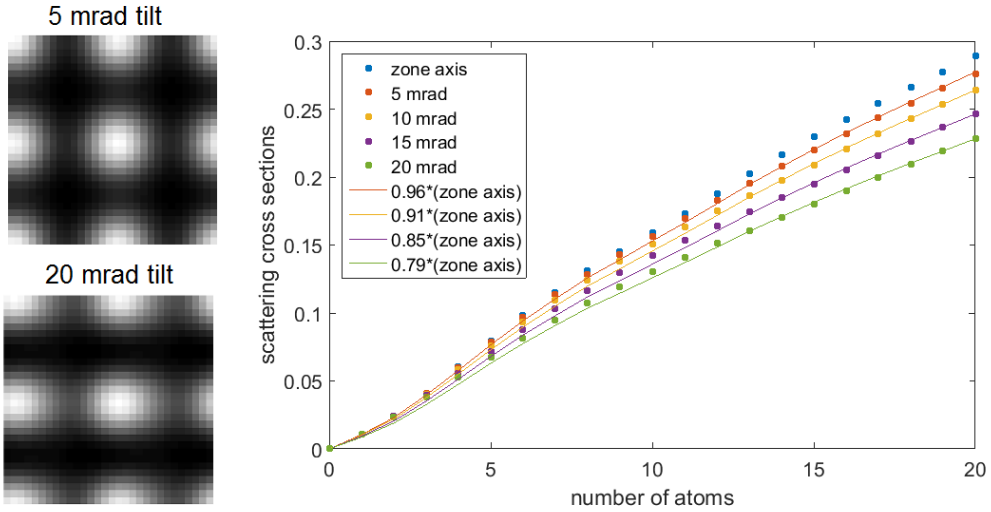

Figure 3.2: Simulated scattering cross sections for different values of the sample tilt. On the left, simulated images with 5 mrad and 20 mrad sample tilt are shown. On the right, in full lines, the scaled library for the sample in zone axis (no sample tilt) is shown, in nice agreement with libraries different tilt values, indicated by dots. Increasing sample tilt causes an (approximately) linear scaling of $a < 1$. Figure adjusted from [Martinez, 2014].

estimates for the locations of the Gaussian components in the mixture model.
Another example of a parameter which is often measured slightly inaccurately is sample tilt. Figure 3.2 shows image simulations for different values of the sample tilt and the effect on the scattering cross sections. Increasing sample tilt results in a decrease of the intensity belonging to an atomic column, again quantified by the scattering cross sections. This decrease can also be approximated as a linear scaling, as indicated in figure 3.2.
The previous analysis suggests that a linear scaling relationship can be incorporated into the statistical parameter estimation theory framework to account for the effects shown in these examples, together with other possible calibration errors. Therefore the key expression relating the existing image simulations-only based and statistics-only based atom-counting procedures is expressed by the following linear relationship:

$$\mu_g = a\mathcal{M}_g, \tag{3.1}$$

where μ_g represents the location of the g^{th} component, and $\mathcal{M}_g$ represents the simulated scattering cross section for a column with g atoms. The scaling parameter a determines the relationship between experimental and simulated intensities, and will be treated as a parameter that needs to be estimated along with the other parameters that determine the probability distribution of the scattering cross sections. The introduction of this linear scaling parameter opens up possibilities to correctly count atoms despite possible inaccuracies in the image simulations.
In the next section, the probability distribution of the scattering cross sections, and the way of incorporating the prior knowledge from the image simulations into the model will be discussed.

3.2 Probability distribution of the scattering cross sections

As mentioned before in section 2.3, the unavoidable presence of noise in the experimental images causes a probability distribution on the scattering cross sections. Represented in a histogram, we do not see isolated peaks corresponding to the different numbers of atoms in a column, but broadened components, often overlapping each other, as shown in figure 2.3c. Ideally, the average scattering

cross sections, in other words the locations of the components, coincide with the simulated scattering cross sections, called the library values since a set of simulated cross sections for different thicknesses is often called a library. Due to inaccuracies, the simulated scattering cross sections can deviate from the experimental scattering cross sections. This deviation was modelled as a linear scaling in the previous section, and will be incorporated into the expression for the locations of the components. Rather than freely estimating the locations, they will now be restricted to a linear scaling factor multiplied with the library values following from simulations.
The distribution of the scattering cross sections is modelled as a Gaussian distribution, analogous to the description given in section 2.3, but with the substitution $\mu_g = a\mathcal{M}_g$ to incorporate the library values $\mathcal{M}_g$ into the model. As compared to the statistics-only based method, where all the locations needed to be estimated, the number of parameters is now reduced by only estimating one scaling parameter to determine the locations. Instead of $2G$ parameters, only $G + 1$ parameters need to be estimated, summarised in the parameter vector:

$$\mathbf{\Psi}_G = (\pi_1, ..., \pi_{G-1}, a, \sigma)^T. \tag{3.2}$$

The updates of the parameters, previously expressed by equations (2.9), (2.10) and (2.11), are now calculated for the parameters of equation (3.2) using the following expressions:

$$\pi_g^{(k+1)} = \frac{1}{N}\sum_{n=1}^{N} \tau_g\left(\hat{V}_n; \psi_G^{(k)}\right), \tag{3.3}$$

$$a^{(k+1)} = \frac{\sum_{n=1}^{N}\sum_{g=1}^{G} \tau_g\left(\hat{V}_n; \psi_G^{(k)}\right)\hat{V}_n\mathcal{M}_g}{\sum_{n=1}^{N}\sum_{g=1}^{G} \tau_g\left(\hat{V}_n; \psi_G^{(k)}\right)\mathcal{M}_g^2}, \tag{3.4}$$

and

$$\sigma^{(k+1)} = \sqrt{\frac{1}{N}\sum_{g=1}^{G}\sum_{n=1}^{N} \tau_g\left(\hat{V}_n; \psi_G^{(k)}\right)\left(\hat{V}_n - a^{(k)}\mathcal{M}_g\right)^2}. \tag{3.5}$$

Elaborate derivations for these updates of the parameter estimates are presented in appendix A. Reliable starting values for the mixing proportions π_g and the width of the components σ are again expressed by equations (2.12) and (2.13). For the starting values of the scaling parameter, different values are used, ranging between a minimum and maximum expected scaling value. For each different set of starting values, the algorithm is iterated until convergence is reached. By evaluating the log likelihood as a function of the scaling value, as described in the next section, it will become clear that many starting values for the scaling parameters are in fact necessary in order for the algorithm to estimate the correct model. The estimates $\mathbf{\Psi}_G$ of the parameters in the mixture model are then given by the set of estimated parameters corresponding to the maximum likelihood. In chapter 4, simulations will be performed, showing that these starting values indeed result in accurate and precise parameter estimates.

An example of an estimated probability distribution of scattering cross sections obtained using the hybrid method is shown in figure 3.3. The scattering cross sections were created by performing random draws from a Gaussian mixture model with equal mixing proportions assigned to the first, second and fourth component, while the mixing proportion of the third component is equal to zero. This Gaussian mixture model is well-conditioned, with well-separated components and a large number of observations per component. Visually, it is clear that we are dealing with only 3 components in the mixture model. Due to the restrictions imposed on the locations by the hybrid method, a library length of 4 will be needed, as can be seen explicitly from 3.3, where the estimated Gaussian mixture models at library

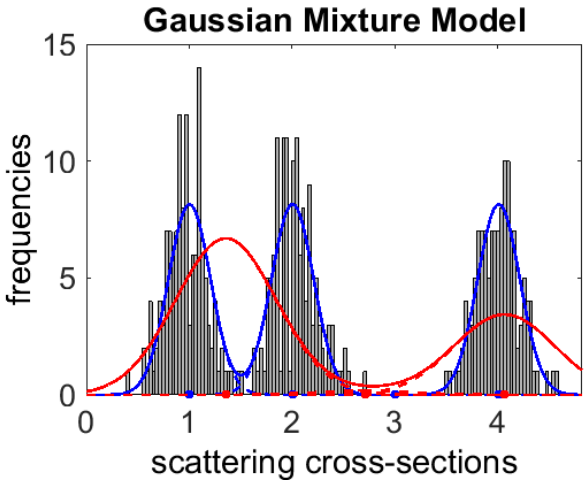

Figure 3.3: Simulated scattering cross sections with scaling value $a = 1$, relative width of components $\sigma = 0.2$, $N/G = 100$ observations per component, mixing proportions $\pi_1 = \pi_2 = \pi_4 = 1/3$ and the third component missing $\pi_3 = 0$, and a linear library. In red, the estimated mixture model by the hybrid method at library length 3 is shown. The estimated mixture model in blue corresponds to the model estimated at library length 4.

lengths 3 and 4 are shown in red and blue respectively. Therefore, we will speak of library length in the context of the hybrid method, since this is intuitively not necessarily the same as the number of components.

The fact that mixing proportions can be estimated equal to zero, which did not occur before because of the freedom in the estimation of the locations, means that this model with three effective, non-zero components at 1, 2 and 4 atoms thick can also be estimated using a library length larger than 4, by putting all mixing proportions from the fifth component onwards equal to zero. This will be used in the next section to evaluate the likelihood as a function of the scaling value on the one hand and as a function of the library length on the other hand. Ideally, based on the selection of the maximum likelihood, or equivalently the minimum negative log likelihood, the correct model is estimated.

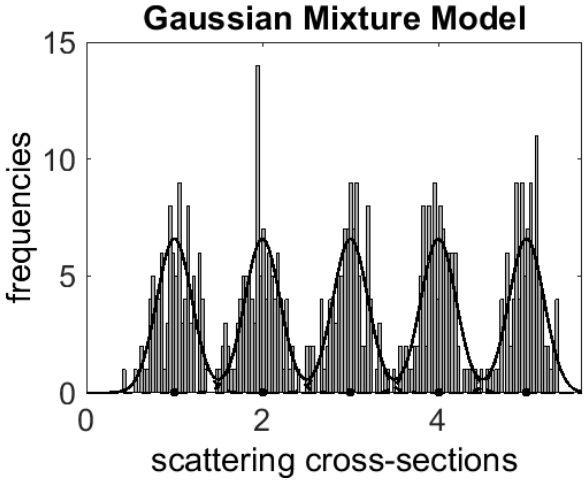

Figure 3.4: Simulated scattering cross sections created by performing random draws from a well-conditioned Gaussian mixture model, with $a = 1$, $\sigma = 0.2$, 5 uniform mixing proportions, $N = 500$ and a linear library. The imposed well-conditioned Gaussian mixture model is shown in black. The dots indicate the locations of the 5 imposed components, equal to the scaled library values.

3.3 Evaluation of the log likelihood

In order to examine the negative log likelihood, we will study an academic example, shown in figure 3.4. A set of scattering cross sections was simulated by performing random draws from a well-conditioned Gaussian mixture model with well-separated components and a large number of observations per component, with a linear library determining its locations. The negative log likelihood for the estimated models at library length 20 for the data shown in figure 3.4 is evaluated as a function of the scaling value in figure 3.5. The negative log likelihood was calculated by keeping the scaling value fixed throughout the estimation procedure, in order to really understand the behaviour of the negative log likelihood as a function of the scaling value. Estimates of the scaling parameter will converge to the nearest of the many local minima in the negative log likelihood as a function of the scaling parameter, because of the analytical implementation of the updates introduced in section 3.2. Therefore, many starting values for the scaling parameter are needed, in order to ensure convergence towards the correct model. After estimating models with many different starting values, the model with the highest likelihood (lowest negative log likelihood) is chosen.

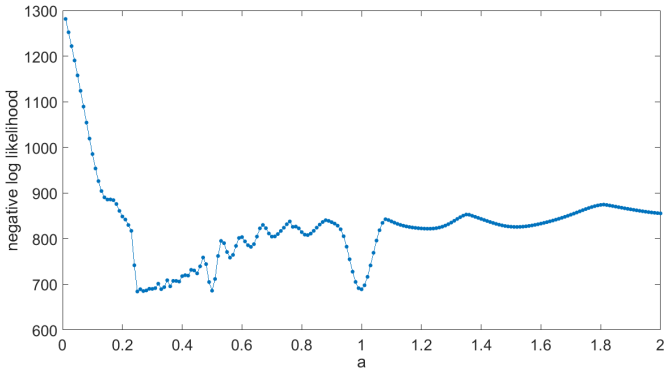

Figure 3.5: Negative log likelihood evaluated as a function of the scaling parameter for the estimated models at library length 20 for the data shown in figure 3.4. A lot of local minima occur, with a significant local minimum at $a = 0.9972$, and the global minimum at $a = 0.2510$.

A clear minimum in the negative log likelihood evaluated as a function of the scaling parameter in figure 3.5 occurs at $a = 0.9972$. The estimated Gaussian mixture model at this scaling value has only 5 mixing proportions estimated differently from zero. As predicted based on the example in figure 3.3, even though all library values upto 20 atoms thickness are used during the estimation procedure, the correct model can be found, because the mixing proportions can be estimated equal to zero. This model is shown in figure 3.6a.

The mixture model with five effective, non-zero components does however not result in the global minimum negative log likelihood as a function of the scaling parameter. The global minimum occurs at a scaling value of $a = 0.2510$. The model estimated at this scaling value is shown in figure 3.6b. More components are used, improving the fit to the data slightly, resulting in a higher likelihood, or equivalently a lower negative log likelihood, although this estimated model does not agree with the imposed mixture model. The dataset is overfitted by this model with 20 non-zero components.
Remarkably, the global minimum in the negative log likelihood as a function of the scaling value occurs at a quarter of the imposed scaling value, while using 4 times as many components to fit to the data. Furthermore, a local minimum occurs at $a = 0.4995$, using 10 effective non-zero components in the Gaussian mixture model. Because in this academic example the mixing proportions are uniform and the library is exactly linear, these models estimated at $a \approx 0.25$, $a \approx 0.5$ and $a \approx 1$, corresponding to 20, 10 and 5 components respectively, are equivalent in the sense that they can be regarded as

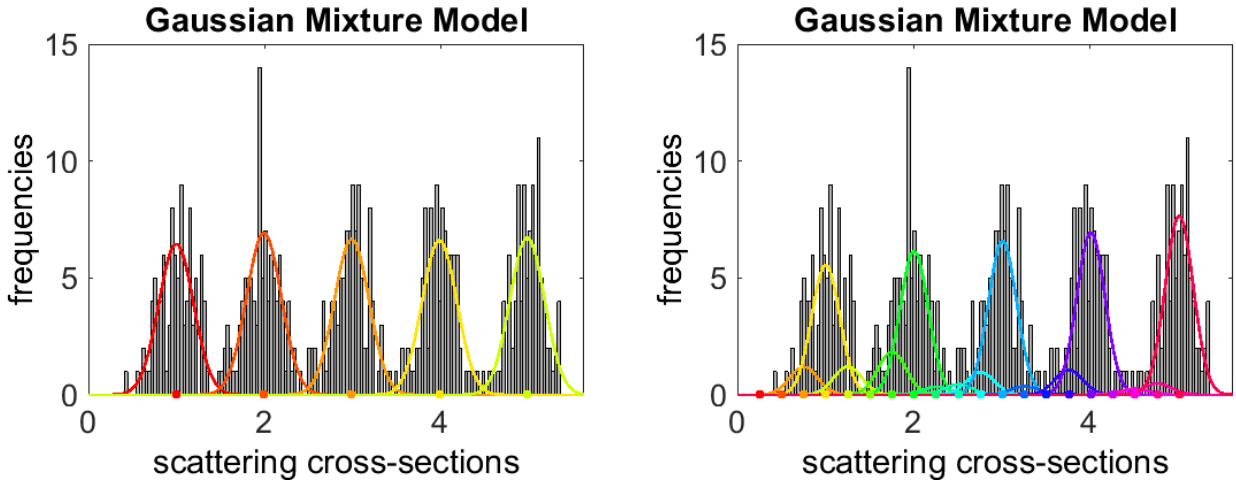

(a) (b)

Figure 3.6: Estimated Gaussian mixture models at (a) the local minimum at $a = 0.9972$ and (b) the global minimum at $a = 0.2510$ occurring in the negative log likelihood evaluated as a function of scaling parameter a for library length 20, as shown in figure 3.5. The model at $a = 0.9972$ only has 5 effective, non-zero components contributing to the mixture model, shown in (a), whereas all 20 components contribute to the mixture model in case a equals 0.2510 as can be seen from (b). The individual Gaussian components are shown in colours indicating the number of estimated atoms in an atomic column.

multiples of each other, where instead of one component, two or four were estimated with a similar likelihood. However, physically, only one of those models is significant. When all experimental set-up parameters used to perform image simulations were measured accurately, the scaling value is expected to be close to 1: experiment and simulations agree perfectly in the ideal case of $a = 1$. Therefore, out of all multiples of $a = 0.25$ corresponding to the global minimum, the value closest to the expected value of 1 should be chosen.

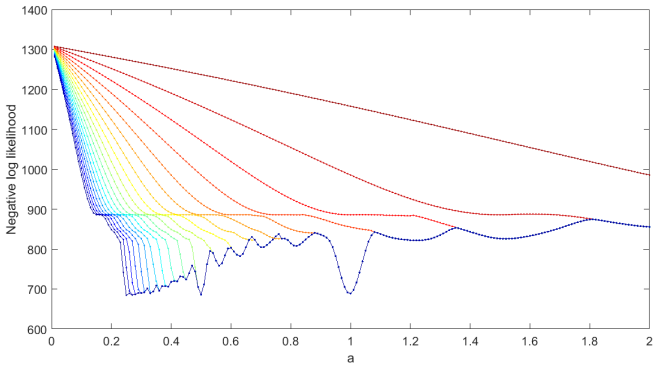

Figure 3.7: Negative log likelihood evaluated as a function of the scaling parameter for the estimated models at library lengths 1 upto 20 (red to blue) for the scattering cross sections from figure 3.4.

Figure 3.7 shows the negative log likelihood evaluated as a function of the scaling value for library lengths ranging from 1 to 20. It is clear that the local minima depend strongly on the library length. More minima appear when the library length increases, corresponding to the new possibilities that arise from having more components to fit to the data.

As mentioned earlier in section 2.1, experimental libraries are non-linear, due to channelling of the electrons when they propagate through the material [Fertig and Rose, 1981; Geuens and Van Dyck, 2005; Hawkes et al., 2007]. Therefore, a more realistic example will result in less likely combinations of a different number of scaled components in the mixture model, as compared to the academic example from figure 3.4. An example, with scattering cross sections simulated based on the estimated Gaussian mixture model of an actual Pt/Ir particle, with a non-linear library, is shown in figure 3.8. The minimum negative log likelihood around the expected value of $a = 1$, which was imposed on the Gaussian mixture model from which the scattering cross sections were simulated, is more difficult to interpret as the correct physically meaningful minimum based on this evaluation of the negative log likelihood as a function of the scaling value, calculated for a library length of 20, as compared to the previous academic example.

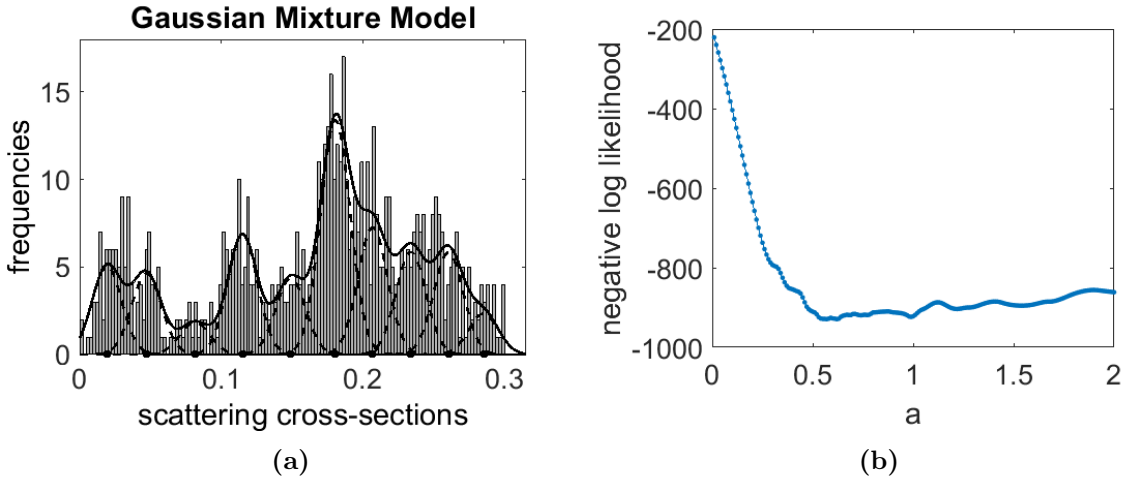

Figure 3.8: (a) Simulated scattering cross sections based on an estimated Gaussian mixture of a Pt/Ir nanoparticle. The imposed Gaussian mixture model is shown as a full black curve, whereas its individual components are black dashed lines. The dots on the x-axis indicate locations of the imposed components, in agreement with the (non-linearly increasing) library values, since a scaling value of $a = 1$ was imposed. (b) Negative log likelihood evaluated as a function of the scaling value, calculated at library length 20.

The negative log likelihood can also be evaluated as a function of the library length, as shown in figure 3.9, rather than as a function of the scaling parameter. The minimum negative log likelihood occurs at the largest library length, corresponding to the model where all components are used to form a mathematically likely fit to the data. At the true library length, the estimated model is indeed the same model that was estimated previously at the true scaling value, shown in figure 3.6a. However, the selection of the correct library length to determine the physically meaningful physical model based on the negative log likelihood is not possible. To facilitate the choice for the correct model, a selection criterion is introduced in the next section, that will penalise models with a high complexity and will therefore make it possible to choose the correct library length.

3.4 Assessing the maximum number of atoms in a column

The global minimum in the negative log likelihood will always occur at a small scaling value and a large library length, such that more components are used to produce a mathematically better fit to the data. A selection criterion can be used to determine the actual library length required to estimate a model with the correct balance between the goodness of fit, i.e. the likelihood of the model, and the complexity of the model. The selection criterion includes a likelihood term, as well as a penalty

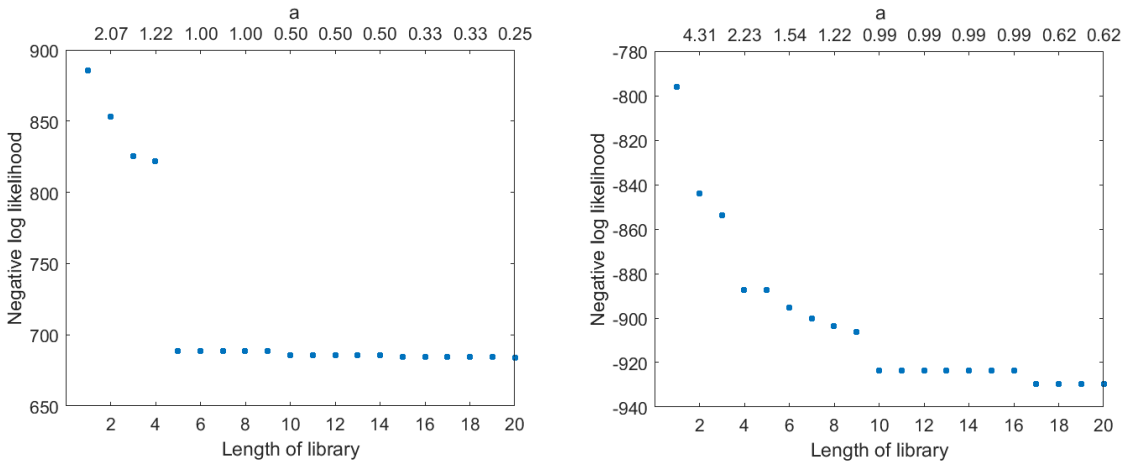

(a) **(b)**

Figure 3.9: Negative log likelihood evaluated as a function of the library length used to estimate the models, for the simulated scattering cross sections based on (a) a linear library, as displayed in figure 3.4 and on (b) a non-linear library, as displayed in figure 3.8a.

term which increases with the number of parameters in the Gaussian mixture model, in order to obtain a good trade off between the goodness of fit and the complexity of the model. Many different information criteria exist, accounting for the complexity of the model in different ways, for which an overview of relevant criteria is given by McLachlan and Peel [2000].
The Integrated Classification Likelihood (ICL) criterion (equation (2.14)) was shown to have the best performance for atom-counting for the statistics-only based method by De Backer et al. [2013]. The ICL criterion consists of a likelihood term $-2\log L(\hat{\mathbf{\Psi}})$, and a penalty term $2EN(\hat{\tau}) + d\log N$ depending on the complexity of the model. The parameter d represents the number of parameters to be estimated, equal to the length of library + 1. This means that increasing library length is penalised, while a higher likelihood is favoured. The reason for the good performance of the ICL criterion is the entropy term $EN(\hat{\tau})$, defined earlier in equation (2.15). The functional dependence on G represents the dependence of the library length for the hybrid method, instead of the number of components previously used in the statistics-only based atom-counting method from section 2.3.
The ICL criterion forms the ideal combination of the Bayesian Information Criterion (BIC) and the Classification Likelihood information Criterion (CLC), expressed by equations (3.6) and (3.7) respectively, which tend to respectively underestimate and overestimate the number of components of the probability distribution.

$$BIC(G) = -2\log L(\hat{\mathbf{\Psi}}_G) + d\log N \tag{3.6}$$

$$CLC(G) = -2\log L(\hat{\mathbf{\Psi}}_G) + 2EN(\hat{\tau}) \tag{3.7}$$

The evaluation of the BIC, CLC and ICL selection criteria as a function of the library length for a simulated set of cross sections with actual library length 51 is shown in figure 3.10. Indeed, the BIC underestimates the library length drastically, as indicated by the blue arrows in figures 3.10a and 3.10b. The CLC on the other hand slightly overestimates the correct library length as indicated in figure 3.10b by the red arrow. The extra $d\log N$ term depending on the number of estimated parameters present in the ICL criterion as compared to the CLC criterion, explains its optimal properties. Therefore, the ICL criterion will be used as an order selection criterion in the hybrid method.

The ICL criterion evaluated as a function of library length for the example from figure 3.4 with the linear library is shown in figure 3.11. The minimum of interest occurs at the global minimum at library

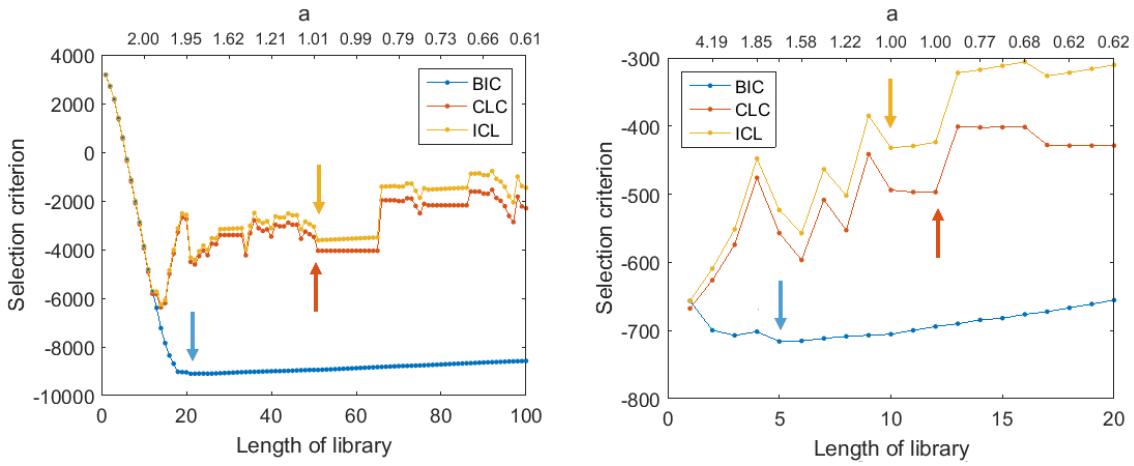

Figure 3.10: Evaluation of the Bayesian Information Criterion (BIC), the Classification Likelihood information Criterion (CLC) and the Integrated Classification Likelihood (ICL) criterion as a function of the library length for a simulated set of cross sections with actual library length (a) 51 and (b) 10 respectively. Arrows indicate the minima selected from the different selection criteria. The top axis evaluates the estimated scaling values. The BIC underestimates the library length drastically, whereas the CLC tends to overestimate the library length.

length 5, corresponding to an estimated scaling value of $a = 0.9972$, resulting in the correct choice of estimated Gaussian mixture model. In this example, the minimum of interest in the ICL criterion as a function of the library length coincides with the global minimum, thanks to the well-conditioned nature of the set of simulated scattering cross sections from figure 3.4. Notice that the estimated scaling values, shown at the upper axis in figure 3.4, remain constant from library lengths 5 upto 9. This implies the models estimated at these library lengths are effectively the same, while components with a mixing proportion equal to zero are added in the end. The ICL values from library lengths 5 upto 9 increase linearly with a slope equal to $\log N$, indicated by the grey lines in figure 3.11. At these library lengths, adding an extra component results in a model with the same likelihood, because the mixing proportion of this extra component is estimated equal to zero. The likelihood and entropy for these library lengths remain approximately constant, and only the number of parameters that need to be estimated d changes with increasing library length, since d equals the library length + 1. Therefore, these lines correspond to effectively the same models with the same scaling value, indicating the high likelihood of the model.

The minimum of interest chosen from figure 3.11 corresponds to the global minimum. This is however not a general property. Figure 3.12 shows the ICL criterion evaluated as a function of the library length for the more realistic example based on a non-linear library from figure 3.8. The interpretation of the ICL criterion evaluated as a function of the library length for the hybrid method to determine the correct library length can therefore be described by three guidelines. First of all, the minimum of interest usually is not the global minimum. Second, when image simulations are performed very carefully, the minimum can be chosen such that the estimated scaling value is close to the expected value of 1, which corresponds to perfect image simulations. Finally, in case one or more lines with slope $\log N$ occur in the ICL criterion, the equivalent models estimated at these library lengths have a very high likelihood. The extent of these lines can be used as an indication of the likelihood of the model, and will therefore aid the interpretation of the ICL criterion. In such cases, we choose the beginning of a line with slope $\log N$ as the minimum of interest.

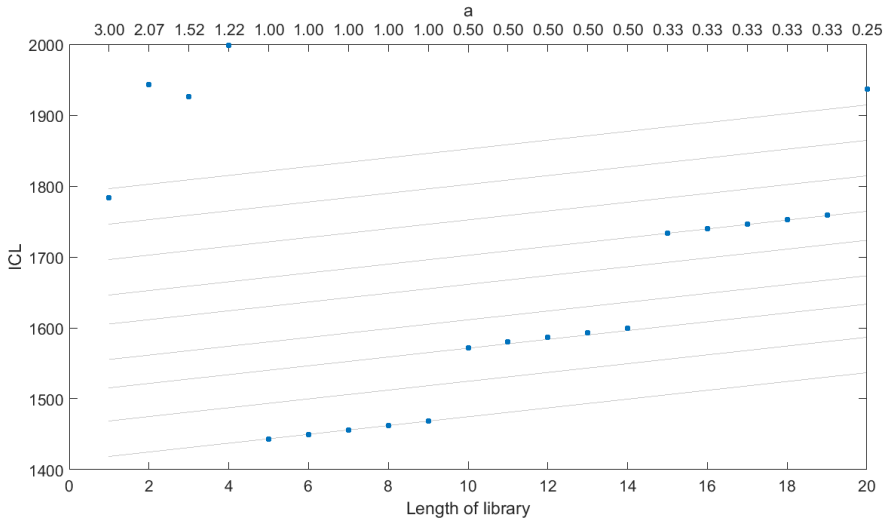

Figure 3.11: Integrated Classification Likelihood criterion evaluated as a function of library length (bottom axis) with corresponding estimated scaling values (top axis) for the scattering cross sections simulated by performing random draws from a **well-conditioned Gaussian mixture model with a linear library** from figure 3.4. The minimum of interest occurs at the global minimum at library length 5, corresponding to an estimated scaling value of $a = 1$, which corresponds to the correct imposed values.

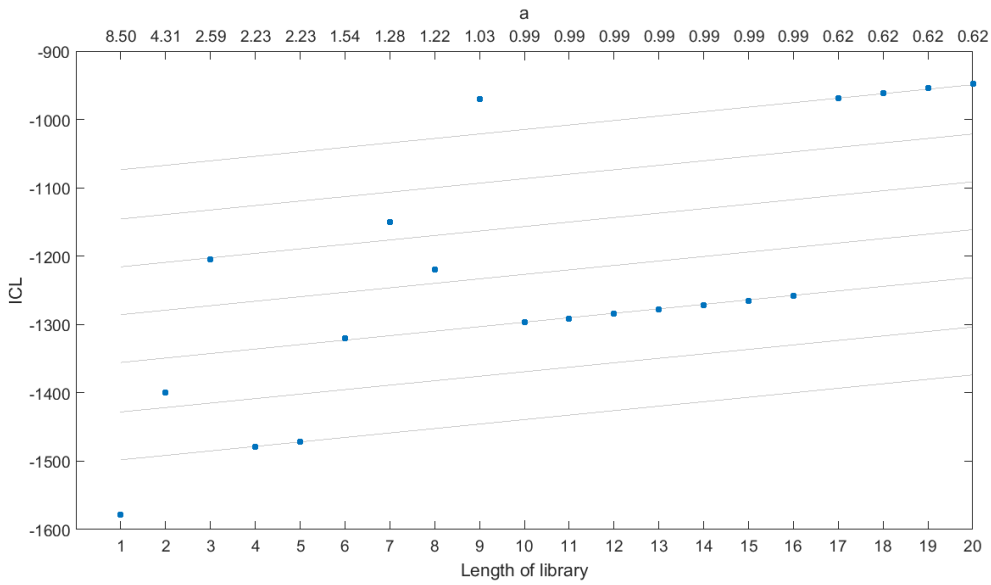

Figure 3.12: Integrated Classification Likelihood criterion evaluated as a function of library length (bottom axis) with corresponding estimated scaling values (top axis) for the scattering cross sections simulated by performing random draws from a **realistic Gaussian mixture model with a non-linear library** from figure 3.8. The minimum of interest occurs at a local minimum, at library length 10, corresponding to an estimated scaling value of $a = 0.99$, in good agreement with the imposed values.

3.5 Conclusion

In this chapter, the methodology of the hybrid statistics-simulations based atom-counting method for ADF STEM images of monatomic crystalline nanostructures was described. Image simulations were incorporated directly into the statistical parameter estimation theory framework by restricting the locations estimated in the Gaussian mixture model. In order to account for possible calibration errors during the measurements of parameters such as sample tilt and detector inner angle, the locations are expressed as a function of the simulated intensities. We have shown that such deviations result in a change of the intensities which can be approximated quite accurately by a linear scaling relationship. Therefore, a linear scaling relationship was used to incorporate the prior knowledge. Using this relationship, we derived new update formulas to be calculated during the Expectation-Maximisation algorithm in order to estimate the parameters of the Gaussian mixture model including the prior knowledge.

Next, we have shown that mixing proportions can be estimated equal to zero, whereas previously locations would have been shifted to compensate for missing components. This simplifies the interpretation of the atom-counts, since the g^{th} component used in the hybrid method will always correspond to g atoms in a column. Using the statistics-only based method, the relation between the number of the component and the number of atoms in a column corresponding to it had to be derived based on the distances between subsequent locations. An advantage of the hybrid method is therefore that missing components can more easily be detected.

The ability to estimate mixing proportions equal to zero also allows the correct model to be estimated at a larger library length. However, the negative log likelihood evaluated as a function of the scaling value, calculated at such a larger library length, exhibits a lot of local minima. For the academic example using a linear library, these local minima occur at fractions of the actual scaling value, determined by the library length. However for a more realistic example based on a non-linear library, we see that less minima occur and that the local minimum around the correct scaling value is less pronounced. Since more components in general result in a better fit to the data, with a slightly better likelihood than the correct model, the global minimum of the negative log likelihood occurs at a very small scaling value corresponding to a model with many components. Increasing the library length allows for overfitting of the dataset using a lot of components, as could clearly be seen by evaluating the negative log likelihood as a function of the library length.

To facilitate the selection of the correct model, a selection criterion evaluated as a function of the library length was introduced, in order to assess the maximum number of atoms in an atomic column. A selection criterion benefits from a high likelihood, but also penalises the complexity of the estimated models. The ICL criterion was chosen over other selection criteria, resulting in the best assessment of the model order. The minimum of interest from this criterion is selected based on three guidelines for its interpretation:

1. the minimum of interest is usually a local minimum,
2. the minimum is expected to correspond to an estimated scaling value close to the expected value of 1, and
3. the beginning of a long line with slope $\log N$ represents a model with a very high likelihood.

In the next chapter, the accuracy and precision of the estimated parameters of the Gaussian mixture model is studied. Furthermore, we look at the performance of the ICL criterion, and the percentage of correctly counted atomic columns for different conditions for the Gaussian mixture model.

Chapter 4

Possibilities and inherent limitations

In this chapter, the possibilities and inherent limitations of the hybrid statistics-simulations based method for atom-counting using ADF STEM images of monatomic crystalline nanostructures, developed in the previous chapter, will be discussed and compared to the performance of the statistics-only based method, introduced in chapter 2. We describe the precision of the estimated parameters using the so-called Cramér-Rao lower bound and validate the accuracy of the estimated parameters. Next, we study the atom-counting performance of the hybrid method. By performing simulations with known input parameters for the Gaussian mixture model, the percentage of correctly chosen minima in the ICL criterion evaluated as a function of library length and the percentage of correctly counted atomic columns will be studied as a function of the relative width of the components and the average number of observations per component. This will allow us to determine the new possibilities of the hybrid method, as well as its limitations.

4.1 Accuracy and precision of estimated parameters

We start this chapter by evaluating the accuracy and precision with which parameters can be estimated using the hybrid statistics-simulations based atom-counting method. The accuracy of the estimated parameters is validated by performing simulations. An analytical expression exists for the so-called Cramér-Rao lower bound on the variance of the estimated parameters. This lower bound expresses the highest possible attainable precision. Using the same set of simulations used to validate the accuracy, we determine the attainability of the Cramér-Rao lower bound.

4.1.1 Accuracy

A statistical estimator $\hat{\theta}$ is accurate when the expectation value of the estimator $\mathbb{E}_\theta(\hat{\theta})$ equals the actual value of the corresponding parameter θ: $\mathbb{E}_\theta(\hat{\theta}) = \theta$. Such an estimator is referred to as unbiased. In this section, we will validate the accuracy of the parameters estimated from the Gaussian mixture model in the hybrid method introduced in the previous chapter. To this purpose, 100 noise realisations were created by performing random draws from an imposed Gaussian mixture model with 5 components. The imposed Gaussian mixture model has a scaling value of $a = 1$, mixing proportions determined by multinomially distributed random draws from uniform proportions, a linear library in which the library value corresponds to the number of atoms in a column, and a width of the components equal to $\sigma = 0.25$. The average number of observations per component equals $N/G = 20$. Table 4.1 summarises the imposed values of the parameters π_g, a and σ. The parameters were estimated using the hybrid method with the starting values for the mixing proportions π_g and the width of the components σ formulated by equations (2.12) and (2.13) respectively. As discussed in the previous chapter, many starting values for the scaling parameter a are needed, with small increments. Therefore, the starting

Parameter	Expectation value	Sample mean	95% confidence interval
π_1	0.2	0.2024	[0.1943; 0.2105]
π_2	0.2	0.2022	[0.1953; 0.2091]
π_3	0.2	0.1957	[0.1883; 0.2031]
π_4	0.2	0.1969	[0.1889; 0.2049]
π_5	0.2	0.2028	[0.1943; 0.2113]
a	1	0.9979	[0.9979; 1.0024]
σ	0.25	0.2488	[0.2446; 0.2530]

Table 4.1: Parameter estimates of the unknown parameters that determine a Gaussian mixture model with 5 components were calculated for 100 noise realisations. The expectation values as well as the average of the estimated values, the sample mean, for each parameter with its 95% confidence intervals are summarised. Parameter estimates are determined using the correct library length.

values used to estimate these models ranged from $a = 0.01$ to $a = 2$ in increments of 0.01. The results of the estimated parameters at the correct library length are summarised in table 4.1. Notice that the sample means, i.e. the average of the estimated values of the parameters, deviate only slightly from the expectation values. Furthermore, all expectation values fall within the 95% confidence interval of the sample mean. We conclude that the parameter estimates for this Gaussian mixture model using the starting values mentioned above are indeed accurate.

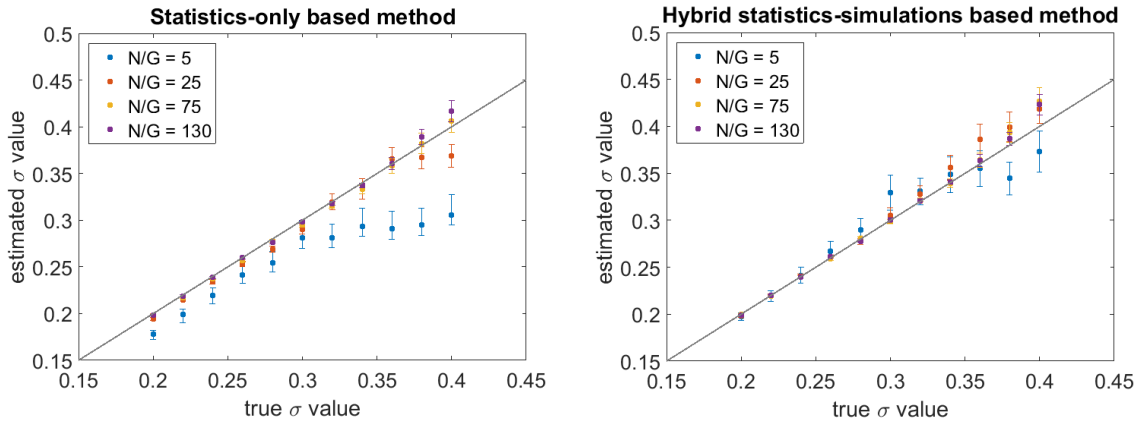

(a) **(b)**

Figure 4.1: Estimates of σ values for different values of N/G, estimated by (a) the statistics-only based method and (b) the hybrid statistics-simulations based method. The diagonal grey line indicates the correctly estimated σ values. Parameter estimates are determined after evaluation of the ICL criterion.

The sample means presented in table 4.1 are calculated using the correct library length, and are therefore more accurate than the estimated parameters would be in case we still had to select the library length, because this is generally not known a priori. Therefore, the mean estimated width of the components after an evaluation of the ICL criterion is evaluated as a function of the true width of the components in figure 4.1. Error bars show 95% confidence intervals on the estimated mean σ values. The minimum in the ICL criterion was automatically selected between 8 and 12, a range of ± 2 around the actual library length of 10. For a small number of columns per component N/G, the value of σ is heavily underestimated by the statistics-only based method, as shown in figure 4.1a. This is an important disadvantage of the statistics-only based method, which is overcome by using the hybrid method. As shown in figure 4.1b, the value of σ estimated by the hybrid method stays closer to the correct value up until a higher amount of overlap between the Gaussian components. Furthermore,

when N/G is increased, the accuracy of the estimates of σ improves faster using the hybrid method as compared to using the statistical method. This implies that the hybrid method allows for a more accurate estimate of the overlap between Gaussian components.

4.1.2 Precision

For unbiased estimators, a lower bound on the variance, i.e. a maximum attainable precision, exists. In this section, we will study the attainability of this lower bound for the different parameters estimated from the Gaussian mixture model using the hybrid method. The lower bound on the variance is defined by the Cramér-Rao lower bound:

$$\mathrm{cov}(\mathbf{\Psi}_G) \geq F_{\mathbf{\Psi}_G}^{-1}, \tag{4.1}$$

with $\mathbf{\Psi}_G$ the vector containing the estimators, and $F_{\mathbf{\Psi}_G}$ the Fisher information matrix, which is defined as follows:

$$F_{\mathbf{\Psi}_G} = -\mathbb{E}\left[\left.\frac{\partial^2 \ln p(\mathbf{V};\mathbf{\Psi}_G)}{\partial \mathbf{\Psi}_G \partial \mathbf{\Psi}_G^T}\right|_{\mathbf{\Psi}_G=\mathbf{\Psi}_0}\right], \tag{4.2}$$

where $\mathbb{E}$ expresses the expectation value. In this expression, $p(\mathbf{V};\mathbf{\Psi}_G)$ represents the joint probability density function, here determined by the Gaussian mixture model $f_{\mathrm{mix}}(\mathbf{V};\mathbf{\Psi}_G)$, defined in equation (2.4), which describes the probability distribution of the set of scattering cross sections $\mathbf{V}$, and is determined by the unknown parameters expressed by the parameter vector $\mathbf{\Psi_G}$. The vector $\mathbf{\Psi}_0$ contains the actual values of the parameters to be estimated. In practice, the following integral is numerically integrated:

$$F_{\mathbf{\Psi}_G} = -N\int_{-\infty}^{\infty} \left.\frac{\partial^2 \ln f_{\mathrm{mix}}(V;\mathbf{\Psi}_G)}{\partial \mathbf{\Psi}_G \partial \mathbf{\Psi}_G^T}\right|_{\mathbf{\Psi}_G=\mathbf{\Psi}_0} f_{\mathrm{mix}}(V;\mathbf{\Psi}_G)dV, \tag{4.3}$$

where N represents the total number of columns in the image. A derivation of the Cramér-Rao lower bound for the parameters of the Gaussian mixture model, is given in appendix B.
As shown in section 4.1.1, the estimators for the unknown parameters that determine the Gaussian mixture model are unbiased. To determine the precision of these estimators, the same 100 noise realisations used to determine the accuracy of the estimators were used. The average parameter estimates obtained at the correct library length by the hybrid method from these 100 noise realisations were already summarised in table 4.1. Table 4.2 summarises the variances of these parameter estimates, together with a 95% confidence interval and the Cramér-Rao lower bound for each parameter. We conclude that the Cramér-Rao lower bound is attained, since the 95% confidence interval on the sample variances include the Cramér-Rao lower bound.
As a consequence of its attainability, combined with the improved accuracy of the estimate for the width of the components shown in section 4.1.1, the Cramér-Rao lower bound can now be used to predict the expected precision of estimated parameters from unknown datasets. This is a very interesting advantage of the hybrid statistics-simulations based method.

4.2 Atom-counting performance

The atom-counting performance of the hybrid method can be examined in two ways. We can either evaluate the percentage of the correct selection of the model order based on the ICL criterion, or the percentage of correctly assigned atom-counts to specific atomic columns. These performance measures will be studied as a function of the conditions of the Gaussian mixture model, determined

Parameter	CRLB	Sample variance	95% confidence interval
π_1	0.0017	0.0017	[0.0013; 0.0023]
π_2	0.0018	0.0012	[0.00094; 0.0016]
π_3	0.0018	0.0014	[0.0011; 0.0019]
π_4	0.0018	0.0016	[0.0013; 0.0022]
π_5	0.0017	0.0018	[0.0014; 0.0025]
a	0.000098	0.00013	[0.000098; 0.00017]
σ	0.00044	0.00045	[0.00035; 0.00060]

Table 4.2: Attainability of the Cramér-Rao lower bound on the estimated parameters of a Gaussian mixture model with 5 components. The sample variances are computed from parameter estimates obtained from 100 well-conditioned noise realisations of the Gaussian mixture model. The Cramér-Rao lower bound (CRLB) is attained when its value is included in the 95% confidence interval on the sample variance.

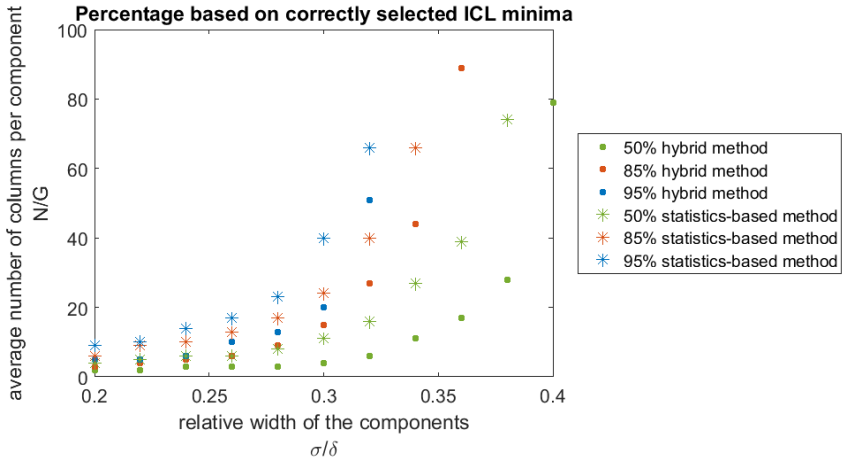

Figure 4.2: Percentage of **correctly chosen minima in the ICL criterion** between library lengths 8 and 12 for 100 noise realisations per Gaussian mixture model with a σ/δ and N/G combination, with an actual length of library equal to 10.

by the relative width of the components σ/δ and the average number of columns per component N/G. Furthermore, a direct comparison with the performance of the statistics-only based atom-counting method will be performed, in order to verify whether the hybrid method does indeed outperform this existing method at conditions corresponding to images of small nanoparticles recorded with a very low electron dose.

4.2.1 Performance of the ICL criterion for model order selection

In order to study the performance of the ICL criterion, scattering cross sections are simulated by performing random draws from Gaussian mixture models with 10 components, mixing proportions determined by multinomially distributed draws from uniform proportions, a scaling value equal to $a = 1$, and a linear library with library values equal to the number of atoms in a column. These scattering cross sections are analysed using both the hybrid method and the statistics-only based method. The values of σ and N, which determine the conditions for atom-counting, are varied. The percentage of correctly chosen minima from the ICL criterion from a 100 noise realisations for each N and σ combination, after evaluation of the ICL criterion between library lengths of ± 2 around the true model order, is displayed in figure 4.2. Here, the average number of columns per component N/G required to reach 50%, 85% and 95% correct selection of the ICL minimum is evaluated as a function of the relative width of the components σ/δ. The percentage of correctly determined ICL minima

can be increased by increasing the average number of columns per component and by decreasing the relative width of the components. However, the required N/G to reach a given percentage with the hybrid method is lower than the N/G needed to reach the same percentage using the statistics-only based method for constant σ/δ.
In other words, the hybrid method does indeed outperform the statistics-only based method, and the most significant improvement is achieved at high values for σ/δ. This suggests the possibility of counting atoms in samples where counting was previously impossible, especially for images of small, beam-sensitive particles recorded using a low electron dose.

4.2.2 Percentage of correctly counted atomic columns

Figure 4.3 shows the results of a similar analysis to the one performed above to obtain figure 4.2. This time, the required values of N/G to reach 50%, 85% and 95% correctly counted atomic columns is evaluated as a function of σ/δ. Using the hybrid method, rather than the statistics-only based method, an increase in the percentage of correctly counted atomic columns is achieved. This increased percentage is most significant at high values for σ/δ, as was also the case for the percentages of correctly chosen minima from the ICL criterion.

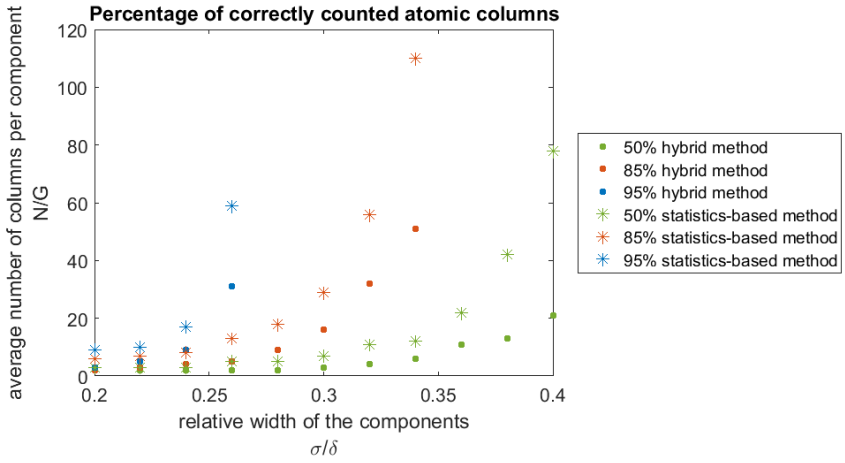

Figure 4.3: Percentage of **correctly counted atomic columns**, after choosing minima in the ICL criterion between library lengths 8 and 12 for 100 noise realisations per Gaussian mixture model with a σ/δ and N/G combination, with an actual length of library equal to 10.

It is worth mentioning that 100% correctly chosen minima from the ICL criterion, does not imply that every single atomic column is counted correctly. For example, at $N/G = 5$ and $\sigma/\delta = 0.2$, the percentage of correct minima selected from the ICL criterion already equals 100%, whereas the percentage of correctly counted atomic columns equals 98.82% under the same conditions. This is an inherent property of the Gaussian mixture model, caused by the overlap between neighbouring Gaussian components. The value at which two Gaussian components, weighed by mixing proportions π_1 and π_2, with equal widths $\sigma_1 = \sigma_2 = \sigma$ intersect is given by:

$$x_{1,2} = \frac{\mu_1 + \mu_2}{2} - \frac{\sigma^2}{\mu_2 - \mu_1} \ln\left(\frac{\pi_2}{\pi_1}\right), \tag{4.4}$$

or in general

$$x_{j,j+1} = \frac{\mu_j + \mu_{j+1}}{2} - \frac{\sigma^2}{\mu_{j+1} - \mu_j} \ln\left(\frac{\pi_{j+1}}{\pi_j}\right), \tag{4.5}$$

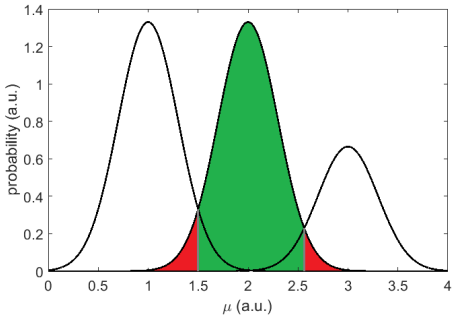

Figure 4.4: Overlapping Gaussian components cause an inherent upper bound on the percentage of correctly counted atomic columns. Columns with a scattering cross section in the green areas are correctly assigned to the second component in this example. Columns with scattering cross sections in the red regions on the other hand are counted wrongly by ±1 atom.

indicated by the grey vertical lines in figure 4.4. The probability F_2 of falsely assigning an atom-count of 1 or 3 to a column that belongs to the second component can therefore be expressed as follows:

$$F_2 = \pi_2 \left[P\left(x \leq x_{1,2}; \mu_2, \sigma\right) + P\left(x \geq x_{2,3}; \mu_2, \sigma\right) \right], \tag{4.6}$$

or in general

$$F_j = \pi_j \left[P\left(x \leq x_{j-1,j}; \mu_j, \sigma\right) + P\left(x \geq x_{j,j+1}; \mu_j, \sigma\right) \right], \tag{4.7}$$

with j ranging from 2 to $G-1$. The first and last component need to be treated slightly different, since they only overlap with one component. The total probability of miscounting an atomic column, i.e. the total overlap area between the subsequent components of the Gaussian mixture model, can be expressed as follows:

$$F = \sum_{j=2}^{G-1} F_j + \pi_1 P\left(x \geq x_{1,2}; \mu_1, \sigma\right) + \pi_G P\left(x \leq x_{G-1,G}; \mu_G, \sigma\right). \tag{4.8}$$

The probability of correctly counting atoms from a Gaussian mixture model equals 1 - the total overlap area:

$$U = 1 - \sum_{j=2}^{G-1} F_j - \pi_1 P\left(x \geq x_{1,2}; \mu_1, \sigma\right) - \pi_G P\left(x \leq x_{G-1,G}; \mu_G, \sigma\right), \tag{4.9}$$

where $\mu_j = a\mathcal{M}_j$ in the specific case of the hybrid method, with $\mathcal{M}_j$ the library values. For uniform mixing proportions, the expression for the upper bound simplifies further, because

$$x_{j,j+1} = \frac{\mu_j + \mu_{j+1}}{2}, \tag{4.10}$$

since $\ln\left(\frac{\pi_j+1}{\pi_j}\right) = \ln(1) = 0$. Equation (4.9) determines the theoretical upper bound on the percentage of correctly counted atomic columns. Figure 4.5 shows this theoretical upper bound, together with the calculated percentages from simulations. For a small relative width of components σ/δ, the upper bound of correctly counted atomic columns is attained, regardless of the average number of columns per component N/G. However, at higher σ/δ values, the theoretical upper bound is only reached for datasets with high values of N/G, i.e. large nanoparticles. The upper bound can therefore be used to predict the expected percentage of correctly counted atomic columns in large particles using

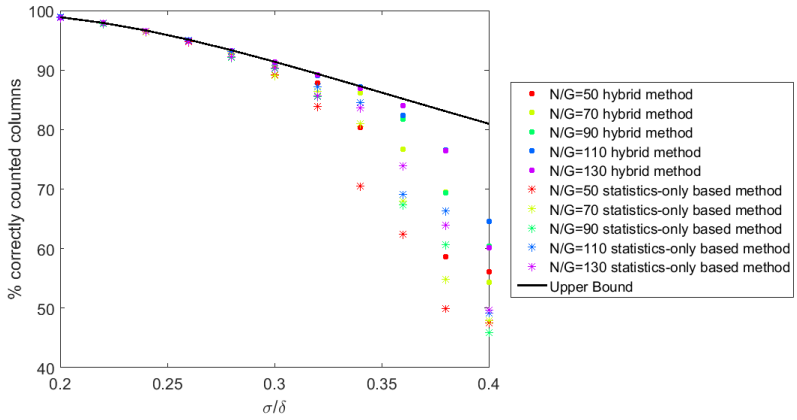

Figure 4.5: Theoretical upper bound of the percentage of correctly counted atomic columns, and calculated percentages for 100 noise realisations of Gaussian mixture models with different N/G values as a function of σ/δ, with uniform mixing proportions, $a = 1$, a linear library and 10 uniform components.

the estimated width of the components. This is possible thanks to the more accurate estimates for the width of the components, as shown in section 4.1.1, and will be applied in chapter 5 to a large gold nanorod. Since the percentages of correctly counted columns differ more strongly from the upper bound when using the statistics-based method as compared to the hybrid method, predicting the percentage using the upper bound is most reliable when using the hybrid method.
When the average number of columns per components N/G is smaller, the upper bound is no longer reached. At low N/G and high σ/δ values, the number of components/library length is underestimated and a wrong model is estimated to the scattering cross sections. The expected percentages of correctly counted columns can be determined for such smaller particles, by using simulated cross sections in the same way that lead to the results in figure 4.3, rather than with the upper bound, as will be applied in chapter 6 for small platinum-iridium nanoparticles.

So far, we have studied simulated scattering cross sections that were created by performing random draws from Gaussian mixture models with locations determined by a linear library. However, experimental libraries are not exactly linear, due to channelling of the electrons when propagating through the sample [Fertig and Rose, 1981; Geuens and Van Dyck, 2005; Hawkes et al., 2007]. We have seen in chapter 3 that many local minima exist in the negative log likelihood evaluated as a function of the scaling value, at 3/2, 1/2, 1/4,... of the true scaling value, directly related to the number of effective components used in the estimated models. We have also shown that less such minima exist when working with a non-linear library, reducing the number of likely models to be estimated. Hence, higher percentages of correct model order selection and atom-counts are expected when the library is non-linear. The results of simulations for Gaussian mixture models with $\sigma/\delta = 0.36$ and $N/G = 14$ using a non-linear platinum library are summarised in table 4.3. The percentage of correctly chosen minima from the ICL criterion to determine the model order using the statistics-only based method decreases significantly when a non-linear library is used instead of a linear library, whereas this percentage increases using the hybrid method. The entropy term in the expression for the ICL criterion (equation (2.14)) prefers evenly separated components, which is only possible when locations are estimated freely, but also results more often in a wrong model based on the minimum in the ICL criterion. The percentage of correctly counted atomic columns increases for both methods.
As can be seen from table 4.3, this increase is not enormous, such that the results obtained in this chapter using a linear library can be regarded as a reasonable lower limit on the expected performance of the hybrid method using a non-linear library. A more detailed prediction of the percentages to be expected given a specific library can be obtained by simulating scattering cross sections and

Method	Percentage based on	Linear library	Non-linear library (Pt)
Statistics-only based	ICL minimum	29	15
Hybrid	ICL minimum	36	42
Statistics-only based	Atom-counts	48	52
Hybrid	Atom-counts	53	60

Table 4.3: The effect of a non-linear library on the percentages of correct model order selection based on the selection of the minimum from the ICL criterion and percentages of correctly counted atomic columns is summarised for both the hybrid method and the statistics-only based method for atom-counting, calculated for 100 noise realisations from Gaussian mixture models with $\sigma/\delta = 0.36$ and $N/G = 14$.

constructing analogous figures to figure 4.3.
The number of likely models that can be estimated to a dataset is further reduced when there are missing components, for which mixing proportions are estimated equal to zero as shown in chapter 3. Therefore, percentages for such mixture models are also expected to be higher than those achieved in figure 4.3.

4.3 Conclusion

In this chapter, we have studied the limitations and the new possibilities for atom-counting using the hybrid statistics-simulations based method. We have shown that the estimates of the unknown parameters are unbiased and in particular that the width of the components is estimated much more accurately using the hybrid method as compared to using the statistics-only based method. Furthermore, the estimates are found to be most precise, because the Cramér-Rao lower bound on the variance is attained. Thanks to the improved accuracy of the parameter estimates, the Cramér-Rao lower bound can be used to reliably predict the precision of the estimated parameters.
We have also studied the performance of the hybrid method for atom-counting. The percentage of correctly chosen minima from the ICL criterion as well as the percentage of correctly counted atomic columns were examined. For very well-conditioned datasets, i.e. a large average number of components per column N/G and a small relative width of the components σ/δ, the atom-counting performance of the purely statistics-only based atom-counting method is matched by the hybrid method. However, at high σ/δ values and low N/G values, corresponding to small particles imaged with a low electron dose, the performance of the hybrid method far exceeds that of the statistics-only based method.
Finally, we calculated the inherent theoretical upper bound on the percentage of correctly counted atomic columns, caused by the overlap between the Gaussian components, determined by σ/δ. For small relative widths of the components σ/δ, the upper bound is attained. For models with more overlap, a higher average number of columns per component N/G is required to reach this upper bound. An advantage of the hybrid statistics-simulations based method is that less N/G is required for the hybrid method to reach the upper bound at such high overlap values as compared to the statistics-only based method.

In conclusion, the hybrid method for atom-counting developed in this thesis not only offers great possibilities for atom-counting in challenging low dose ADF STEM images of small nanoparticles, but also allows one to predict the precision of the estimated parameters as well as the expected percentage of correctly counted atomic columns.
We will apply the hybrid method to a very well-conditioned experimental example in chapter 5 on the one hand, and to a very challenging experimental example with conditions in the range where the most significant improvement by the hybrid method is expected in chapter 6 on the other hand.

Chapter 5

Case study: Au nanorod

Noble metal nanoparticles have size-dependent properties that make them very interesting for a variety of electronic, optical, and biomedical applications. Gold nanorods display two surface plasmon resonance bands thanks to their anisotropic shape, one due to light absorbed along the short axis (transverse) and the other due to absorption along the long axis (longitudinal). As the rod length increases, the absorption of the longitudinal band can be shifted towards (near) infrared light. This ability to absorb near infrared light, makes the gold nanorods particularly useful for biomedical applications, such as drug delivery. Gold nanorods are useful materials for sensing, photothermal therapy, and imaging, thanks to the size-dependent properties [Vigderman et al., 2012; Stone et al., 2011]. In other words, the exact size of the rod determines its properties. In this chapter, a gold (Au) nanorod imaged along the [100] zone axis using a double aberration-corrected FEI TITAN operated at 300 kV is analysed using the statistics-only based atom-counting method and the hybrid statistics-simulations based method. The experimental image of this Au nanorod is shown in figure 5.1a. The histogram of scattering cross sections, calculated from the refined model of the experimental image as explained in section 2.3, is shown in figure 5.1b. The atoms in this Au nanorod could already be counted reliably using the statistics-only based atom-counting method by Van Aert et al. [2013]. Therefore, this well-conditioned experimental example will be used to compare the results obtained by both atom-counting methods.

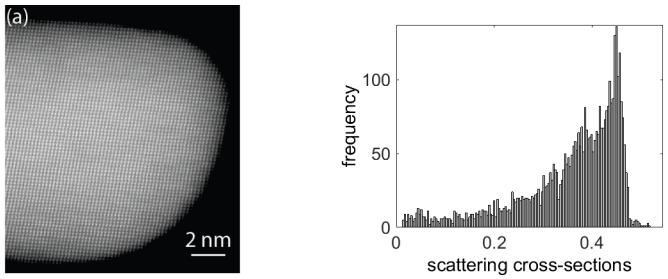

(a) **(b)**

Figure 5.1: (a) Experimental image of a gold nanorod imaged along the [100] zone axis using a double aberration-corrected FEI TITAN operated at 300 kV. (b) Histogram of calculated scattering cross sections.

The analysis using the statistics-only based method is shown in figure 5.2. The ICL criterion in figure 5.2b reveals the presence of 47 components. The histogram of scattering cross sections is shown in figure 5.2c, together with the estimated probability distribution with 47 Gaussian components, shown as a full curve in black. The individual components are indicated in colours ranging from blue to red, on the same scale as the atom-counts, shown in figure 5.2a for each atomic column, overlaying the observations.

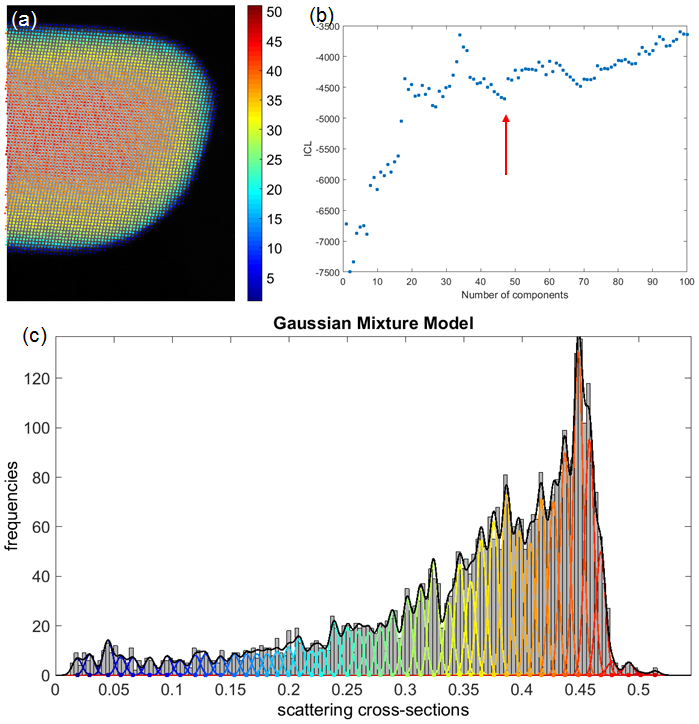

Figure 5.2: Analysis of the Au nanorod using the **statistics-only based method**. (a) Atom-counts overlaying the observations. (b) ICL criterion evaluated as a function of the number of components. The minimum of interest occurs at 47 components. (c) Estimated Gaussian mixture model overlaying the histogram of scattering cross sections. The full black line indicates the estimated Gaussian mixture model, whereas the individual components are plotted in colours, on the same scale as the colour bar of the atom-counts. The dots on the cross sections axis indicate the estimated locations.

The analysis performed with the hybrid statistics-simulations based method, developed in this thesis, is shown in figure 5.3. The ICL criterion is evaluated as a function of the library length in figure 5.3b, with a top axis indicating the estimated scaling parameters. In chapter 3, the interpretation of the ICL criterion obtained with the hybrid method was discussed. We concluded that the minimum of interest from the ICL criterion need not be the global minimum and preferably coincides with a scaling parameter close to the expected value of 1. Furthermore, a feature specific to the hybrid ICL criterion was discussed, namely the lines that increase with a slope of $\log N$ when the library length increases. The meaning of these lines was revealed by examining the expression of the ICL criterion, and we concluded that these lines indicate a very likely model, since adding components with zero mixing proportions is preferred over changing the model by shifting all components and adding an extra component with a non-zero mixing proportion. The ICL criterion calculated for this Au nanorod contains two such lines with slope $\log N$, starting at library lengths 34 and 51. The corresponding scaling parameters are $a = 1.44$ and $a = 0.99$ respectively. Notice that the ratio between the library lengths approximately equals the inverse ratio between the estimated scaling parameters: $\frac{34}{51} = 0.67 \approx \frac{0.99}{1.44} = 0.69$, which was also a feature that can aid the interpretation of the ICL criterion, as discussed in chapter 3. Considering all these interpretation guidelines, we conclude that the minimum of interest in the ICL criterion corresponds to library length 51. The estimated Gaussian mixture model is shown in figure 5.3c overlaying the histogram of scattering cross sections. The individual Gaussian components are indicated in different colours, again ranging from blue to red, on the same colour scale as previously used for the statistics-only based analysis. The atom-counts corresponding to the model are also shown on this colour scale, in figure 5.3a.

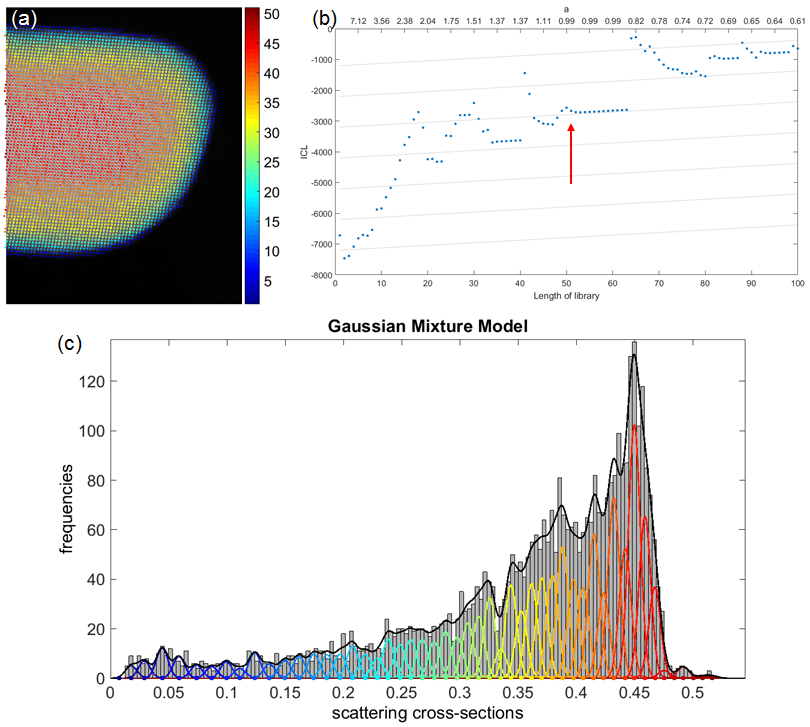

Figure 5.3: Analysis of the Au nanorod using the **hybrid statistics-simulations based method**. (a) Atom-counts overlaying the observations. (b) ICL criterion evaluated as a function of the library length, with a second axis indicating the estimated scaling values. In light grey, the lines with slope $\log N$ are indicated to facilitate interpretation (see chapter 3). The minimum of interest occurs at library length 51, at the beginning of the longest line with slope $\log N$. (c) Estimated Gaussian mixture model overlaying the histogram of scattering cross sections. The full black line indicates the estimated Gaussian mixture model, whereas the individual components are plotted in colours, on the same scale as the colour bar of the atom-counts. The dots on the cross sections axis indicate the estimated locations, equal to the scaled library values.

There is a noticeable difference between the Gaussian mixture models estimated by both methods. Table 5.1 summarises the N/G, σ/δ, negative log likelihood values and total number of atoms counted from the image for both methods. The negative log likelihood of the Gaussian mixture model estimated by the statistics-only based method is lower than the negative log likelihood corresponding to the model estimated by the hybrid method. In other words, the model estimated with 47 components with free locations represents a mathematically better fit to the data than the model with 51 components with restricted locations. However, the mathematically more likely model is not necessarily the most correct model. Using the library to incorporate prior knowledge about the material, less freedom is allowed in the model, keeping it closer to the physically correct model. This effect can also be observed from the intensity/thickness graph from figure 5.4a. The estimated locations by the statistics-only based method, as well as the scaled library values estimated by the hybrid method are evaluated as a function of the number of atoms in an atomic column. The origin of the difference between both methods lies in channelling theory which is explicitly incorporated in the hybrid method through the use of image simulations, but is not incorporated into freely estimated locations.

Notice also the significant difference in estimated σ/δ by both methods, as listed in table 5.1. As shown in section 4.1.1, the statistics-only based method underestimates the width of the components σ at large actual widths. The sensitivity of the atom-counting procedure was therefore previously overestimated. In section 4.1.2 it was shown that thanks to the increased accuracy of the estimated width of the components by the hybrid method, the percentage of correctly counted atomic columns can be predicted in large particles. The predicted percentage of correctly counted atomic columns in

Parameter	Statistics-only based method	Hybrid method
N/G	87	80
σ/δ	0.38	0.49
$-\log L(\mathbf{\Psi}_G)$	-4690	-4670
total number of atoms	125968	128802

Table 5.1: Comparison between the analysis of the Au nanorod from figure 5.1 with the statistics-only based and the hybrid statistics-simulations based atom-counting.

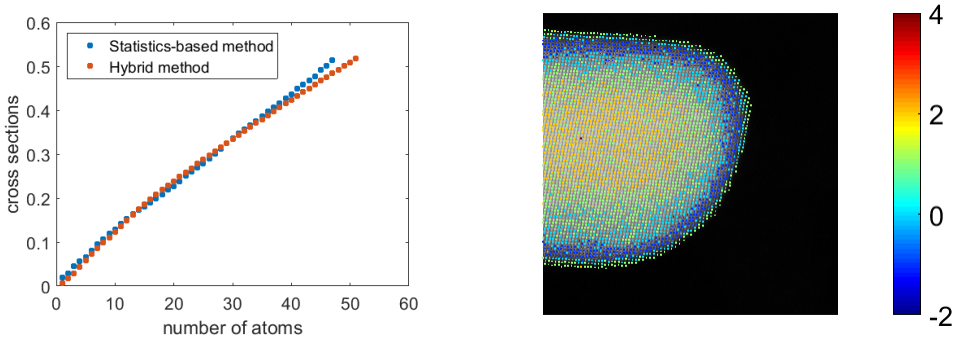

(a) **(b)**

Figure 5.4: Comparison between the statistics-only based and the hybrid statistics-simulations based analysis of the Au nanorod. (a) Intensity/thickness graph calculated using both methods. (b) Difference in atom-counts between the hybrid and the statistics-only based method.

this Au nanorod based on the parameter estimates obtained by the hybrid method, calculated as the theoretical upper bound expressed by equation (4.9), equals 67%.
The difference between the estimated Gaussian mixture models evidently results in a difference between the atom-counts as well. Figure 5.4b displays the difference between the atom-counts obtained by the hybrid method and the statistics-only based method for each atomic column. The total number of atoms counted from the image of the Au nanorod by the hybrid method exceeds the total number of atoms counted by the statistics-only based method by 2834 atoms, an increase of only 2.2%. A different atom-count is found for 77% of the atomic columns, but only 24% of the columns were counted by more than 1 atom difference. Only one column was counted by more than 2 atoms difference, in the middle of this particle, and can be regarded as a statistical outlier. The models estimated using both methods are therefore in good agreement.
Another benefit of the hybrid method, discussed in chapter 3, was the possibility to estimate mixing proportions equal to zero. From this example it becomes clear that this facilitates the interpretation of the atom-counts. The first mixing proportion is estimated equal to zero, implying the absence of atomic columns with only one atom in them. This can now be observed directly through analysis of the mixing proportions.

We conclude that the hybrid method puts atom-counts on an absolute scale. From a mathematical point of view, the estimated mixture model forms a slightly worse fit to the data, but by directly imposing results from image simulations that include channelling theory onto the estimated average cross sections for each thickness, the resulting model is physically more correct. The Au nanorod discussed in this chapter was a well-conditioned example, which explains the good agreement with the statistics-only based method. In the next chapter, we will discuss a more challenging experimental example, which will show the advantage of the hybrid method more clearly.

Chapter 6

Case study: Pt/Ir nanoparticles

Nanoparticles composed of two different metal elements technologically excel their monometallic counterparts. Such bimetallic nanoparticles can have entirely new properties, exceeding the simple combination of properties from both metals. These new properties depend on the precise ratio between the two metals and the structure of the nanoparticle [Toshima and Yonezawa, 1998; Shah et al., 2012; Zaleska-Medynska et al., 2016]. Platinum-based bimetallic nanoparticles in particular can be used as a catalyst for carbon monoxide oxidation in fuel cells [Ralph and Hogarth, 2002]. The platinum-iridium (Pt/Ir) particle which will be analysed in this chapter, was supported on a 3-dimensional carbon black support and received in powder form dusted onto a carbon coated copper grid. Images were taken at the QuAntEM, a double corrected FEI Titan^3 working at 300 kV. The experimental settings that were used are summarised in table 6.1. Images were recorded with different electron doses. Atom-counting was previously impossible from images with a low electron dose [De Backer et al., 2015a]. In order to verify the results obtained by the statistics-only based atom-counting method, image simulations were performed. The difference in atomic number between iridium (Z=77) and platinum (Z=78) is only one, causing a difference of less than 3% up to 15 atoms in a projected atomic column [De Backer et al., 2015a]. Therefore the assumption of a pure platinum particle is reasonable. The treatment of bimetallic particles with a bimetallic library will become possible, thanks to recent progress made in calculating the bimetallic libraries in an efficient manner [van den Bos and Van Aert, 2014; van den Bos et al., 2016].

Parameter	**Value**
Acceleration voltage	300 kV
Convergence angle α	20.2 mrad
Inner angle β_1	35 mrad
Outer angle β_2	190 mrad
Dwell time τ (6.1a)	30 μs
Pixel size dx (6.1a)	0.12 $\mathring{A}$
Electron dose d (6.1a)	$5.2 \cdot 10^5$ $e^-/\mathring{A}^2$
Dwell time τ (6.2a)	15 μs
Pixel size dx (6.2a)	0.24 $\mathring{A}$
Electron dose d (6.2a)	$0.62 \cdot 10^5$ $e^-/\mathring{A}^2$

Table 6.1: Experimental settings used for the high and low dose images of Pt/Ir nanoparticles in figures 6.1a and 6.2a.

The high dose image is shown in figure 6.1a and its refined model in figure 6.1b. An excellent match between the estimated locations and the scattering cross sections obtained from image simulations was achieved using the statistics-only based method [De Backer et al., 2015a], as shown in figure 6.3. As

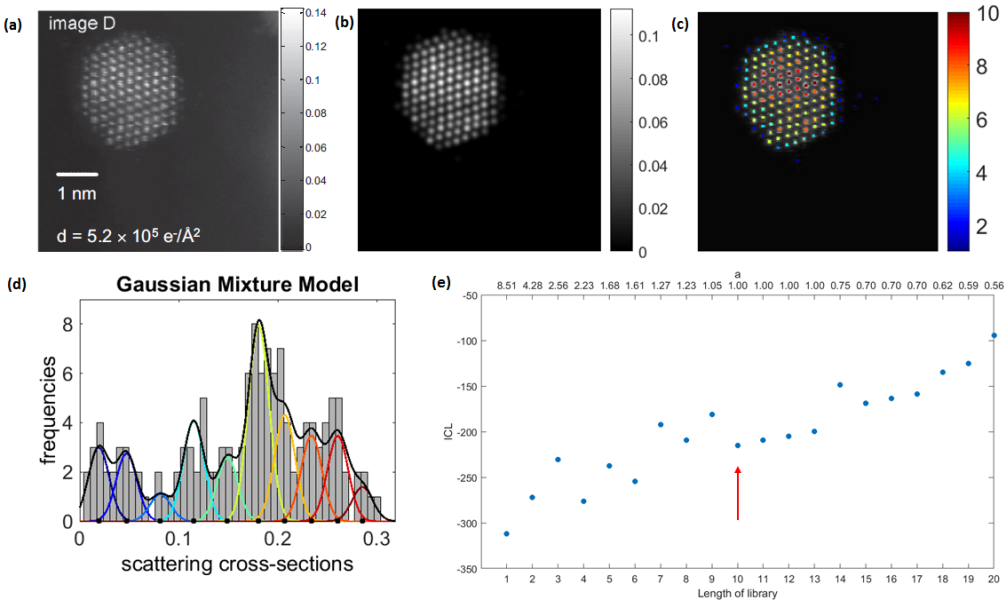

Figure 6.1: (a) Experimental **high dose** image of a Pt/Ir nanoparticle also analysed by De Backer et al. [2015a]. (b) Model of the experimental image. (c) Histogram of scattering cross sections calculated from the model. The full black curve shows the estimated Gaussian mixture model, whereas the coloured curves indicate the separate components. (d) Atom-counts for the Pt/Ir nanoparticle, using the same colour scale as the individual components in the Gaussian mixture model. (e) ICL criterion, with two axes, indicating library length and estimated value of the scaling parameter a.

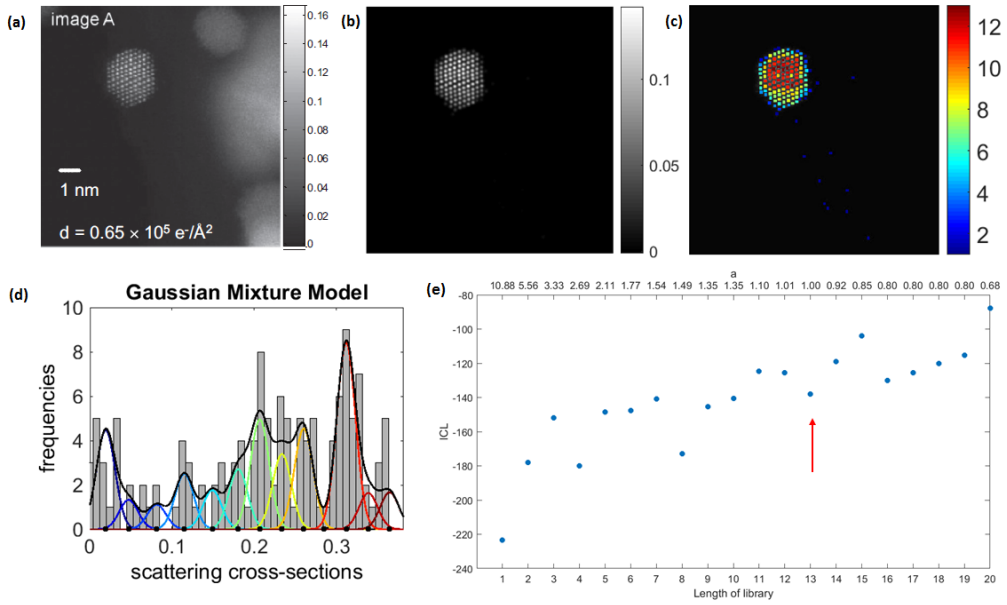

Figure 6.2: (a) Experimental **low dose** image of a Pt/Ir nanoparticle also analysed by De Backer et al. [2015a]. (b) Model of the experimental image. (c) Histogram of scattering cross sections calculated from the model. The full black curve shows the estimated Gaussian mixture model, whereas the coloured curves indicate the separate components. (d) Atom-counts for the Pt/Ir nanoparticle, using the same colour scale as the individual components in the Gaussian mixture model. (e) ICL criterion, with two axes, indicating library length and estimated value of the scaling parameter a.

can be seen from the ICL criterion evaluated as a function of the library length, with a second x-axis indicating the estimated scaling values, the model order chosen by the statistics-only based method by De Backer et al. [2015a] is confirmed by the hybrid method. As indicated by the arrow in figure 6.1e, the minimum of interest is chosen at library length 10, since the estimated scaling value is very close to 1 and this value corresponds to the beginning of a line with slope $\log N$, implying a very high likelihood of the model, as discussed in chapter 3. The estimated Gaussian mixture model is shown as a full black curve overlaying the histogram of scattering cross sections in figure 6.1d. The individual components are shown in colours ranging from blue to red, indicating the corresponding number of atoms per atomic column. The atom-counts for each column of the particle are shown in figure 6.1c, using the same colour scale to indicate the thickness of the columns.

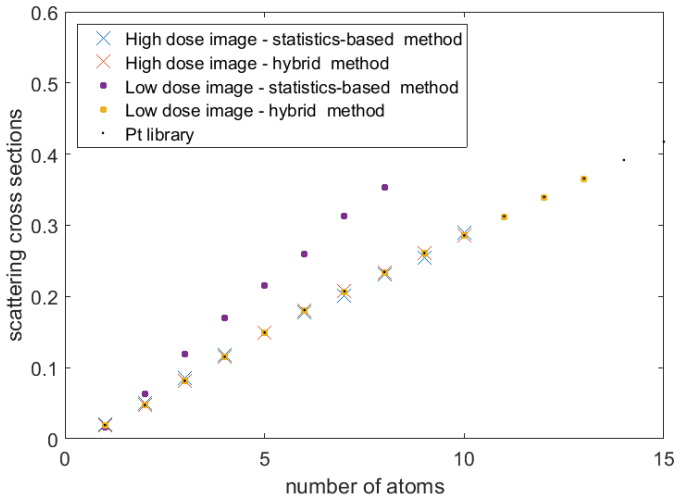

Figure 6.3: Estimated locations for the high dose (6.1) and the low dose (6.2) images obtained with the hybrid and the statistics-only based method are evaluated as a function of the number of atoms in a column. A good agreement is achieved between the results obtained from the high dose image with both the hybrid and the statistics-only based method. However, using the statistics-only based method, estimated locations from the low dose image do not match the simulations, whereas a match can be found using the hybrid method, making atom-counting from the low dose image possible for the first time.

A higher electron dose ensures a higher signal-to-noise ratio in the image, allowing for a more reliable quantitative analysis. However, high electron doses can also cause beam-induced structural changes, specifically in beam-sensitive materials such as small nanoparticles [Meyer et al., 2014]. Reducing the electron dose limits the radiation damage, but also reduces the signal-to-noise ratio, making atom-counting more difficult. The results obtained in chapter 4 suggested that the hybrid method offers the most room for improvement under precisely these circumstances: small particles, imaged with a considerable amount of noise.

The low dose image is shown in figure 6.2a with its refined model in figure 6.2b. Using the statistics-only based method, atoms could not be counted reliably from this image, because the low electron dose results in an underestimation of the model order. A strong deviation between the estimated locations and the simulated scattering cross sections was found by De Backer et al. [2015a], as shown in figure 6.3. Using the hybrid statistics-simulations based atom-counting method, the model order is no longer underestimated. The minimum of interest in the ICL evaluated as a function of the library length, shown in figure 6.2e, occurs at library length 13, corresponding to a scaling parameter close to 1. A good agreement with the simulations is achieved, as can also be seen from figure 6.3. The estimated Gaussian mixture model is shown in figure 6.2d, and the resulting atom-counts for this low dose image are shown in figure 6.2c.

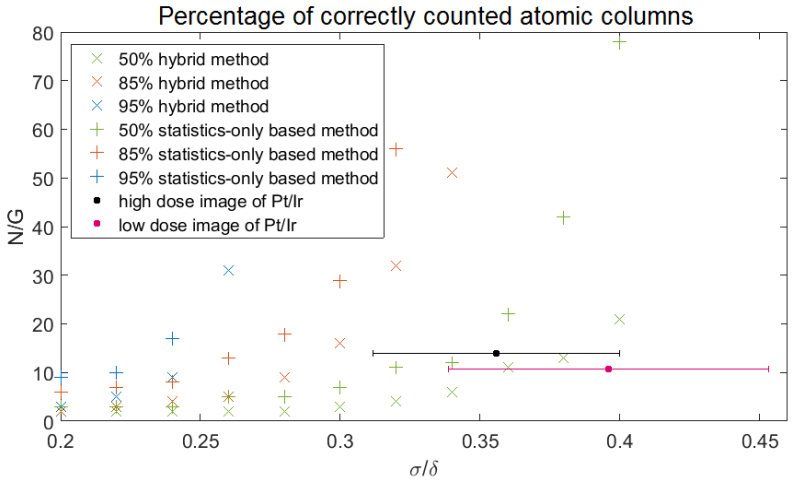

Figure 6.4: The average number of columns per component N/G needed to attain 50%, 85% and 95% correctly counted atomic columns is evaluated as a function of the relative width of the components σ/δ. In black, the conditions of the high dose image from figure 6.1 are indicated together with the uncertainty on the σ/δ value calculated with the Cramér-Rao lower bound. In pink, the conditions of the low dose image, shown in figure 6.2, are indicated, also with the corresponding interval around its σ/δ value.

Until now, the number of atoms per atomic column could not be counted from this low dose image. This can be understood by comparing the conditions for atom-counting, determined by the estimated relative width of the components σ/δ and the average number of atomic columns per component N/G, to the analysis performed in chapter 4. For the high dose image, $\sigma/\delta = 0.3558 \pm 0.0450$ and $N/G = 14$, whereas for the low dose image $\sigma/\delta = 0.3960 \pm 0.0584$ and $N/G = 10.77$. The uncertainty on the estimated relative width was calculated using the Cramér-Rao lower bounds (equation (4.1)) on the variance of the estimated width and scaling value:

$$s_{\sigma/\delta} = \sqrt{\left(\frac{\partial \sigma/\delta}{\partial \sigma}\right)^2 \mathrm{CRLB}_\sigma + \left(\frac{\partial \sigma/\delta}{\partial a}\right)^2 \mathrm{CRLB}_a}, \tag{6.1}$$

$$= \sqrt{\left(\frac{1}{\delta}\right)^2 \mathrm{CRLB}_\sigma + \left(-\frac{\sigma}{\delta a}\right)^2 \mathrm{CRLB}_a}. \tag{6.2}$$

The σ/δ and N/G values for the high and low dose images are indicated in black and pink respectively in figure 6.4, together with the percentages of correctly counted atomic columns for different conditions, as obtained in chapter 4. From figure 6.4, it is clear that the advantage of the hybrid method is more significant for the low dose image than for the high dose image. In case of this low electron dose, an N/G value of 80 is needed in order to reach 50% correctly counted atomic columns using the statistics-only based method, whereas the required N/G value to reach this percentage using the hybrid method only equals 20. This explains why atoms could not be counted from the low dose image before, whereas this has now become possible for the first time, by using the hybrid method.

In conclusion, we have shown that the hybrid method enables us to count the number of atoms per column in an experimental image from which counting was previously impossible, due to the low electron dose. The hybrid method for atom-counting therefore holds great promise for quantitative analysis of challenging, beam-sensitive nanoparticles, thanks to its ability to overcome challenges presented due to low electron doses.

Chapter 7

Conclusion

A novel method for atom-counting was introduced. This so-called hybrid statistics-simulations based method for atom-counting from ADF STEM images of monatomic crystalline nanostructures directly combines the principles of the two existing methods for atom-counting, based on image simulations on the one hand and on statistical parameter estimation theory on the other hand. The key to the direct combination of both approaches is to use the information obtained from image simulations as a prior knowledge that can be incorporated into the statistical parameter estimation theory framework. In the statistics-only based method, the probability distribution of the estimated scattering cross sections, i.e. the total intensity of scattered electrons per atomic column, is described by a Gaussian mixture model. The estimated locations of these Gaussian components correspond to the scattering cross sections of atomic columns with different thicknesses. Image simulations allow one to determine the scattering cross sections for each different thickness. Using this knowledge, the estimated locations in the Gaussian mixture model are no longer free parameters, but are determined by the simulated scattering cross sections. However, small calibration errors have an effect on the scattering cross sections which can not be neglected. Previously, in the simulations-only based method, such systematic errors would remain undetected, causing the accuracy of the obtained atom-counts to depend solely on the unknown accuracy of the image simulations. This disadvantage can be overcome by proposing a relationship between scattering cross sections calculated from experimental images and from simulated images that describes the deviation of the scattering cross sections caused by common calibration errors. The scattering cross sections resulting from image simulations using different annular dark field detector inner angles were compared, as well as the scattering cross sections obtained from image simulations with different amounts of sample tilt. Both effects can to a good approximation be described by a linear scaling relationship. Therefore, the imposed relationship to relate the estimated locations in the Gaussian mixture model to the prior knowledge obtained from image simulations used in the description of the hybrid method is a linear scaling. This scaling relationship, together with the prior knowledge resulting from image simulations, was incorporated in the statistical parameter estimation theory framework to obtain a new algorithm for atom-counting.

The implementation and interpretation of this hybrid method was studied by evaluating the negative log likelihood. However, it was clear that this negative log likelihood evaluated as a function of the scaling parameter exhibits many local minima. Due to the analytical implementation of the parameter updates, the parameters evolve towards the nearest local minimum in the negative log likelihood. This means that many starting values are needed in order for the correct model to be estimated. The local minima occur at the true scaling value, and at fractions of this value determined by the more components used in the estimated mixture model. Mixing proportions can be estimated equal to zero. Therefore, at the true scaling value, the correct model can be obtained by estimating all mixing proportions of components corresponding to atomic columns with a higher number of atoms equal to zero. The values of the estimated scaling parameters at the most apparent local minima can aid the

interpretation and lead to the correct choice of scaling value in well-conditioned academic examples. However, this interpretation becomes more challenging when more complex experimental examples are considered, and a mathematically better fit will always be obtained when more components can be used. The negative log likelihood evaluated as a function of the library length keeps decreasing with increasing library length. We conclude that an order selection criterion, evaluated as a function of the library length, is needed to select the correct Gaussian mixture model. The Integrated Classification Likelihood (ICL) criterion, used successfully in the statistics-only based method, is introduced, and is shown successful for model order selection in the hybrid method as well. The ICL criterion evaluated as a function of the library length is studied, and three guidelines for its interpretation are constructed: the minimum of interest is a local minimum, it corresponds to an estimated scaling parameter close to the expected scaling value of 1, and when lines with slope $\log N$ occur, the minimum of interest is chosen at the beginning of such a line. The latter lines correspond to effectively the same models with the same scaling value, indicating the likelihood of the model. Adding components with zero mixing proportions is here preferred over changing the scaling value and changing the model by using more components.

Next, the performance of the newly introduced hybrid method for atom-counting was examined. Simulations lead to the conclusion that the parameters of the Gaussian mixture model with locations restricted to the scaled library values are estimated accurately. Whereas the statistics-only based method tends to underestimate the width of the components when the actual width is large, the hybrid method is able to estimate the width of the components more accurately, even for sets of scattering cross sections with few observations per component. One of the great advantages of working in a statistical parameter estimation theory framework is that an analytical expression for the precision can be determined. The Cramér-Rao lower bound expresses the lower bound on the variance of unbiased estimators, and is attained by the parameter estimates obtained by the hybrid method. Since the estimate of the width of the components obtained with the hybrid method is accurate, we now have a way of reliably predicting the precision of the estimated parameters of the Gaussian mixture models, using the Cramér-Rao lower bound.

The performance of the hybrid method for atom-counting is examined and compared to the statistics-only based method. The percentage of correctly selected minima from the ICL criterion evaluated as a function of library length and the percentage of correctly counted atomic columns was calculated for different values of the average number of columns per component N/G and the relative width of the components of the Gaussian mixture model σ/δ. The required number of columns per component N/G to reach a given percentage is smaller for the hybrid method, as compared to the statistics-only based method at a given relative width of the components σ/δ. This effect becomes even more pronounced at high σ/δ values. In practice, these conditions correspond to small nanoparticles imaged with a low electron dose, which causes a low signal-to-noise ratio in the experimental image.

A theoretical upper bound of the percentage of correctly counted atomic columns can be calculated, based on the overlap between the Gaussian components. For small values of σ/δ, the upper bound is easily achieved, contrary to the results at high values of σ/δ. Large overlap between the components makes it harder to estimate the correct model. This effect is most significant for the statistics-only based method. The hybrid method is shown to be able to stay closer to the upper bound under challenging conditions for atom-counting.

To conclude this master's thesis, two case studies of experimental images were performed. A gold nanorod, for which an analysis was already successfully conducted by Van Aert et al. [2013] using the statistics-only based method, was analysed using the hybrid method. A high number of columns of the gold nanorod were imaged, making it easier to count atoms from this experimental image, and a good agreement between the results obtained with both methods was found. The small difference between

the results obtained with the statistics-only based method and the hybrid statistics-simulations based method can be explained by the restriction imposed on the estimated locations obtained by the hybrid method. Using the statistics-only based method, freely estimated locations can be shifted to result in a mathematically slightly better fit, but a physically less accurately estimated Gaussian mixture model.
Finally, more challenging experimental images were analysed. Images were recorded of small platinum-iridium nanoparticles using different electron doses. Atoms have already been counted from the high dose image by De Backer et al. [2015a], but could not be counted from the low dose image when using the statistics-only based method. The low electron dose resulted in an underestimation of the number of components in the mixture model, causing the estimated locations to differ strongly from the image simulations. Detailed research already showed that the underestimation of the number of components was a direct consequence of the low electron dose. Using the hybrid method, atom-counts were obtained in nice agreement with the image simulations, despite the low electron dose. It is shown that the hybrid method enables us to count atoms in challenging low dose images from which atom-counting was impossible up until now.

To summarise, in this thesis we presented a new method for atom-counting from ADF STEM images of monatomic crystalline nanostructures that allows one to exceed the limitations of the atom-counting methods that exist today. It was shown that this method holds great promise for counting the number of atoms in beam-sensitive materials. Such materials need to be imaged using a low electron dose in order to avoid radiation damage, which makes the images more noisy and more difficult to analyse. The hybrid method developed in this master's thesis enables atom-counting under more challenging conditions and therefore takes an important step towards the reliable analysis of this kind of nanomaterials.

Future work to further improve this method will include increasing its speed and exploring the route towards automatic selection of the model order. Furthermore, the results obtained about the performance for atom-counting in this thesis are based on the assumption that the linear scaling relationship between simulated scattering cross sections and experimental scattering cross sections accurately describes the combined effect of all calibration errors. However, not all parameters used to perform the image simulations affect the scattering cross sections in a purely linear way. Another possible improvement needed for this hybrid method for atom-counting is therefore the refinement of this relationship. Ultimately, it is expected that the analysis of bimetallic particles using a bimetallic library will become possible by extending the hybrid method. Another interesting extension worthy of further research would be to directly combine information obtained from ADF STEM images with results from electron energy loss spectroscopy (EELS) or energy dispersive X-ray (EDX) spectroscopy.

Bibliography

Allen, L., Findlay, S., Oxley, M., and Rossouw, C. (2003). Lattice-resolution contrast from a focused coherent electron probe. Part I. *Ultramicroscopy*, 96:47–63.

Anderson, S., Birkeland, C., Anstis, G., and Cockayne, D. (1997). An approach to quantitative compositional profiling at near-atomic resolution using high-angle annular dark field imaging. *Ultramicroscopy*, 69:83–103.

Bals, S., Van Aert, S., Romero, C., Lauwaet, K., Van Bael, M., Schoeters, B., Partoens, B., Yücelen, E., Lievens, P., and Van Tendeloo, G. (2012). Atomic scale dynamics of ultrasmall germanium clusters. *Nature Communications*, 3:897.

Biernacki, C., Celeux, G., and Govaert, G. (2000). Assessing a mixture model for clustering with the integrated classification likelihood. *IEEE Transactions on Pattern Analysis and Machine Intelligence*, 22:719–725.

Bollig, B., Fischer, H., and Kubalek, E. (1996). Multislice simulation of high-resolution scanning transmission electron microscopy Z-contrast images of semiconductor heterointerfaces. *Scanning*, 18:291–300.

Boschker, H., Huijben, M., Vailionis, A., Verbeeck, J., Van Aert, S., Luysberg, M., Bals, S., Van Tendeloo, G., Houwman, E., Koster, G., Blank, D., and Rijnders, G. (2011). Optimized fabrication of high-quality $La_{0.67}Sr_{0.33}MnO_3$ thin films considering all essential characteristics. *Journal of Physics D: Applied Physics*, 44:205001.

Cowley, J., Hansen, M., and Wang, S. (1995). Imaging modes with an annular detector in STEM. *Ultramicroscopy*, 58:18–24.

Cowley, J. and Moodie, A. (1959). The scattering of electrons by atoms and crystals. III. Single-crystal diffraction patterns. *Acta Crystallographica*, 12:360–367.

Croitoru, M., Van Dyck, D., Van Aert, S., Bals, S., and Verbeeck, J. (2006). An efficient way of including thermal diffuse scattering in simulation of scanning transmission electron microscopic images. *Ultramicroscopy*, 106:933–940.

De Backer, A., Martinez, G., MacArthur, K., Jones, L., Béché, A., Nellist, P., and Van Aert, S. (2015a). Dose limited reliability of quantitative annular dark field scanning transmission electron microscopy for nano-particle atom-counting. *Ultramicroscopy*, 151:56–61.

De Backer, A., De wael, A., Gonnissen, J., and Van Aert, S. (2015b). Optimal experimental design for nano-particle atom-counting from high-resolution STEM images. *Ultramicroscopy*, 151:46–55.

De Backer, A., Martinez, G., Rosenauer, A., and Van Aert, S. (2013). Atom counting in HAADF STEM using a statistical model-based approach: Methodology, possibilities, and inherent limitations. *Ultramicroscopy*, 134:23–33.

Dempster, A., Laird, N., and Rubin, D. (1977). Maximum Likelihood from Incomplete Data via the EM Algorithm. *Journal of the Royal Statistical Society. Series B (Methodological)*, 39:1–38.

den Dekker, A., Van Aert, S., van den Bos, A., and Van Dyck, D. (2005). Maximum likelihood estimation of structure parameters from high resolution electron microscopy images. Part I: a theoretical framework. *Ultramicroscopy*, 104:83106.

E, H., MacArthur, K., Pennycook, T., Okunishi, E., D'Alfonso, A., Lugg, N., Allen, L., and Nellist, P. (2013). Probe integrated scattering cross sections in the analysis of atomic resolution HAADF STEM images. *Ultramicroscopy*, 133:109119.

Erni, R., Rossell, M., Kisielowski, C., and Dahmen, U. (2009). Atomic-Resolution Imaging with a Sub-50-pm Electron Probe. *Physical Review Letters*, 102:096101.

Fertig, J. and Rose, H. (1981). Resolution and contrast of crystalline objects in high-resolution scanning-transmission electron-microscopy. *Optik*, 59:407–429.

Findlay, S., Allen, L., Oxley, M., and Rossouw, C. (2003). Lattice-resolution contrast from a focused coherent electron probe. Part II. *Ultramicroscopy*, 96:65–81.

Findlay, S. and LeBeau, J. (2013). Detector non-uniformity in scanning transmission electron microscopy. *Ultramicroscopy*, 124:52–60.

Fujita, H. and Sumida, N. (1994). *Physics of New Materials - Chapter 8 Usefulness of Electron Microscopy*. New York: Springer Science+Business Media LLC.

Geuens, P. and Van Dyck, D. (2005). The S-State Model for Electron Channeling in High-Resolution Electron Microscopy. *Advances in Imaging and Electron Physics*, 136:111–226.

Grieb, T., Müller, K., Fritz, R., Schowalter, M., Neugebohrn, N., Knaub, N., Volz, K., and Rosenauer, A. (2012). Determination of the chemical composition of GaNAs using STEM HAADF imaging and STEM strain state analysis. *Ultramicroscopy*, 117:15–23.

Grillo, V. (2011). An advanced study of the response of ADF detector. *Journal of Physics: Conference Series*, 326:012036.

Haider, M., Uhlemann, S., Schwan, E., Rose, H., Kabius, B., and Urban, K. (1998). Electron microscopy image enhanced. *Nature*, 392:768–769.

Hawkes, P., Spence, J., and Nellist, P. (2007). *Science of Microscopy - Chapter 2 Scanning Transmission Electron Microscopy*. New York: Springer Science+Business Media LLC.

Henderson, R. (1995). The potential and limitations of neutrons, electrons and X-rays for atomic resolution microscopy of unstained biological molecules. *Q Rev Biophys*, 28:171–193.

Huang, T. and Nancy Xu, X. (2010). Synthesis and Characterization of Tunable Rainbow Colored Colloidal Silver Nanoparticles Using Single-Nanoparticle Plasmonic Microscopy and Spectroscopy. *Journal of Materials Chemistry*, 20:9867–9876.

Huijben, M., Koster, G., Kruize, M., Wenderich, S., Verbeeck, J., Bals, S., Slooten, E., Shi, B., Molegraaf, H., Kleibeuker, J., Van Aert, S., Goedkoop, J., Brinkman, A., Blank, D., Golden, M., Van Tendeloo, G., Hilgenkamp, H., and Rijnders, G. (2013). Defect Engineering in Oxide Heterostructures by Enhanced Oxygen Surface Exchange. *Advanced Functional Materials*, 24:5240.

Ishizuka, K. (2002). A practical approach for STEM image simulation based on the FFT multislice method. *Ultramicroscopy*, 90:71–83.

Jones, L. (2016). Quantitative ADF STEM: acquisition, analysis and interpretation. *IOP Conf. Series: Materials Science and Engineering*, 109:012008.

Jones, L., MacArthur, K., Fauske, V., van Helvoort, A., and Nellist, P. (2014). Rapid estimation of catalyst nanoparticle morphology and atomic-coordination by high-resolution Z-contrast electron microscopy. *Nano Letters*, 14:6336–6341.

Jones, L. and Nellist, P. (2013). Identifying and Correcting Scan Noise and Drift in the Scanning Transmission Electron Microscope. *Microscopy and Microanalysis*, 19:1050–1060.

Jones, L., Yang, H., Pennycook, T., Marshall, M., Van Aert, S., Browning, N., Castell, M., and Nellist, P. (2015). Smart Aligna new tool for robust non-rigid registration of scanning microscope data. *Advanced Structural and Chemical Imaging*, 1:8.

Kirkland, E. (1998). *Advanced computing in electron microscopy.* New York: Springer Science+Business Media LLC.

Koch, C. (2002). *Determination of core structure periodicity and point defect density along dislocations.* Tempe, AZ: Arizona State University.

Koli, D., Agnihotri, G., and Purohit, R. (2014). A Review on Properties, Behaviour and Processing Methods for Al- Nano Al_2O_3 Composites. *Procedia Materials Science, 3rd International Conference on Materials Processing and Characterisation (ICMPC 2014)*, 6:567589.

LeBeau, J., Findlay, S., Allen, L., and Stemmer, S. (2008). Quantitative Atomic Resolution Scanning Transmission Electron Microscopy. *Physical Review Letters*, 100:206101.

LeBeau, J., Findlay, S., Allen, L., and Stemmer, S. (2010). Standardless atom counting in scanning transmission electron microscopy. *Nanoletters*, 10:4405–4408.

Lin, W., Insley, T., Tuttle, M., Zhu, L., Berthold, D., Král, P., Rienstra, C., and Murphy, C. (2015). Control of Protein Orientation on Gold Nanoparticles. *The Journal of Physical Chemistry C*, 119:2103521043.

Loane, R., Xu, P., and Silcox, J. (1991). Thermal vibrations in convergent-beam electron diffraction. *Acta Crystallographica Section A*, 47:267–278.

MacArthur, K., DAlfonso, A., Ozkaya, D., Allen, L., and Nellist, P. (2015). Optimal ADF STEM imaging parameters for tilt-robust image quantification. *Ultramicroscopy*, 156:1–8.

MacArthur, K., Jones, L., and Nellist, P. (2014). How flat is your detector? Non-uniform annular detector sensitivity in STEM quantification. *Journal of Physics: Conference Series*, 522:012018.

Martinez, G. (2014). *Quantitative Model-based High Angle Annular Dark Field Scanning Transmission Electron Microscopy.* PhD thesis, University of Antwerp.

Martinez, G., De Backer, A., Rosenauer, A., Verbeeck, J., and Van Aert, S. (2013). The effect of probe inaccuracies on the quantitative model-based analysis of high angle annular dark field scanning transmission electron microscopy images. *Micron*, 63:57–63.

Martinez, G., Jones, L., De Backer, A., Béché, A., Verbeeck, J., Van Aert, S., and Nellist, P. (2015). Quantitative STEM normalisation: The importance of the electron flux. *Ultramicroscopy*, 159:46–58.

McLachlan, G. and Peel, D. (2000). *Finite Mixture Models.* Wiley series in probability and statistics. John Wiley and Sons, inc.

Mehrtens, T., Schowalter, M., Tytko, D., Choi, P., Raabe, D., Hoffmann, L., Jönen, H., Rossow, U., Hangleiter, A., and Rosenauer, A. (2013). Measurement of the indium concentration in high indium content InGaN layers by scanning transmission electron microscopy and atom probe tomography. *Applied Physics Letters*, 102:132112.

Meyer, J., Kotakoski, J., and Mangler, C. (2014). Atomic structure from large-area, low-dose exposures of materials: A new route to circumvent radiation damage. *Ultramicroscopy*, 145:13–21.

Mikami, Y., Dhakshinamoorthy, A., Alvaro, M., and García, H. (2013). Catalytic activity of unsupported gold nanoparticles. *Catalysis Science & Technology*, 3:58–69.

Moore, G. (1998). Cramming More Components onto Integrated Circuits. *Proceedings of the IEEE*, 86:82–85.

Muller, D., Edwards, B., Kirkland, E., and Silcox, J. (2001). Simulation of thermal diffuse scattering including a detailed phonon dispersion curve. *Ultramicroscopy*, 86:371–380.

Nellist, P. and Pennycook, S. (1999). Incoherent imaging using dynamically scattered coherent electrons. *Ultramicroscopy*, 78:111–124.

Nellist, P. and Pennycook, S. (2000). The Principles and Interpretation of Annular Dark-Field Z-Contrast Imaging. *Advances in imaging and electron physics*, 113:147.

Nguyen, D., Findlay, S., and Etheridge, J. (2014). The spatial coherence function in scanning transmission electron microscopy and spectroscopy. *Ultramicroscopy*, 146:6–16.

Olson, G. (2000). Pathways of Discovery, Designing a New Material World. *Science*, 288:993–998.

Ralph, T. and Hogarth, M. (2002). Catalysis for Low Temperature Fuel Cells. *Platinum Metals Review*, 46:117–135.

Rosenauer, A., Mehrtens, T., Müller, K., Gries, K., Schowalter, M., Satyam, P., Bley, S., Tessarek, C., Hommel, D., Sebald, K., Seyfried, M., Gutowski, J., Avramescu, A., Engl, K., and Lutgen, S. (2011). Composition mapping in InGaN by scanning transmission electron microscopy. *Ultramicroscopy*, 111:1316–1327.

Rosenauer, A. and Schowalter, M. (2007). STEMSIM - A new software tool for simulation of STEM HAADF Z-contrast imaging. *Springer Proceedings in Physics*, 120:169.

Rosenauer, A., Schowalter, M., Titantah, J., and Lamoen, D. (2008). An emission-potential multislice approximation to simulate thermal diffuse scattering in high-resolution transmission electron microscopy. *Ultramicroscopy*, 108:1504–1513.

Ruskin, R., Yu, Z., and Grigorieff, N. (2013). Quantitative characterization of electron detectors for transmission electron microscopy. *Journal of Structural Biology*, 184:385393.

Shah, A., Rahman, L., Qureshi, R., and Rehman, Z. (2012). Synthesis, characterization and applications of bimetallic (Au-Ag, Au-Pt, Au-Ru) alloy nanoparticles. *Reviews on Advanced Materials Science*, 30:133–149.

Shibata, N., Kohno, Y., Findlay, S., Sawada, H., Kondo, Y., and Ikuhara, Y. (2010). New area detector for atomic-resolution scanning transmission electron microscopy. *Journal of Electron Microscopy*, 59:473–479.

Spence, J. (1999). The future of atomic resolution electron microscopy for materials science. *Materials Science and Engineering: R: Reports*, 26:1–49.

Stone, J., Jackson, S., and Wright, D. (2011). Biological applications of gold nanorods. *Wiley Interdiscip Rev Nanomed Nanobiotechnol.*, 3:100–109.

Takayanagi, K., Kim, S., Lee, S., Oshima, Y., Tanaka, T., Tanishiro, Y., Sawada, H., Hosokawa, F., Tomita, T., Kaneyama, T., and Kondo, Y. (2011). Electron microscopy at a sub-50 pm resolution. *Journal of Electron Microscopy*, 60:239–244.

Toshima, N. and Yonezawa, T. (1998). Bimetallic nanoparticlesnovel materials for chemical and physical applications. *New Journal of Chemistry*, 22:1179–1201.

Van Aert, S., Batenburg, K., Rossell, M., Erni, R., and Van Tendeloo, G. (2011). Three-dimensional atomic imaging of crystalline nanoparticles. *Nature*, 470:374–377.

Van Aert, S., De Backer, A., Martinez, G., Goris, B., Bals, S., and Van Tendeloo, G. (2013). Procedure to count atoms with trustworthy single-atom sensitivity. *Physical Review B*, 87:064107.

Van Aert, S., den Dekker, A., van den Bos, A., and Van Dyck, D. (2005). Maximum likelihood estimation of structure parameters from high resolution electron microscopy images. Part II: a practical example. *Ultramicroscopy*, 104:107125.

Van Aert, S., Turner, S., Delville, R., Schryvers, D., Van Tendeloo, G., and Salje, E. (2012). Direct Observation of Ferrielectricity at Ferroelastic Domain Boundaries in CaTiO3 by Electron Microscopy. *Advanced materials*, 24:523.

Van Aert, S., Verbeeck, J., Erni, R., Bals, S., Luysberg, M., Van Dyck, D., and Van Tendeloo, G. (2009). Quantitative atomic resolution mapping using high-angle annular dark field scanning transmission electron microscopy. *Ultramicroscopy*, 109:12361244.

van den Bos, K., De Backer, A., Martinez, G., Winckelmans, N., Bals, S., Nellist, P., and Van Aert, S. (2016). Unscrambling mixed elements using high angle annular dark field scanning transmission electron microscopy. *Physical Review Letters, accepted*.

van den Bos, K. and Van Aert, S. (2014). A channelling based approach for scattering cross sections of mixed columns in HAADF STEM images. *18th International Microscopy Congress IMC 2014, Prague, Czech Republic*, pages IT–2–P–2255.

Van Dyck, D., Van Aert, S., den Dekker, A., and van den Bos, A. (2003). Is atomic resolution transmission electron microscopy able to resolve and refine amorphous structures? *Ultramicroscopy*, 98:27–42.

Vigderman, L., Khanal, B., and Zubarev, E. (2012). Functional Gold Nanorods: Synthesis, Self-Assembly, and Sensing Applications. *Advanced Materials*, 24:48114841.

Wiesendanger, R. (1994). *Scanning Probe Microscopy and Spectroscopy, Methods and Applications*. Cambridge: Cambridge University Press.

Yang, H., Pennycook, T., and Nellist, P. (2015). Efficient phase contrast imaging in STEM using a pixelated detector. Part II: Optimisation of imaging conditions. *Ultramicroscopy*, 151:232239.

Yang, P. and Tarascon, J. (2012). Towards systems materials engineering. *Nature Materials*, 11:560–563.

Zaleska-Medynska, A., Marchelek, M., Diak, M., and Grabowska, E. (2016). Noble metal-based bimetallic nanoparticles: the effect of the structure on the optical, catalytic and photocatalytic properties. *Advances in Colloid and Interface Science*, 229:80–107.

Zanchet, D., Hall, B., and Ugarte, D. (2000). *Characterization of Nanophase Materials - Chapter 2 X-ray Characterization of Nanoparticles*. Weinheim: Wiley-VCH.

List of publications

Publications in journals included in the ISI Web of Science

- A. De Backer, A. De wael, J. Gonnissen, G. T. Martinez, A. Béché, K. E. MacArthur, L. Jones, P. D. Nellist, S. Van Aert, Quantitative annular dark field scanning transmission electron microscopy for nanoparticle atom-counting: What are the limits?, Microscopy and Analysis 21 (2015) 8-12.

- A. De Backer, A. De wael, J. Gonnissen, G. T. Martinez, A. Béché, K. E. MacArthur, L. Jones, P. D. Nellist, S. Van Aert, Quantitative annular dark field scanning transmission electron microscopy for nanoparticle atom-counting: What are the limits?, Journal of Physics: Conference Series 644 (2015) 012034.

- A. De Backer, A. De wael, J. Gonnissen, S. Van Aert, Optimal experimental design for nanoparticle atom-counting from high-resolution STEM images, Ultramicroscopy 151 (2015) 46-55.

- A. De wael, A. De Backer, L. Jones, P.D. Nellist, S. Van Aert, Hybrid statistics-simulations based method for atom-counting using scanning transmission electron microscopy, manuscript in preparation for Ultramicroscopy (2016)

Publications in other journals

- A. De wael, Minimum electron budget for a maximum result: how to count atoms with single atom sensitivity using electron microscopy?, Student Research Conference (2014) 123-126.

Conference abstracts

- S. Van Aert, A. De wael, K. van den Bos, J. Gonnissen, A. De Backer, L. Jones, M. Alania, G. T. Martinez, P. D. Nellist, Minimum electron budget for maximum structural information of beam-sensitive nanoparticles using quantitative scanning transmission electron microscopy, MRS 2016, Phoenix, USA, March 28 - April 1, 2016, 2408003.

- S. Van Aert, A. De wael, K. van den Bos, J. Gonnissen, A. De Backer, L. Jones, M. Alania, G. T. Martinez, P. D. Nellist, Minimum electron budget for maximum structural information of beam-sensitive nanoparticles using quantitative scanning transmission electron microscopy, ACMM 2016, Melbourne, Australia, January 31 - February 4, 2016, 69.

- A. De Backer, A. De wael, J. Gonnissen, G. T. Martinez, A. Béché, K. E. MacArthur, L. Jones, P. D. Nellist, S. Van Aert, Quantitative annular dark field scanning transmission electron microscopy for nanoparticle atom-counting: What are the limits?, MMC 2015 incorporating EMAG 2015, Manchester, UK, June 29 - July 2, 2015, 4033.

- S. Van Aert, A. De Backer, A. De wael, J. Gonnissen, G. Martinez, A. Bch, K. MacArthur, L. Jones, P.D. Nellist, Quantitative annular dark field scanning transmission electron microscopy for nanoparticle atom-counting: What are the limits?, PICO 2015 - 3rd Conference on Frontiers of Aberration Corrected Electron Microscopy, Kasteel Vaalsbroek, The Netherlands, April 19-23, 2015.

- A. De Backer, A. De wael, S. Van Aert, Probability of error for counting the number of atoms from high resolution HAADF STEM images, 18th International Microscopy Congress IMC 2014, Prague, Czech Republic, September 7-12, 2014, IT-2-P-2255.

Appendix A

Expectation-Maximisation algorithm

In general, a Gaussian mixture model is expressed by equation (A.1).

$$\begin{aligned} f_{\text{mix}}\left(\hat{V}_n; \mathbf{\Psi}_G\right) &= \sum_{g=1}^{G} \pi_g \phi_g \left(\hat{V}_n; \mu_g, \sigma\right) \\ &= \sum_{g=1}^{G} \pi_g \frac{1}{\sqrt{2\pi\sigma^2}} \exp\left(-\frac{(\hat{V}_n - \mu_g)^2}{2\sigma^2}\right), \end{aligned} \tag{A.1}$$

with G the number of components, π_g the mixing proportions, μ_g the locations and σ the width of the components. $\hat{V}_n$ represents the least squares estimate for the n^{th} scattering cross section, estimated equal to the volume under the n^{th} Gaussian peak. The vector $\mathbf{\Psi}_G$ is the parameter vector containing all unknown parameters to be estimated $\mathbf{\Psi}_G = (\pi_1, ..., \pi_{G-1}, \mu_1, ..., \mu_G, \sigma)^T$.
We start by deriving update formulas for the estimation of the parameters of the Gaussian mixture model in the purely statistics-only based atom-counting method. Afterwards, the substitution $\mu_g = a\mathcal{M}_g$ is introduced in order to derive the parameter updates of the Gaussian mixture model incorporating the library values expressed by equation (A.2).

$$\begin{aligned} f_{\text{mix}}\left(\hat{V}_n; \mathbf{\Psi}_G\right) &= \sum_{g=1}^{G} \pi_g \phi_g \left(\hat{V}_n; a, \sigma\right) \\ &= \sum_{g=1}^{G} \pi_g \frac{1}{\sqrt{2\pi\sigma^2}} \exp\left(-\frac{(\hat{V}_n - a\mathcal{M}_g)^2}{2\sigma^2}\right), \end{aligned} \tag{A.2}$$

with G the library length, with a the scaling parameter and $\mathcal{M}_g$ the library values. The parameter vector $\mathbf{\Psi}_G$ is in this case expressed as $\mathbf{\Psi}_G = (\pi_1, ..., \pi_{G-1}, a, \sigma)^T$.
Parameters are estimated using the Expectation-Maximisation Algorithm, for a constant number of components G, which calculates iterative updates that maximise the likelihood. Each iteration of the algorithm consists of two steps, the E-step and the M-step. In the E-step, the probability that a volume $\hat{V}_n$ belongs to the g^{th} component is calculated:

$$\tau_g\left(\hat{V}_n; \mathbf{\Psi}_G^{(k)}\right) = \frac{\pi_g^{(k)} \phi_g\left(\hat{V}_n; \mu_g^{(k)}, \sigma^{(k)}\right)}{\sum_{h=1}^{G} \pi_h^{(k)} \phi_h\left(\hat{V}_n; \mu_h^{(k)}, \sigma^{(k)}\right)}, \tag{A.3}$$

with k the index of the iteration. The update of the parameters is calculated in the M-step in order to maximise the log likelihood. The updates for the maximum likelihood estimates of π_g, μ_g and σ are expressed by equation (A.4), (A.5) and (A.6).

$$\pi_g^{(k+1)} = \frac{1}{N}\sum_{n=1}^{N}\tau_g\left(\hat{V}_n;\boldsymbol{\Psi}_G^{(k)}\right), \tag{A.4}$$

$$\mu_g^{(k+1)} = \frac{\sum_{n=1}^{N}\tau_g\left(\hat{V}_n;\boldsymbol{\Psi}_G^{(k)}\right)\hat{V}_n}{\sum_{n=1}^{N}\tau_g\left(\hat{V}_n;\boldsymbol{\Psi}_G^{(k)}\right)}, \tag{A.5}$$

and

$$\sigma^{(k+1)} = \sqrt{\frac{1}{N}\sum_{g=1}^{G}\sum_{n=1}^{N}\tau_g\left(\hat{V}_n;\boldsymbol{\Psi}_G^{(k)}\right)\left(\hat{V}_n-\mu_g^{(k+1)}\right)^2}. \tag{A.6}$$

This iterative algorithm stops when convergence of the log likelihood is reached.
Updates are calculated in the M-step in order to maximise the likelihood function, or equivalently, maximise the log likelihood function, as derived in equation (A.7).

$$\begin{aligned}
\frac{\partial \log L\left(\boldsymbol{\Psi}_G\right)}{\partial \boldsymbol{\Psi}_G} &= \sum_{n=1}^{N}\frac{\partial}{\partial \boldsymbol{\Psi}_G}\left[\log\left(\sum_{g=1}^{G}\pi_g\phi_g\left(\hat{V}_n;\mu_g,\sigma\right)\right)\right] \\
&= \sum_{n=1}^{N}\frac{1}{\sum_{g=1}^{G}\pi_g\phi_g\left(\hat{V}_n;\mu_g,\sigma\right)}\frac{\partial}{\partial \boldsymbol{\Psi}_G}\left[\sum_{h=1}^{G}\pi_h\phi_h\left(\hat{V}_n;\mu_h,\sigma\right)\right] \\
&= \sum_{n=1}^{N}\sum_{h=1}^{G}\frac{1}{\sum_{g=1}^{G}\pi_g\phi_g\left(\hat{V}_n;\mu_g,\sigma\right)}\frac{\pi_h\phi_h\left(\hat{V}_n;\mu_h,\sigma\right)}{\pi_h\phi_h\left(\hat{V}_n;\mu_h,\sigma\right)}\frac{\partial}{\partial \boldsymbol{\Psi}_G}\left[\pi_h\phi_h\left(\hat{V}_n;\mu_h,\sigma\right)\right] \\
&= \sum_{n=1}^{N}\sum_{h=1}^{G}\frac{\pi_h\phi_h\left(\hat{V}_n;\mu_h,\sigma\right)}{\sum_{g=1}^{G}\pi_g\phi_g\left(\hat{V}_n;\mu_g,\sigma\right)}\frac{\partial}{\partial \boldsymbol{\Psi}_G}\left[\log\left(\pi_h\phi_h\left(\hat{V}_n;\mu_h,\sigma\right)\right)\right] \\
&= \sum_{n=1}^{N}\sum_{h=1}^{G}\tau_h\left(\hat{V}_n;\boldsymbol{\Psi}_G^{(k)}\right)\frac{\partial}{\partial \boldsymbol{\Psi}_G}\left[\log\left(\pi_h\phi_h\left(\hat{V}_n;\mu_h,\sigma\right)\right)\right] \\
&= 0,
\end{aligned} \tag{A.7}$$

where $\tau_h\left(\hat{V}_n;\boldsymbol{\Psi}_G^{(k)}\right)$ is calculated in the E-step. This general expression can be used to determine the updates for the different parameters.

A.1 Update for the mixing proportions π_g

$$\frac{\partial \log L(\mathbf{\Psi}_G)}{\partial \pi_g} = \sum_{n=1}^{N} \sum_{h=1}^{G} \tau_h \left(\hat{V}_n; \mathbf{\Psi}_G^{(k)} \right) \frac{\partial}{\partial \pi_g} \left[\log \left(\pi_h \phi_h \left(\hat{V}_n; \mu_h, \sigma \right) \right) \right], \tag{A.8}$$

with

$$\frac{\partial}{\partial \pi_g} \left[\log \left(\pi_h \phi_h \left(\hat{V}_n; \mu_h, \sigma \right) \right) \right] = \begin{cases} 0 & \text{if } h \neq g \\ \frac{1}{\pi_g} & \text{if } h = g \\ \frac{-1}{\pi_G} & \text{if } h = G, \end{cases} \tag{A.9}$$

since $\sum_{h=1}^{G} \pi_h = 1$, and π_G is therefore not estimated, but determined as $\pi_G = 1 - \sum_{h=1}^{G-1} \pi_h$.
Setting equation (A.9) equal to zero yields

$$\begin{aligned} &\sum_{n=1}^{N} \left[\tau_g \left(\hat{V}_n; \mathbf{\Psi}_G^{(k)} \right) \frac{1}{\pi_g} - \tau_G \left(\hat{V}_n; \mathbf{\Psi}_G^{(k)} \right) \frac{1}{\pi_G} \right] = 0 \\ \Leftrightarrow \pi_g &= \frac{\pi_G}{\sum_{n=1}^{N} \tau_G \left(\hat{V}_n; \mathbf{\Psi}_G^{(k)} \right)} \sum_{n=1}^{N} \tau_g \left(\hat{V}_n; \mathbf{\Psi}_G^{(k)} \right) \\ \Leftrightarrow \pi_g &= \frac{1}{N} \sum_{n=1}^{N} \tau_g \left(\hat{V}_n; \mathbf{\Psi}_G^{(k)} \right), \end{aligned} \tag{A.10}$$

since $\sum_{n=1}^{N} \tau_G \left(\hat{V}_n; \mathbf{\Psi}_G^{(k)} \right)$ represents the number of columns that belong to component G.
This expression stays the same for both the statistics-only based method and the hybrid method.

A.2 Update for the variance σ^2

$$\frac{\partial \log L(\mathbf{\Psi}_G)}{\partial \sigma} = \sum_{n=1}^{N}\sum_{h=1}^{G} \tau_h\left(\hat{V}_n; \mathbf{\Psi}_G^{(k)}\right) \frac{\partial}{\partial \sigma}\left[\log\left(\pi_h \phi_h\left(\hat{V}_n; \mu_h, \sigma\right)\right)\right], \tag{A.11}$$

with

$$\begin{aligned}
\frac{\partial}{\partial \sigma}\left[\log\left(\pi_h \phi_h\left(\hat{V}_n; \mu_h, \sigma\right)\right)\right] &= \frac{\pi_h}{\pi_h \phi_h\left(\hat{V}_n; \mu_h, \sigma\right)} \frac{\partial}{\partial \sigma}\left[\phi_h\left(\hat{V}_n; \mu_h, \sigma\right)\right] \qquad \text{(A.12)}\\
&= \frac{1}{\phi_h\left(\hat{V}_n; \mu_h, \sigma\right)} \left[\frac{-1}{\sigma^2} + \frac{1}{\sigma}\frac{\left(\hat{V}_n - \mu_h\right)^2}{\sigma^3}\right] \frac{1}{\sqrt{2\pi}} \exp\left(-\frac{\left(\hat{V}_n - \mu_h\right)^2}{2\sigma^2}\right)\\
&= \left[\frac{-1}{\sigma} + \frac{\left(\hat{V}_n - \mu_h\right)^2}{\sigma^3}\right].
\end{aligned}$$

Setting equation (A.11) equal to zero yields

$$\begin{aligned}
&\sum_{n=1}^{N}\sum_{g=1}^{G} \tau_g\left(\hat{V}_n; \mathbf{\Psi}_G^{(k)}\right) \left[\frac{-1}{\sigma} + \frac{\left(\hat{V}_n - \mu_h\right)^2}{\sigma^3}\right] = 0\\
\Leftrightarrow \frac{1}{\sigma}\sum_{n=1}^{N}\sum_{g=1}^{G} \tau_g\left(\hat{V}_n; \mathbf{\Psi}_G^{(k)}\right) &= \frac{1}{\sigma^3}\sum_{n=1}^{N}\sum_{g=1}^{G} \tau_g\left(\hat{V}_n; \mathbf{\Psi}_G^{(k)}\right)\left(\hat{V}_n - \mu_g\right)^2\\
\Leftrightarrow \sigma^2 &= \frac{1}{N}\sum_{n=1}^{N}\sum_{g=1}^{G} \tau_g\left(\hat{V}_n; \mathbf{\Psi}_G^{(k)}\right)\left(\hat{V}_n - \mu_g\right)^2. \qquad \text{(A.13)}
\end{aligned}$$

The expression for the update for the hybrid method therefore becomes

$$\sigma^2 = \frac{1}{N}\sum_{n=1}^{N}\sum_{g=1}^{G} \tau_g\left(\hat{V}_n; \mathbf{\Psi}_G^{(k)}\right)\left(\hat{V}_n - a\mathcal{M}_g\right)^2, \tag{A.14}$$

where we have substituted $\mu_g = a\mathcal{M}_g$.

A.3 Update for the locations μ_g

$$\frac{\partial \log L(\phi_G)}{\partial \mu_g} = \sum_{n=1}^{N} \sum_{h=1}^{G} \tau_h \left(\hat{V}_n; \mathbf{\Psi}_G^{(k)} \right) \frac{\partial}{\partial \mu_g} \left[\log \left(\pi_h \phi_h \left(\hat{V}_n; \mu_h, \sigma \right) \right) \right], \tag{A.15}$$

with

$$\begin{aligned}
\frac{\partial}{\partial \mu_g} \left[\log \left(\pi_h \phi_h \left(\hat{V}_n; \mu_h, \sigma \right) \right) \right] &= \frac{\pi_g}{\pi_g \phi_g \left(\hat{V}_n; \mu_g, \sigma \right)} \frac{\partial}{\partial \mu_g} \left[\phi_g \left(\hat{V}_n; \mu_g, \sigma \right) \right] \delta_{hg} \\
&= \frac{\delta_{hg}}{\phi_g \left(\hat{V}_n; \mu_g, \sigma \right)} \frac{1}{\sqrt{2\pi\sigma^2}} \frac{\partial}{\partial \mu_g} \left[\exp \left(- \frac{\left(\hat{V}_n - \mu_g \right)^2}{2\sigma^2} \right) \right] \\
&= \frac{\delta_{hg}}{\phi_g \left(\hat{V}_n; \mu_g, \sigma \right)} \frac{\hat{V}_n - \mu_g}{\sigma^2} \phi_g \left(\hat{V}_n; \mu_g, \sigma \right) \\
&= \frac{\hat{V}_n - \mu_g}{\sigma^2} \delta_{hg}.
\end{aligned} \tag{A.16}$$

Setting equation (A.15) equal to zero yields

$$\begin{aligned}
\sum_{n=1}^{N} \tau_g \left(\hat{V}_n; \mathbf{\Psi}_G^{(k)} \right) \frac{\hat{V}_n - \mu_g}{\sigma^2} &= 0 \\
\Leftrightarrow \mu_g &= \frac{\sum_{n=1}^{N} \tau_g \left(\hat{V}_n; \mathbf{\Psi}_G^{(k)} \right) \hat{V}_n}{\sum_{n=1}^{N} \tau_g \left(\hat{V}_n; \mathbf{\Psi}_G^{(k)} \right)}.
\end{aligned} \tag{A.17}$$

A.4 Update for the scaling parameter a

$$\frac{\partial \log L(\mathbf{\Psi}_G)}{\partial a} = \sum_{n=1}^{N}\sum_{h=1}^{G} \tau_g\left(\hat{V}_n; \mathbf{\Psi}_G^{(k)}\right) \frac{\partial}{\partial a}\left[\log\left(\pi_h \phi_h\left(\hat{V}_n; a, \sigma\right)\right)\right], \tag{A.18}$$

with

$$\begin{aligned}
\frac{\partial}{\partial a}\left[\log\left(\pi_g \phi_g\left(\hat{V}_n; a, \sigma\right)\right)\right] &= \frac{\pi_g}{\pi_g \phi_g\left(\hat{V}_n; a, \mathcal{M}_g, \sigma\right)} \frac{\partial}{\partial a}\left[\phi_g\left(\hat{V}_n; a, \mathcal{M}_g, \sigma\right)\right] \\
&= \frac{1}{\phi_g\left(\hat{V}_n; a, \mathcal{M}_g, \sigma\right)} \frac{\partial}{\partial a}\left[\frac{1}{\sqrt{2\pi}\sigma} \exp\left(-\frac{\left(\hat{V}_n - a\mathcal{M}_g\right)^2}{2\sigma^2}\right)\right] \\
&= \frac{1}{\phi_g\left(\hat{V}_n; a, \mathcal{M}_g, \sigma\right)} \frac{1}{\sqrt{2\pi}\sigma}(-2)\frac{\hat{V}_n - a\mathcal{M}_g}{2\sigma^2}(-\mathcal{M}_g) \exp\left(-\frac{\left(\hat{V}_n - a\mathcal{M}_g\right)^2}{2\sigma^2}\right) \\
&= \frac{\mathcal{M}_g\left(\hat{V}_n - a\mathcal{M}_g\right)}{\sigma^2},
\end{aligned} \tag{A.19}$$

with $\mathcal{M}_g$ the library value corresponding to the g^{th} component.

Setting equation (A.18) equal to zero yields

$$\sum_{n=1}^{N}\sum_{g=1}^{G} \tau_g\left(\hat{V}_n; \mathbf{\Psi}_G^{(k)}\right) \frac{\mathcal{M}_g\left(\hat{V}_n - a\mathcal{M}_g\right)}{\sigma^2} = 0 \tag{A.20}$$

$$\Leftrightarrow a = \frac{\sum_{n=1}^{N}\sum_{g=1}^{G} \tau_g\left(\hat{V}_n; \mathbf{\Psi}_G^{(k)}\right) \hat{V}_n \mathcal{M}_g}{\sum_{n=1}^{N}\sum_{g=1}^{G} \tau_g\left(\hat{V}_n; \mathbf{\Psi}_G^{(k)}\right) \mathcal{M}_g^2}. \tag{A.21}$$

Appendix B

Cramér-Rao lower bound

In this appendix, the Cramér-Rao lower bound will be derived for the hybrid statistics-simulations based atom-counting method. The likelihood function is expressed by equation (B.1).

$$p(\hat{\mathbf{V}};\mathbf{\Psi}_G) = \Pi_{n=1}^{N} f_{\text{mix}}(\hat{V}_n;\mathbf{\Psi}_G), \tag{B.1}$$

with the Gaussian mixture model expressed by equation (B.3):

$$f_{\text{mix}}\left(\hat{V}_n;\mathbf{\Psi}_G\right) = \sum_{g=1}^{G} \pi_g \phi_g\left(\hat{V}_n;a,\sigma\right) \tag{B.2}$$

$$= \sum_{g=1}^{G} \pi_g \frac{1}{\sqrt{2\pi\sigma^2}} \exp\left(-\frac{(\hat{V}_n - a\mathcal{M}_g)^2}{2\sigma^2}\right). \tag{B.3}$$

The Fisher information matrix is defined by equation (B.5).

$$F_{\mathbf{\Psi}_G} = -\mathbb{E}\left[\left.\frac{\partial^2 \ln p(\hat{\mathbf{V}};\mathbf{\Psi}_G)}{\partial\mathbf{\Psi}_G\partial\mathbf{\Psi}_G^T}\right|_{\mathbf{\Psi}_G=\mathbf{\Psi}_0}\right] \tag{B.4}$$

$$= -N\int_{-\infty}^{\infty} \left.\frac{\partial^2 \ln f_{\text{mix}}(V;\mathbf{\Psi}_G)}{\partial\mathbf{\Psi}_G\partial\mathbf{\Psi}_G^T}\right|_{\mathbf{\Psi}_G=\mathbf{\Psi}_0} f_{\text{mix}}(V;\mathbf{\Psi}_G)dV, \tag{B.5}$$

where $\mathbf{\Psi}_0$ is the vector with the actual values of the parameters to be estimated. Equation (B.5) is written in full matrix form of equation (B.6).

$$F_{\mathbf{\Psi}_G} = -N\int_{L}^{U} \left.\begin{pmatrix} \frac{\partial^2 \ln p}{\partial\pi_1^2} & \frac{\partial^2 \ln p}{\partial\pi_1\partial\pi_2} & \frac{\partial^2 \ln p}{\partial\pi_1\partial\pi_3} & \frac{\partial^2 \ln p}{\partial\pi_1\partial\pi_4} & \frac{\partial^2 \ln p}{\partial\pi_1\partial a} & \frac{\partial^2 \ln p}{\partial\pi_1\partial\sigma} \\ \frac{\partial^2 \ln p}{\partial\pi_2\partial\pi_1} & \frac{\partial^2 \ln p}{\partial\pi_2^2} & \frac{\partial^2 \ln p}{\partial\pi_2\partial\pi_3} & \frac{\partial^2 \ln p}{\partial\pi_2\partial\pi_4} & \frac{\partial^2 \ln p}{\partial\pi_2\partial a} & \frac{\partial^2 \ln p}{\partial\pi_2\partial\sigma} \\ \frac{\partial^2 \ln p}{\partial\pi_3\partial\pi_1} & \frac{\partial^2 \ln p}{\partial\pi_3\partial\pi_2} & \frac{\partial^2 \ln p}{\partial\pi_3^2} & \frac{\partial^2 \ln p}{\partial\pi_3\partial\pi_4} & \frac{\partial^2 \ln p}{\partial\pi_3\partial a} & \frac{\partial^2 \ln p}{\partial\pi_3\partial\sigma} \\ \frac{\partial^2 \ln p}{\partial\pi_4\partial\pi_1} & \frac{\partial^2 \ln p}{\partial\pi_4\partial\pi_2} & \frac{\partial^2 \ln p}{\partial\pi_4\partial\pi_3} & \frac{\partial^2 \ln p}{\partial\pi_4^2} & \frac{\partial^2 \ln p}{\partial\pi_4\partial a} & \frac{\partial^2 \ln p}{\partial\pi_4\partial\sigma} \\ \frac{\partial^2 \ln p}{\partial a\partial\pi_1} & \frac{\partial^2 \ln p}{\partial a\partial\pi_2} & \frac{\partial^2 \ln p}{\partial a\partial\pi_3} & \frac{\partial^2 \ln p}{\partial a\partial\pi_4} & \frac{\partial^2 \ln p}{\partial a^2} & \frac{\partial^2 \ln p}{\partial a\partial\sigma} \\ \frac{\partial^2 \ln p}{\partial\sigma\partial\pi_1} & \frac{\partial^2 \ln p}{\partial\sigma\partial\pi_2} & \frac{\partial^2 \ln p}{\partial\sigma\partial\pi_3} & \frac{\partial^2 \ln p}{\partial\sigma\partial\pi_4} & \frac{\partial^2 \ln p}{\partial\sigma\partial a} & \frac{\partial^2 \ln p}{\partial\sigma^2} \end{pmatrix}\right|_{\mathbf{\Psi}_G=\mathbf{\Psi}_0} f_{\text{mix}}(V;\mathbf{\Psi}_G)dV, \tag{B.6}$$

where L and U are the finite boundaries of the integration in order to implement the symmetric Fisher information matrix, chosen equal to

$$L = \min(a\mathcal{M}) - 3\sigma, \tag{B.7}$$

$$U = \max(a\mathcal{M}) + 3\sigma, \tag{B.8}$$

with $\mathcal{M}$ the library. The Cramér-Rao lower bound is defined by (B.9).

$$\mathrm{cov}(\mathbf{\Psi}_G) \geq F^{-1}_{\mathbf{\Psi}_G}, \tag{B.9}$$

or

$$\mathrm{var}([\mathbf{\Psi}_G]_k] \geq [F^{-1}_{\mathbf{\Psi}_G}]_{kk}, \tag{B.10}$$

for the separate parameters. Notation is simplified as follows:

$$\phi_g(\hat{V}_n; a, \sigma) = \phi_g, \tag{B.11}$$
$$f_{\mathrm{mix}}(\hat{V}_n; \mathbf{\Psi}_G) = f_{\mathrm{mix}}, \tag{B.12}$$
$$p(\hat{\mathbf{V}}; \mathbf{\Psi}_G) = p. \tag{B.13}$$

The vector of parameters to be estimated in this specific case equals

$$\mathbf{\Psi}_G = (\pi_1, ..., \pi_{G-1}, a, \sigma), \tag{B.14}$$

because of the normalisation condition for the mixing proportions

$$\sum_{g=1}^{G} \pi_g = 1 \Rightarrow \pi_G = \left(1 - \sum_{g=1}^{G-1} \pi_g\right). \tag{B.15}$$

The first derivatives of the likelihood function to the parameters are expressed by equations (B.16), (B.18) and (B.17).

$$\begin{aligned}
\frac{\partial \ln p}{\partial \pi_i} &= \frac{\partial}{\partial \pi_i}\left(\sum_{n=1}^{N} \ln f_{\mathrm{mix}}\right) \\
&= \sum_{n=1}^{N} \frac{1}{f_{\mathrm{mix}}} \frac{\partial f_{\mathrm{mix}}}{\partial \pi_i} \\
&= \sum_{n=1}^{N} \frac{1}{f_{\mathrm{mix}}} \frac{\partial}{\partial \pi_i}\left[\sum_{g=1}^{G-1}(\pi_g \phi_g) + \left(1 - \sum_{h=1}^{G} \pi_h\right)\phi_G\right] \\
&= \sum_{n=1}^{N} \frac{1}{f_{\mathrm{mix}}} (\phi_i + (-1)\phi_G) \\
&= \sum_{n=1}^{N} \frac{\phi_i - \phi_G}{f_{\mathrm{mix}}},
\end{aligned} \tag{B.16}$$

$$
\begin{aligned}
\frac{\partial \ln p}{\partial a} &= \frac{\partial}{\partial a}\left(\sum_{n=1}^{N} \ln f_{\text{mix}}\right) \\
&= \sum_{n=1}^{N} \frac{1}{f_{\text{mix}}} \frac{\partial f_{\text{mix}}}{\partial a} \\
&= \sum_{n=1}^{N} \frac{1}{f_{\text{mix}}} \frac{\partial}{\partial a}\left[\sum_{g=1}^{G-1}(\pi_g \phi_g) + \left(1 - \sum_{h=1}^{G-1} \pi_h\right)\phi_G\right] \\
&= \sum_{n=1}^{N} \frac{1}{f_{\text{mix}}}\left[\sum_{g=1}^{G-1} \pi_g \frac{1}{\sqrt{2\pi}\sigma}\left(-\frac{2(V_n - a\mathcal{M}_g)}{2\sigma^2}(-\mathcal{M}_g)\right)\exp\left(-\frac{(V_n - a\mathcal{M}_g)^2}{2\sigma^2}\right)\right. \\
&\quad \left. + \left(1 - \sum_{h=1}^{G-1} \pi_h\right)\frac{1}{\sqrt{2\pi}\sigma}\left(-\frac{2(V_n - a\mathcal{M}_G)}{2\sigma^2}(-\mathcal{M}_G)\right)\exp\left(-\frac{(V_n - a\mathcal{M}_G)^2}{2\sigma^2}\right)\right] \\
&= \sum_{n=1}^{N} \frac{1}{f_{\text{mix}}}\left[\sum_{g=1}^{G-1} \pi_g \phi_g \frac{(V_n - a\mathcal{M}_g)\mathcal{M}_g}{\sigma^2} + \left(1 - \sum_{h=1}^{G-1} \pi_h\right)\phi_G \frac{(V_n - a\mathcal{M}_G)\mathcal{M}_G}{\sigma^2}\right] \\
&= \sum_{n=1}^{N} \frac{1}{f_{\text{mix}}} \sum_{g=1}^{G} \pi_g \phi_g \frac{(V_n - a\mathcal{M}_g)\mathcal{M}_g}{\sigma^2}, \qquad \text{(B.17)}
\end{aligned}
$$

$$
\begin{aligned}
\frac{\partial \ln p}{\partial \sigma} &= \frac{\partial}{\partial \sigma}\left(\sum_{n=1}^{N} \ln f_{\text{mix}}\right) \\
&= \sum_{n=1}^{N} \frac{1}{f_{\text{mix}}} \frac{\partial f_{\text{mix}}}{\partial \sigma} \\
&= \sum_{n=1}^{N} \frac{1}{f_{\text{mix}}} \frac{\partial}{\partial \sigma}\left[\sum_{g=1}^{G-1}(\pi_g \phi_g) + \left(1 - \sum_{h=1}^{G-1} \pi_h\right)\phi_G\right] \\
&= \sum_{n=1}^{N} \frac{1}{f_{\text{mix}}}\left[\sum_{g=1}^{G-1} \pi_g \left(\frac{1}{\sqrt{2\pi}}\frac{-1}{\sigma^2}\exp\left(-\frac{(V_n - a\mathcal{M}_g)^2}{2\sigma^2}\right)\right.\right. \\
&\quad \left. + \frac{1}{\sqrt{2\pi}\sigma}\left(-\frac{(V_n - a\mathcal{M}_g)^2}{2}\left(\frac{-2}{\sigma^3}\right)\right)\exp\left(-\frac{(V_n - a\mathcal{M}_g)^2}{2\sigma^2}\right)\right) \\
&\quad + \left(1 - \sum_{h=1}^{G-1} \pi_h\right)\left(\frac{1}{\sqrt{2\pi}}\frac{-1}{\sigma^2}\exp\left(-\frac{(V_n - a\mathcal{M}_G)^2}{2\sigma^2}\right)\right. \\
&\quad \left.\left. + \frac{1}{\sqrt{2\pi}\sigma}\left(-\frac{(V_n - a\mathcal{M}_G)^2}{2}\left(\frac{-2}{\sigma^3}\right)\right)\exp\left(-\frac{(V_n - a\mathcal{M}_G)^2}{2\sigma^2}\right)\right)\right] \\
&= \sum_{n=1}^{N} \frac{1}{f_{\text{mix}}}\left[\sum_{g=1}^{G-1} \pi_g \phi_g \left(\frac{(V_n - a\mathcal{M}_g)^2}{\sigma^3} - \frac{1}{\sigma}\right) + \left(1 - \sum_{h=1}^{G-1} \pi_h\right)\phi_G \left(\frac{(V_n - a\mathcal{M}_G)^2}{\sigma^3} - \frac{1}{\sigma}\right)\right] \\
&= \sum_{n=1}^{N} \frac{1}{f_{\text{mix}}} \sum_{g=1}^{G} \pi_g \phi_g \left(\frac{(V_n - a\mathcal{M}_g)^2}{\sigma^3} - \frac{1}{\sigma}\right). \qquad \text{(B.18)}
\end{aligned}
$$

Second derivatives are derived in the following and finally expressed by equations (B.19)-(B.24).

$$\begin{aligned}
\frac{\partial^2 \ln p}{\partial \pi_i \partial \pi_k} &= \frac{\partial}{\partial \pi_k}\left(\frac{\partial \ln p}{\partial \pi_i}\right) \\
&= \frac{\partial}{\partial \pi_k}\left(\sum_{n=1}^{N} \frac{\phi_i - \phi_G}{f_{\text{mix}}}\right) \\
&= \sum_{n=1}^{N} (\phi_i - \phi_G)\left(\frac{-1}{f_{\text{mix}}^2}\right)\frac{\partial f_{\text{mix}}}{\partial \pi_k} \\
&= -\sum_{n=1}^{N} \frac{(\phi_i - \phi_G)(\phi_k - \phi_G)}{f_{\text{mix}}^2},
\end{aligned} \tag{B.19}$$

$$\begin{aligned}
\frac{\partial^2 \ln p}{\partial \pi_i \partial a} &= \frac{\partial}{\partial a}\left(\frac{\partial \ln p}{\partial \pi_i}\right) \\
&= \frac{\partial}{\partial a}\left(\sum_{n=1}^{N} \frac{\phi_i - \phi_G}{f_{\text{mix}}}\right) \\
&= \sum_{n=1}^{N}\left[\frac{1}{f_{\text{mix}}}\left(\frac{\partial \phi_i}{\partial a} - \frac{\partial \phi_G}{\partial a}\right) - \frac{\phi_i - \phi_G}{f_{\text{mix}}^2}\frac{\partial f_{\text{mix}}}{\partial a}\right] \\
&= \sum_{n=1}^{N}\left[\frac{1}{f_{\text{mix}}}\left(\phi_i \frac{(V_n - a\mathcal{M}_i)\mathcal{M}_i}{\sigma^2} - \phi_G \frac{(V_n - a\mathcal{M}_G)\mathcal{M}_G}{\sigma^2}\right)\right. \\
&\quad \left. - \frac{\phi_i - \phi_G}{f_{\text{mix}}^2}\sum_{g=1}^{G} \pi_g \phi_g \frac{(V_n - a\mathcal{M}_g)\mathcal{M}_g}{\sigma^2}\right],
\end{aligned} \tag{B.20}$$

$$\begin{aligned}
\frac{\partial^2 \ln p}{\partial \pi_i \partial \sigma} &= \frac{\partial}{\partial \sigma}\left(\frac{\partial \ln p}{\partial \pi_i}\right) \\
&= \frac{\partial}{\partial \sigma}\left(\sum_{n=1}^{N} \frac{\phi_i - \phi_G}{f_{\text{mix}}}\right) \\
&= \sum_{n=1}^{N}\left[\frac{1}{f_{\text{mix}}}\left(\frac{\partial \phi_i}{\partial \sigma} - \frac{\partial \phi_G}{\partial \sigma}\right) - \frac{\phi_i - \phi_G}{f_{\text{mix}}^2}\frac{\partial f_{\text{mix}}}{\partial \sigma}\right] \\
&= \sum_{n=1}^{N}\left[\frac{1}{f_{\text{mix}}}\left(\phi_i\left(\frac{(V_n - a\mathcal{M}_i)^2}{\sigma^3} - \frac{1}{\sigma}\right) - \phi_G\left(\frac{(V_n - a\mathcal{M}_G)^2}{\sigma^3} - \frac{1}{\sigma}\right)\right)\right. \\
&\quad \left. - \frac{\phi_i - \phi_G}{f_{\text{mix}}^2}\sum_{g=1}^{G} \pi_g \phi_g \left(\frac{(V_n - a\mathcal{M}_g)^2}{\sigma^3} - \frac{1}{\sigma}\right)\right],
\end{aligned} \tag{B.21}$$

$$
\begin{aligned}
\frac{\partial^2 \ln p}{\partial a \partial \sigma} &= \frac{\partial}{\partial \sigma}\left(\frac{\partial \ln p}{\partial a}\right) \\
&= \frac{\partial}{\partial \sigma}\left(\sum_{n=1}^{N}\frac{1}{f_{\text{mix}}}\sum_{g=1}^{G}\pi_g\phi_g\frac{(V_n - a\mathcal{M}_g)\mathcal{M}_g}{\sigma^2}\right) \\
&= \sum_{n=1}^{N}\left[-\frac{1}{f_{\text{mix}}^2}\frac{\partial f_{\text{mix}}}{\partial \sigma}\left(\sum_{g=1}^{G}\pi_g\phi_g\frac{(V_n - a\mathcal{M}_g)\mathcal{M}_g}{\sigma^2}\right) + \frac{1}{f_{\text{mix}}}\frac{\partial}{\partial \sigma}\left(\sum_{g=1}^{G}\pi_g\phi_g\frac{(V_n - a\mathcal{M}_g)\mathcal{M}_g}{\sigma^2}\right)\right] \\
&= \sum_{n=1}^{N}\left[-\frac{1}{f_{\text{mix}}^2}\left(\sum_{g=1}^{G}\pi_g\phi_g\left(\frac{(V_n - a\mathcal{M}_g)^2}{\sigma^3} - \frac{1}{\sigma}\right)\right)\left(\sum_{g=1}^{G}\pi_g\phi_g\frac{(V_n - a\mathcal{M}_g)\mathcal{M}_g}{\sigma^2}\right)\right. \\
&\quad \left. + \frac{1}{f_{\text{mix}}}\sum_{g=1}^{G}\pi_g\phi_g\frac{(V_n - a\mathcal{M}_g)\mathcal{M}_g}{\sigma^2}\left(\frac{(V_n - a\mathcal{M}_g)^2}{\sigma^3} - \frac{3}{\sigma}\right)\right], \qquad \text{(B.22)}
\end{aligned}
$$

$$
\begin{aligned}
\frac{\partial^2 \ln p}{\partial a^2} &= \frac{\partial}{\partial a}\left(\frac{\partial \ln p}{\partial a}\right) \\
&= \frac{\partial}{\partial a}\left(\sum_{n=1}^{N}\frac{1}{f_{\text{mix}}}\sum_{g=1}^{G}\pi_g\phi_g\frac{(V_n - a\mathcal{M}_g)\mathcal{M}_g}{\sigma^2}\right) \\
&= \sum_{n=1}^{N}\left[-\frac{1}{f_{\text{mix}}^2}\left(\sum_{h=1}^{G}\pi_h\phi_h\frac{(V_n - a\mathcal{M}_h)\mathcal{M}_h}{\sigma^2}\right)\left(\sum_{g=1}^{G}\pi_g\phi_g\frac{(V_n - a\mathcal{M}_g)\mathcal{M}_g}{\sigma^2}\right)\right. \\
&\quad \left. + \frac{1}{f_{\text{mix}}}\left(\sum_{g=1}^{G}\pi_g\left[\phi_g\frac{(V_n - a\mathcal{M}_g)\mathcal{M}_g}{\sigma^2}\frac{(V_n - a\mathcal{M}_g)\mathcal{M}_g}{\sigma^2} + \phi_g\left(\frac{-\mathcal{M}_g^2}{\sigma^2}\right)\right]\right)\right] \\
&= \sum_{n=1}^{N}\left[-\frac{1}{f_{\text{mix}}^2}\left(\sum_{g=1}^{G}\pi_g\phi_g\frac{(V_n - a\mathcal{M}_g)\mathcal{M}_g}{\sigma^2}\right)^2\right. \\
&\quad \left. + \frac{1}{f_{\text{mix}}}\sum_{g=1}^{G}\pi_g\phi_g\left(\left(\frac{(V_n - a\mathcal{M}_g)\mathcal{M}_g}{\sigma^2}\right)^2 - \frac{\mathcal{M}_g^2}{\sigma^2}\right)\right] \qquad \text{(B.23)}
\end{aligned}
$$

$$
\begin{aligned}
\frac{\partial^2 \ln p}{\partial \sigma^2} &= \frac{\partial}{\partial \sigma}\left(\frac{\partial \ln p}{\partial \sigma}\right) \\
&= \frac{\partial}{\partial \sigma}\left(\sum_{n=1}^{N}\frac{1}{f_{\text{mix}}}\sum_{g=1}^{G}\pi_g\phi_g\left(\frac{(V_n - a\mathcal{M}_g)^2}{\sigma^3} - \frac{1}{\sigma}\right)\right) \\
&= \sum_{n=1}^{N}\left[-\frac{1}{f_{\text{mix}}^2}\left(\sum_{h=1}^{G}\pi_h\phi_h\left(\frac{(V_n - a\mathcal{M}_h)^2}{\sigma^3} - \frac{1}{\sigma}\right)\right)\left(\sum_{g=1}^{G}\pi_g\phi_g\left(\frac{(V_n - a\mathcal{M}_g)^2}{\sigma^3} - \frac{1}{\sigma}\right)\right)\right. \\
&\quad \left. + \frac{1}{f_{\text{mix}}}\sum_{g=1}^{G}\pi_g\phi_g\left[\left(\frac{(V_n - a\mathcal{M}_g)^2}{\sigma^3} - \frac{1}{\sigma}\right)^2 + \left(-\frac{3(V_n - a\mathcal{M}_g)^2}{\sigma^4} + \frac{1}{\sigma^2}\right)\right]\right]. \qquad \text{(B.24)}
\end{aligned}
$$

Finally, the lower bound on a function of estimated parameters is determined by equation (B.25).

$$\mathrm{cov}(\hat{\gamma}) \geq \frac{\partial \gamma(\theta)}{\partial \theta^T} F_\theta^{-1} \frac{\partial \gamma(\theta)^T}{\partial \theta} \tag{B.25}$$

Since $\pi_G = \pi_G(\pi_1, \pi_2, ..., \pi_{G-1}) = 1 - \sum_{g=1}^{G-1} \pi_g$, the lower bound on the variance of π_G is expressed as follows:

$$\mathrm{var}(\pi_G) \geq \frac{\partial \pi_G(\theta)}{\partial \theta^T} F^{-1}_{(\pi_1 \pi_2 ... \pi_{G-1})} \frac{\partial \pi_G(\theta)^T}{\partial \theta}, \tag{B.26}$$

with

$$\frac{\partial \pi_G(\theta)}{\partial \theta^T} = \begin{pmatrix} \frac{\partial \pi_G}{\partial \pi_1} & \frac{\partial \pi_G}{\partial \pi_2} & \cdots & \frac{\partial \pi_G}{\partial \pi_{G-1}} \end{pmatrix}, \tag{B.27}$$

and

$$\frac{\partial \pi_G}{\partial \pi_i} = \frac{\partial}{\partial \pi_i} \left(1 - \sum_{g=1}^{G-1} \pi_g \right) = -1. \tag{B.28}$$

Therefore the explicit expression of the lower bound in matrix expression equals:

$$\mathrm{var}(\pi_G) \geq \begin{pmatrix} -1 & \cdots & -1 \end{pmatrix} \left(-N \int_L^U \begin{pmatrix} \frac{\partial^2 \ln p}{\partial \pi_1^2} & \frac{\partial^2 \ln p}{\partial \pi_1 \partial \pi_2} & \frac{\partial^2 \ln p}{\partial \pi_1 \partial \pi_3} & \frac{\partial^2 \ln p}{\partial \pi_1 \partial \pi_4} \\ \frac{\partial^2 \ln p}{\partial \pi_2 \partial \pi_1} & \frac{\partial^2 \ln p}{\partial \pi_2^2} & \frac{\partial^2 \ln p}{\partial \pi_2 \partial \pi_3} & \frac{\partial^2 \ln p}{\partial \pi_2 \partial \pi_4} \\ \frac{\partial^2 \ln p}{\partial \pi_3 \partial \pi_1} & \frac{\partial^2 \ln p}{\partial \pi_3 \partial \pi_2} & \frac{\partial^2 \ln p}{\partial \pi_3^2} & \frac{\partial^2 \ln p}{\partial \pi_3 \partial \pi_4} \\ \frac{\partial^2 \ln p}{\partial \pi_4 \partial \pi_1} & \frac{\partial^2 \ln p}{\partial \pi_4 \partial \pi_2} & \frac{\partial^2 \ln p}{\partial \pi_4 \partial \pi_3} & \frac{\partial^2 \ln p}{\partial \pi_4^2} \end{pmatrix} \Bigg|_{\mathbf{\Psi}_G = \mathbf{\Psi}_0} f_{\mathrm{mix}}(V; \mathbf{\Psi}_G) dV \right)^{-1} \begin{pmatrix} -1 \\ \vdots \\ -1 \end{pmatrix}$$